Simulationen zur H^- Charge Exchange Injection in den CERN Proton Synchrotron Booster mit Linac4

(Simulations of the H^- Charge Exchange Injection into the CERN Proton Synchrotron Booster with Linac4)

von
Matthias Scholz
geboren am
10. August 1979

Diplomarbeit im Studiengang Physik
Universität Hamburg

2010

1. Gutachter: Dr. Christan Carli
2. Gutachter: Prof. Eckhart Elsen

Abstract

The CERN Proton Synchrotron Booster (PSB) is the first synchrotron of the LHC proton injection chain. The main limitation of the Booster performance is given by direct space charge effects at low energy. Linac2, the present pre-accelerator of the Booster, will be replaced by Linac4 in 2015. The main motivation for Linac4 is to increase the injection energy into the Booster from 50 MeV at present to 160 MeV to mitigate direct space charge effects. In addition, the conventional multiturn injection will be replaced by an H^- charge exchange injection requiring special hardware and, in particular, a closed orbit bump in the injection section (chicane) introducing perturbations on the lattice. Two different schemes which aim at mitigating the impact of these perturbations on PSB performance were tested: an active compensation with additional quadrupole components at dedicated positions in the ring and a passive compensation with gradients added to the chicane magnets. To find the best setting for the injection, simulations with the particle tracking code ORBIT were carried out for both schemes and the different results were compared. The simulations include the apertures, acceleration, space charge effects, scattering at the injection foil and planned schemes to populate the available phase space in transverse and longitudinal plane (Painting).

Zusammenfassung

Der CERN Proton Synchrotron Booster (PSB) ist das erste Synchrotron in der LHC Protonen-Injektions-Kette. Die wichtigste Leistungseinschränkung ist durch direkte Raumladungskräfte bei niedrigen Energien gegeben. Linac2, der aktuelle Vorbeschleuniger des Boosters, wird im Jahr 2015 durch Linac4 ersetzt werden. Die Hauptmotivation für Linac4 ist die Erhöhung der Injektionsenergie in den Booster von derzeit 50 MeV auf 160 MeV, um die direkten Raumladungseffekten abzuschwächen. Darüber hinaus wird die konventionelle Multiturn-Injection durch eine H^- Charge Exchange Injection ersetzt werden, welche spezielle Bauteile erfordert, insbesondere einen closed Orbit Bump (Schikane) im Injektionsabschnitt, wodurch Störungen im Lattice verursacht werden. Zwei verschiedene Schemata zur Reduzierung der Auswirkungen dieser Störungen auf die Leistung des PSB wurden getestet: Eine aktive Kompensation mit zusätzlichen quadrupol Komponenten an geeigneten Positionen im Ring und eine passive Kompensation mit zusätzlichen Gradienten in den Magneten der Schikane. Um die besten Einstellungen für die Injektionsschikane zu finden, wurden Simulationen für beide Schemata mit dem Particle Tracking Programm ORBIT ausgeführt und miteinander verglichen. Die Simulationen beinhalten die Aperturen, Beschleunigung, Raumladungseffekte, Streuung an der Injektionsfolie und geplante Schemata zur Füllung der bestehenden Phasenraumellipsen in transversaler und longitudinaler Ebene (Painting).

Contents

Chapter 1

Introduction

This thesis was written at the BE department at the CERN laboratory. CERN is the largest particle physics laboratory in the world, situated in the northwest suburbs of Geneva [1]. The thesis is concerned with the injection from a linac to a synchrotron and it was the task to run simulations to assess the feasibility of future machines and components. To this end, the particle tracking programme ORBIT [2] had to be understood as far as it was necessary to run simulations. This was realised step by step in such a way, that the simulated elements like apertures and injection equipment were added to the runs one by one. At the end, several simulations were carried out to compare different injection schemes investigating if they are feasible for the required beam parameters and, in case that they work, to explore which one provides the best results.

1.1 Accelerators at CERN

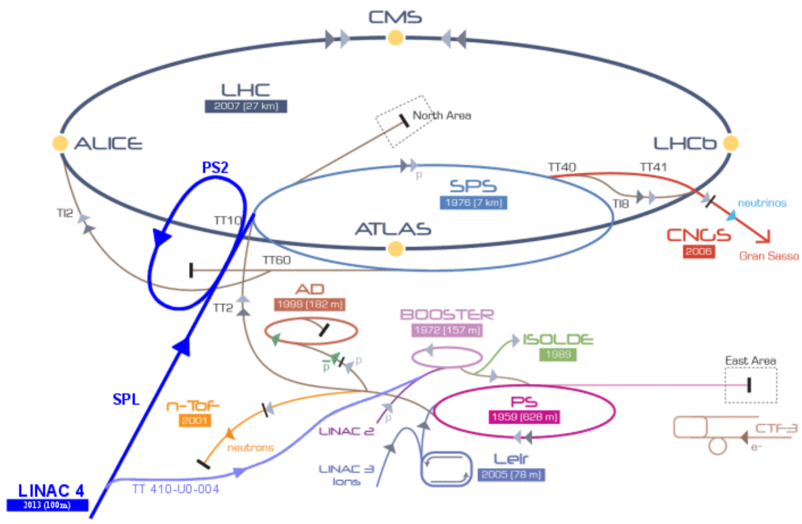

Figure 1.1: All existing and future particle accelerators at CERN including the experiments [3].

The largest accelerator at CERN is the Large Hadron Collider (LHC) which accelerates two proton beams in opposite directions from 450 GeV up to 3.5 TeV at present and up to nominal energy of 7 TeV in future. The proton beams collide at four dedicated places in the ring and six experiments (CMS, ATLAS, ALICE, LHCb, LHCf and TOTEM) analyse the data. To accelerate the protons up to the LHC injection energy of

450 GeV, a chain of pre-accelerators, starting with a linac and followed by three synchrotrons, is in use. At present, the first machine after the proton source is the Linac2 which accelerates the particles up to an energy of 50 MeV. The first synchrotron is the Proton Synchrotron Booster (PSB) with an ejection energy of 1.4 GeV, followed by the Proton Synchrotron (PS) where the particles get accelerated up to 26 GeV. The last synchrotron in the LHC injector chain is the Super Proton Synchrotron (SPS) which provides particle energies up 450 GeV for the LHC injection. Beside the proton acceleration, the LHC can also accelerate lead ions up to a maximum energy of 2.67 TeV per nucleon. The pre-accelerator chain for the ions consist of Linac3, LEIR, the PS and finally the SPS from where the injection to the LHC takes place. There are also more experiments than those around the LHC like the Antiproton Decelerator (AD), positioned behind the PS, the Isotope Separator On-Line (ISOLDE) experiment which is supplied with protons by the PS Booster or the CERN Neutrinos for Gran Sasso (CNGS) experiment, receiving protons from the SPS. The proposed future accelerators Linac4, SPL (Superconducting Proton Linac) and PS2 are shown in Fig. 1.1 on the left hand side in blue color.

1.2 Linac4 project

Linac4 will replace Linac2 in 2015 and the H^- ions accelerated with Linac4 will be injected to the PS Booster whose main limitations are direct space charge effects at low energies. The higher injection energy of 160 MeV instead of 50 MeV with Linac2 will mitigate the direct space charge effects and allow increasing the beam intensity and brightness of the Booster. To this end, the conventional multi turn injection used with Linac2 has to be replaced by a charge exchange injection where the ions will be stripped to protons by a thin carbon foil. The charge exchange injection requires two closed orbit bumps, the so-called "chicane" and the "injection painting" bump, both consisting out of four magnets. All injection elements have to be within the space available in the fixed lattice of the existing Booster. These constrains lead to short chicane magnets installed in the short injection straight section with a deflection angle of 66 mrad introducing additional vertical focusing effects perturbing the lattice. The perturbations will induce strong beta beating since the vertical tune is close to a half integer resonance. To compensate the perturbations, two different methods were tested, the "passive" and the "active" compensation scheme. For the first scheme, additional gradients have to be added to the chicane's magnets which have the same effect on the beam than rotations of the magnet's pole faces reducing the focusing effects and the strong beta beating in vertical plane. However, using this compensation scheme, one induces perturbations in the horizontal plane, but the consequences are less due to the fact that the beam is not close to a half-integer resonance in this plane. The second possibility to compensate the perturbations is to install additional quadrupole components to defocusing magnets existing in the lattice at dedicated positions outside the injection area. The positions have to be chosen such that the betatron phase advance between the perturbations and the compensation are suitable. These constrains are fulfilled by the defocusing magnets in the Booster periods 3 and 14.

To accumulate the particles for a high intensity beam with 1.6×10^{13} protons in the Booster, one has to inject the particles over 100 turns. For injections over several turns, one can apply so-called "painting-schemes" in order to fill the available phase in transversal and longitudinal plane with an even density distribution. To this end, the second closed orbit bump, the "painting bump", will be superimposed with the chicane in the charge exchange injection section allowing to use the painting scheme in horizontal plane. The longitudinal painting will be realised by varying energy of the Linac4 in a controlled way.

The aim of this thesis was to study different injection and compensation schemes and to compare them in order to provide information required to take the decision which compensation scheme should be used and how the injection from the Linac4 to the Booster could be managed.

Chapter 2

Theory

This chapter will tread all topics about accelerator physics which are applied in this thesis from the theoretical point of view. To avoid mistakes due to not clearly declared signs, Tab. 2.1 shows all used signs including the declarations.

Table 2.1: Declaration of the used signs.

α	The related Twiss-function	v	Velocity
β	The related Twiss-function	ϵ_x^*	Normalised horizontal rms Emittance
γ	The related Twiss-function	ϵ_x	Physical horizontal rms Emittance
c	Speed of Light	ϵ_y^*	Normalised vertical rms Emittance
β_{rel}	Velocity/c	ϵ_y	Physical vertical rms Emittance
γ_{rel}	The Lorentz factor	k	Focusing strength
m_0	Rest mass	B	Magnetic flux
e	Elementary charge	D	Dispersion
p	Momentum	U	Circumference

Furthermore, the coordinate System, as shown in Fig. 2.1, was used for the calculations and descriptions.

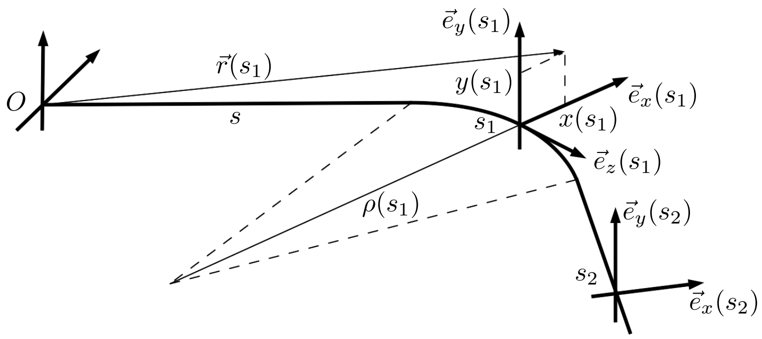

Figure 2.1: The machine coordinate system used in this thesis. $\vec{e}_x(s)$, $\vec{e}_y(s)$ and $\vec{e}_z(s)$ describe a local coordinate system at the longitudinal position s in the lattice.

The particle positions can be described in this coordinate system with vectors:

$$\vec{r}(s) = \vec{r}_0(s) + x(s)\ \vec{e}_x(s) + y(s)\ \vec{e}_y(s) \tag{2.1}$$

2.1 Transversal beam dynamics

2.1.1 Linear equation of motion

The linear equation of motion for both transversal planes for particles circulating the machine can be written as [4]:

$$x'' + K\,x = \frac{1}{\rho_x}\frac{\Delta p}{p_0} \tag{2.2}$$
$$y'' + k\,y = 0. \tag{2.3}$$

With the magnetic field gradient k and $K = \left(\frac{1}{\rho^2} + k\right)$ and the derivatives $x'' = \frac{d^2x}{ds^2}$ and $y'' = \frac{d^2y}{ds^2}$.

The general solution $x(s)$ of the Eq. 2.2 is the sum of the solution x_h of the homogeneous equation (like Eq. 2.3) and a particular solution x_i of the inhomogeneous equation.

$$x(s) = x_h(s) + x_i(s) \tag{2.4}$$

with:

$$x_h''(s) + K\,x_h(s) = 0 \tag{2.5}$$
$$x_i''(s) + K\,x_i(s) = \frac{1}{\rho_x(s)}\frac{\Delta p}{p_0}. \tag{2.6}$$

To separate the particle properties from the machine properties, one can write the solutions of the inhomogeneous equation like:

$$D(s) = \frac{x_i}{\Delta p/p_0}. \tag{2.7}$$

The general solution is then

$$x(s) = C(s)x_0 + S(s)x_0' + D(s)\frac{\Delta p}{p_0}, \tag{2.8}$$

with the cosine and sine like functions $C(s)$ and $S(s)$ plus the initial values $x(s_0) = x_0$ and $x'(s_0) = x_0'$. The principal solutions of homogeneous differential equation are [5]:

$$C(s) = \cos\sqrt{K}s \qquad \text{and} \qquad S(s) = \frac{1}{\sqrt{K}}\sin\sqrt{K}s \qquad \text{for} \qquad K > 0 \tag{2.9}$$

and

$$C(s) = \cosh\sqrt{|K|}s \qquad \text{and} \qquad S(s) = \frac{1}{\sqrt{|K|}}\sinh\sqrt{|K|}s \qquad \text{for} \qquad K < 0. \tag{2.10}$$

In order to proof the independence of these solutions, one can calculate the Wronski determinant W:

$$W = \begin{vmatrix} C & S \\ C' & S' \end{vmatrix} = CS' - SC' = C^2 + S^2 = 1 \neq 0. \tag{2.11}$$

The non-zero Wronski determinant verifies the independence of the two solutions of the homogeneous equation. To investigate the developing of the determinant, one can calculate its derivative with respect to the longitudinal coordinate s:

$$\frac{d}{ds}\left(CS' - SC'\right) = CS'' - SC'' = K\left(CS - SC\right) = 0. \tag{2.12}$$

The derivative of the Wronski determinant vanishes which means, the value of the determinant will not change: $W(s) = W(s_0)$. For this reason, the independence between the two solutions is preserved.

The solution of the inhomogeneous equation was defined as:

$$D(s) = \frac{x_i}{\Delta p/p_0}. \tag{2.13}$$

The Dispersion D(s) describes the part of the motion which is depending on the momentum. x(s) and x'(s) are related to their initial values by a linear transformation. Taking also the longitudinal component into account, one can write:

$$x(s) = C\,x_0 + S\,x_0' + D\left(\frac{\Delta p}{p_0}\right)_0 \tag{2.14}$$

$$x'(s) = C'\,x_0 + S'\,x_0' + D'\left(\frac{\Delta p}{p_0}\right)_0. \tag{2.15}$$

The Dispersion can be calculated by:

$$D(s) = S(s)\int_{s_o}^{s}\frac{1}{\rho(t)}C(t)\,dt - C(s)\int_{s_0}^{s}\frac{1}{\rho(t)}S(t)\,dt. \tag{2.16}$$

This definition fulfils the inhomogeneous part of Eq. 2.2 [6].

2.1.2 Transfer matrices

Transfer matrices describe the particle movement between two positions of the lattice [4]. A transfer matrix can be allocated to each element in the ring as well as to sets of elements. If the initial particle coordinates and the transfer matrices are known, the coordinates at all other positions in the lattice can be calculated by:

$$\vec{r}(s) = \mathbf{M}_{0,s}\,\vec{r}_0. \tag{2.17}$$

The matrices for several elements can be calculated multiplying the matrices of the single elements

$$\mathbf{M}_{set} = \prod_i \mathbf{M}_i. \tag{2.18}$$

Furthermore, the general transfer matrix is related to the sine and cosine like solutions of the linear equation of motion as well as to the dispersion. It is possible to write transfer matrices just for one plane, for the transversal planes or for all planes of the six-dimensional phase space, whereas the last two options allow also to implement the impacts between the planes. Below, there will be presented exemplary transfer matrices for different lattice elements.

The transfer matrix for a drift with length L is:

$$\mathbf{DS} = \begin{pmatrix} 1 & L & 0 & 0 & 0 & 0 \\ 0 & 1 & 0 & 0 & 0 & 0 \\ 0 & 0 & 1 & L & 0 & 0 \\ 0 & 0 & 0 & 1 & 0 & 0 \\ 0 & 0 & 0 & 0 & 1 & \frac{L}{\gamma_{rel}^2} \\ 0 & 0 & 0 & 0 & 0 & 1 \end{pmatrix}. \tag{2.19}$$

The transfer matrices for a focusing and a defocusing quadrupole magnet with length L, maximum magnetic field B_0 and aperture a are:

$$\mathbf{QF} = \begin{pmatrix} \cos\sqrt{k}L & \frac{\sin\sqrt{k}L}{\sqrt{k}} & 0 & 0 & 0 & 0 \\ -\sqrt{k}\sin\sqrt{k}L & \cos\sqrt{k}L & 0 & 0 & 0 & 0 \\ 0 & 0 & \cosh\sqrt{k}L & \frac{\sinh\sqrt{k}L}{\sqrt{k}} & 0 & 0 \\ 0 & 0 & \sqrt{k}\sinh\sqrt{k}L & \cosh\sqrt{k}L & 0 & 0 \\ 0 & 0 & 0 & 0 & 1 & \frac{L}{\gamma_{rel}^2} \\ 0 & 0 & 0 & 0 & 0 & 1 \end{pmatrix}, \tag{2.20}$$

$$\mathbf{QD} = \begin{pmatrix} \cosh\sqrt{k}L & \frac{\sinh\sqrt{k}L}{\sqrt{k}} & 0 & 0 & 0 & 0 \\ \sqrt{k}\sinh\sqrt{k}L & \cosh\sqrt{k}L & 0 & 0 & 0 & 0 \\ 0 & 0 & \cos\sqrt{k}L & \frac{\sin\sqrt{k}L}{\sqrt{k}} & 0 & 0 \\ 0 & 0 & -\sqrt{k}\sin\sqrt{k}L & \cos\sqrt{k}L & 0 & 0 \\ 0 & 0 & 0 & 0 & 1 & \frac{L}{\gamma_{rel}^2} \\ 0 & 0 & 0 & 0 & 0 & 1 \end{pmatrix}. \tag{2.21}$$

As an example for a matrix with interactions between the phase spaces of the different planes, the following matrix shows the transfer matrix for a sector bend with bending radius ρ_0, deflection angle α and the length L:

$$\mathbf{SB} = \begin{pmatrix} \cos\alpha & \rho_0\sin\alpha & 0 & 0 & 0 & \rho_0(1-\cos\alpha) \\ -\frac{\sin\alpha}{\rho_0} & \cos\alpha & 0 & 0 & 0 & \sin\alpha \\ 0 & 0 & 1 & \rho_0\alpha & 0 & 0 \\ 0 & 0 & 0 & 1 & 0 & 0 \\ -\sin\alpha & -\rho_0(1-\cos\alpha) & 0 & 0 & 1 & \rho_0\frac{\alpha}{\gamma_{rel}^2} - \rho_0(\alpha-\sin\alpha) \\ 0 & 0 & 0 & 0 & 0 & 1 \end{pmatrix}. \tag{2.22}$$

2.1.3 Stability criterion for transfer matrices

To get the transfer matrix $\mathbf{M}_{circ}$ for a complete turn, one has to multiply all single matrices of the lattice elements (cf. Eq. 2.18). To calculate the transfer matrix for n turns, one has to apply $\mathbf{M}_{circ}$ for n times:

$$\mathbf{M}_n = (\mathbf{M}_{circ})^n\,. \tag{2.23}$$

It is important to find out if there are constrains on the transfer matrices in order to run the machine stable. To get more information about the impact of a transfer matrix on the stability, one can investigate the eigenvalues of the matrix.

$$\mathbf{M}\,\vec{x} = \lambda\,\vec{x} \qquad \text{with} \qquad \vec{x} = \begin{pmatrix} x \\ x' \end{pmatrix} \tag{2.24}$$

Using Tr($\mathbf{M}$) $= 2\cos\mu$, one calculates:

$$\lambda_{1/2} = \exp \pm i\mu. \tag{2.25}$$

Excluding the case Tr($\mathbf{M}$) $= 2$, the matrix $\mathbf{M}$ can be expressed in a useful form applying the Twiss matrix:

$$\mathbf{M} = \mathbf{I}\ \cos\mu + \mathbf{J}\ \sin\mu \qquad \text{with} \qquad \mathbf{I} = \begin{pmatrix} 1 & 0 \\ 0 & 1 \end{pmatrix}, \quad \mathbf{J} = \begin{pmatrix} \alpha & \beta \\ -\gamma & -\alpha \end{pmatrix}. \tag{2.26}$$

With the Twiss parameters α, β and γ calculated with the elements m_{ij} of the matrix $\mathbf{M}$:

$$\alpha = \frac{m_{11} - m_{22}}{2\sin\mu}, \quad \beta = \frac{m_{12}}{\sin\mu}, \quad \gamma = -\frac{m_{21}}{\sin\mu}. \tag{2.27}$$

The transfer matrix for n turns is then:

$$\mathbf{M}^n = \mathbf{I}\ \cos n\mu + \mathbf{J}\ \sin n\mu. \tag{2.28}$$

For real μ, the elements of the matrix $\mathbf{M}^n$ oscillate but remain bounded for any n. But, for complex or imaginary μ, $\cos\mu$ and $\sin\mu$ will increase exponentially and the motion becomes unbounded [6]. This leads to the following constrains for the transfer matrices:

$$\text{Tr}(\mathbf{M}) < 2. \tag{2.29}$$

2.1.4 Solution of the Hill equation

To describe the Twiss parameters, one has to find the solution of the Hill equation [4,6]:

$$x''(s) + k(s)\, x(s) = 0, \tag{2.30}$$

with the periodicity $k(s+U) = k(s)$ and the circumference of the machine U.

Floquet's theorem assures two linearly independent solutions of the Hill equation which are:

$$\begin{aligned} x_m(s+U) &= x_m(s)\ \exp \pm i\mu & (2.31) \\ &= x_m(s)\ (\cos\mu \pm i\sin\mu), \qquad m = 1, 2. & (2.32) \end{aligned}$$

The solutions $x_m(s+U)$ and $x_m(s)$ are also correlated with the Twiss matrix:

$$\begin{pmatrix} x_m(s+U) \\ x'_m(s+U) \end{pmatrix} = \begin{pmatrix} \cos\mu + \alpha\sin\mu & \beta\sin\mu \\ -\gamma\sin\mu & \cos\mu - \sin\mu \end{pmatrix} \begin{pmatrix} x_m(s) \\ x'_m(s) \end{pmatrix} \tag{2.33}$$

For $x(s)$, this can also be written as:

$$x(s)\ (\cos\mu \pm i\sin\mu) = (\cos\mu + \alpha\sin\mu)\ x_m(s) + \beta\sin\mu\ x'_m(s). \tag{2.34}$$

Using Eq. 2.34 and the Hill equation, one can derive the following differential equation for β:

$$\frac{1}{2}\beta\beta'' - \frac{1}{4}\beta' + k\beta^2 = 1. \tag{2.35}$$

This equation shows the correlation between the Twiss parameter β and the focusing strength k. For constant k, one can calculate that $\beta = 1/\sqrt{k}$. The beta function $\beta(s)$ can be derived by solving Eq.2.35 numerically, but in most cases it will be derived from the transfer matrices for one turn. The other Twiss parameters are given by:

$$\alpha = -\frac{1}{2}\beta', \qquad \gamma = \frac{1+\alpha^2}{\beta}. \tag{2.36}$$

The independent solutions proposed by Floquet's theorem are:

$$x_m(s) = a_m\sqrt{\beta}\exp \pm\psi(s) \qquad \text{with} \qquad \psi = \int_0^s \frac{1}{\beta(t)}\,dt, \quad m = 1,2. \tag{2.37}$$

The general solution can be written as the linear combination of the two independent solutions

$$x(s) = a_1\sqrt{\beta(s)}\exp\left[i\psi(s)\right] + a_2\sqrt{\beta(s)}\exp\left[-i\psi(s)\right], \tag{2.38}$$

and the particle trajectory is described by a real solution:

$$x(s) = a\sqrt{\beta(s)}\cos\psi(s) + \psi_0). \tag{2.39}$$

The variables a and ψ_0 define the individual trajectory of the particle. Eq. 2.39 describes a quasi harmonic oscillation with variable amplitude $a\sqrt{\beta(s)}$ and variable wave number $d\psi/ds = 1/\beta(s)$. The number of oscillations per turn, known as the tune of the machine, is:

$$Q_{x,y} = \frac{1}{2\pi}\int_s^{s+U}\frac{dt}{\beta_{x,y}(t)}. \tag{2.40}$$

2.1.5 Machine ellipse

The trajectory of a particle in the phase space can be described by:

$$\begin{aligned} x(s) &= a\sqrt{\beta(s)}\cos\left(\psi(s)+\psi_0\right). & (2.41)\\ x'(s) &= -\frac{a}{\sqrt{\beta(s)}}\left[\alpha(s)\ \cos\left(\psi(s)+\psi_0\right) + \sin\left(\psi(s)+\psi_0\right)\right]. & (2.42)\end{aligned}$$

This equations represent an ellipse in the phase space like shown in Fig. 2.2.

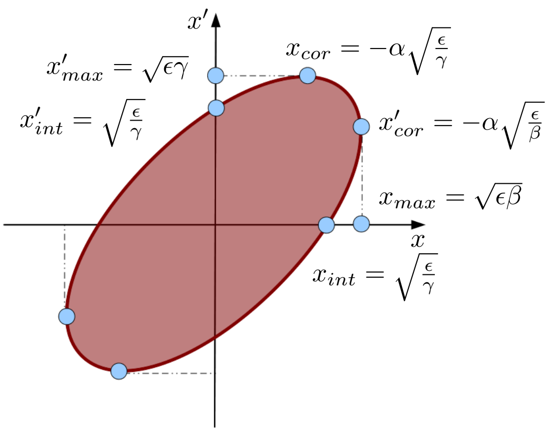

Figure 2.2: Phase ellipse in horizontal phase space. The significant positions are highlighted and defined.

The size of the phase ellipse's surface is a constant and can be derived by $A = \pi\ a^2$ with

$$\gamma x^2 + 2\alpha x x' + \beta x'^2 = a^2 \tag{2.43}$$

which is the Courant-Snyder invariant. The maximum amplitudes in x and x' direction are given by

$$x_{max} = \sqrt{\epsilon\beta} \qquad \text{and} \qquad x'_{max} = \sqrt{\epsilon\gamma} \tag{2.44}$$

using the emittance $\epsilon = a^2$. The physical interpretation of the Courant-Snyder invariant corresponds to [4]:

- A particle with the coordinates (x, x') moves in the phase space on the edge of an ellipse whose form is related to the particles' position in the lattice.
- The size of the ellipse's surface area defining the particles' movement is constant and given by the particles' amplitudes.
- The form of the ellipse is given by the lattice and can be displayed using the Twiss parameters α, β and γ.
- The phase ellipse defined by the Courant-Snyder invariant $a^2 = \epsilon$ describes the movement in phase space for all particles with betatron amplitudes smaller or equal to a.

2.1.6 Periodic dispersion

The periodic dispersion of the lattice is described by the differential equation [4]:

$$x'' + k_x(s)\, x = \frac{1}{\rho_0}\frac{\Delta p}{p_0}, \tag{2.45}$$

with the coefficients $k_x(s + U) = k_x(s)$ and $\rho_0(s + U) = \rho_0(s)$ whereas U is the circumference of the machine or the length of a super period of the lattice. Due to the relative momentum offset $\Delta p/p_0$, the particles will circulate the machine with an additional offset x_D compared to the closed orbit without momentum deviation.

$$x_D(s) = D(s)\frac{\Delta p}{p_0}. \tag{2.46}$$

The modified orbit is, like the orbit for particles with $\Delta p/p_0 = 0$, a periodic solution and $D(s)$ is the periodic dispersion of the lattice. The general solution of Eq. 2.45 is:

$$x(s) = x_D(s) + x_\beta(s). \tag{2.47}$$

with $x_D(s)$, the offset caused by the dispersion, and $x_\beta(s)$, the offset due to betatron oscillations.
Inserting Eq. 2.47 to Eq. 2.45, one can derive a differential equation for the dispersion:

$$D'' + k(s)\, D = \frac{1}{\rho(s)} \tag{2.48}$$

whose solution has to fulfill the periodicity conditions of the dispersion:

$$\begin{aligned} D(s+U) &= D(s) && (2.49)\\ D(s+U) &= D(s). && (2.50) \end{aligned}$$

To solve this differential equation, one has to chose a fixed starting point $s_0 = 0$ with D_0 and D'_0. The solutions at the position s is then identical with:

$$D(s) = D_0\, C(s) + D_0'\, S(s) + d(s). \tag{2.51}$$

In this connection, $d(s)$ is a special solution depending on the periodicity conditions and $C(s)$ respectively $S(s)$ are the cosine and sine like solutions of the homogeneous equation (cf. section 2.1.1). Comparing $D(s)$ with $D(s+U)$ and taking the periodicity conditions into account, one can derive the dispersion function:

$$D(s) = \frac{\sqrt{\beta(s)}}{2\sin\left(\frac{\mu}{2}\right)} \int_s^{s+C} \frac{1}{\rho(t)} \sqrt{\beta(t)}\, \cos\left(\psi(t) - \psi(s) - \frac{\mu}{2}\right) dt \qquad \text{with} \qquad \mu = \int_s^{s+U} \frac{dt}{\beta(t)}. \tag{2.52}$$

2.1.7 Edge focusing

Edge focusing effects appear when the closed orbit is not perpendicular to the pole faces of the magnets. Due to effects caused by field gradients, this leads to perturbations. For the description of the edge focusing, a fixed Cartesian coordinate system will be used whose z-axis is defined by the direction of the design orbit in the field-free area outside the magnet and whose origin is defined by the edge of the effective field.

A particle which arrives with an horizontal offset Δx at a rotated pole face with an angle β has to travel, depending on the sign of the offset, through a shorter respectively a longer part $\pm\Delta z$ of the magnet. This leads to an additional deflection which can be calculated using Eq. 2.53. The sign of the additional deflection depends on the particles offset and on the angle of the pole face rotation.

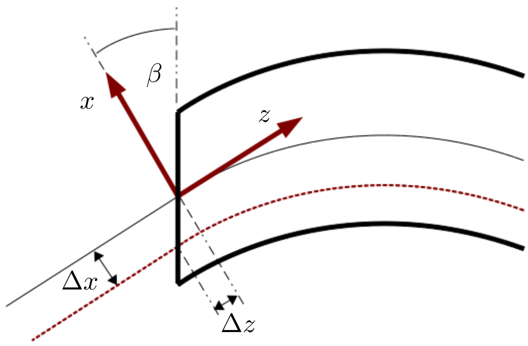

Figure 2.3: Schematic drawing related to the edge focusing effects at rotated pole faces showing the coordinate system used for the description

$$\Delta x' = \frac{\Delta z}{\rho_0} = \frac{\tan\beta}{\rho_o} x_0, \tag{2.53}$$

whereas β is the angle of the pole face rotation, x_0 the offset and ρ_0 the bending radius of the magnet.

A vertical offset Δy will lead to an impact on the particles caused by the fringe fields at the magnet edges. The kick, caused by a vertical offset, can be calculated by:

$$\Delta y' = \frac{1}{B_0 \rho_0} \int B_x\, dz, \tag{2.54}$$

with the maximum magnetic field B_0 and its radial component B_x. Using an appropriate coordinate system and integration path [4], B_x can be calculated and the formula for the additional vertical deflection can the be written as:

$$\Delta y' = -y_0 \frac{\tan\beta}{\rho_0}. \tag{2.55}$$

The transfer matrix for edge focusing can then be expressed as:

$$\mathbf{EF} = \begin{pmatrix} 1 & 0 & 0 & 0 & 0 & 0 \\ \frac{\tan\beta}{\rho_0} & 1 & 0 & 0 & 0 & 0 \\ 0 & 0 & 1 & 0 & 0 & 0 \\ 0 & 0 & -\frac{\tan\beta}{\rho_0} & 1 & 0 & 0 \\ 0 & 0 & 0 & 0 & 1 & 0 \\ 0 & 0 & 0 & 0 & 0 & 1 \end{pmatrix}. \tag{2.56}$$

2.1.8 Horizontal painting

The painting concept describes a filling scheme for the phase space ellipses which allows to control the distribution of the particles in order to mitigate direct space charge effects. To fill first the centre and then the outer areas of the phase ellipse, a closed orbit bump, the so called "painting bump", is necessary. The injection position has to be in a certain distance to the orbit of the circulating particles, but at the beginning of the injection, the trajectory of the incoming and the circulating beam have to be merged using the closed orbit bump. The particles injected during this time will execute betatron oscillation with small amplitudes, thus, they will fill the centre of the phase ellipse. The painting bump will decay during injection and, due to this, there will be an increasing offset between the injected and the circulating beam which leads to larger betatron oscillation amplitudes and, due to this, to a filling of the outer areas of the phase ellipse.
This horizontal painting scheme will be used for the Linac4 injection to the Booster. Fig. 2.4 shows on the left hand side the positions of the bunches after 5 injection turns and on the right hand side the function of a linearly decreasing painting bump.

The function for the painting bump decrease can also be changed to other characteristics than a linear one, and it is also possible to inject the particles with a small initial offset in order to get less particles in the centre of the phase ellipse.

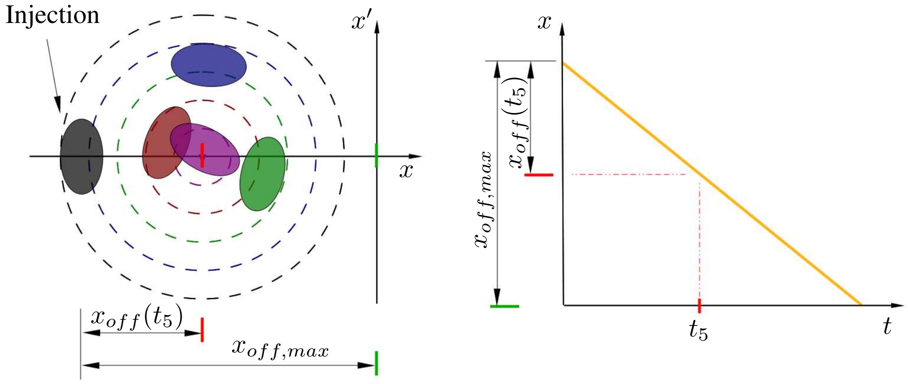

Figure 2.4: Horizontal painting. On the left hand side, the positions of the bunches after five injection turns (at the time t_5) using horizontal painting, are shown. The bunches execute betatron oscillations with different amplitudes depending on the offset between the injection position and the orbit of the circulating particles during injection time. The function presented on the right hand side shows a linearly decrease of the painting bump.

2.2 Longitudinal beam dynamics

This section will be concerned with the longitudinal beam dynamics as observed in a synchrotron with RF acceleration cavities. The acceleration and the synchrotron oscillations will be discussed and a filling scheme for the buckets, the longitudinal painting as used for the Linac4 injection, will be presented as well.

2.2.1 Acceleration and synchrotron movement

To accelerate particles in a synchrotron using a radio frequency field, the following condition between the rotational frequency of the particles ω_s and the accelerating radio frequency ω_{RF} has to be fulfilled:

$$\omega_{HF} = h\,\omega_s. \tag{2.57}$$

The harmonic number h has to be an integer value in order to allow constant acceleration during the cycle. The rotational frequencies in the Booster during injection with 160 MeV and ejection with 1.4 GeV are:

$$\omega_{s,\ 160\,\mathrm{MeV}} = 6.23 \times 10^6\ \frac{1}{s} \qquad \text{and} \qquad \omega_{s,\ 1.4\,\mathrm{GeV}} = 10.98 \times 10^6\ \frac{1}{s}. \tag{2.58}$$

As the main harmonic number $h = 1$ is used in the Booster (cf. section 3.1), these numbers are the same for the RF-frequency ω_{RF} for the respective particle energies.
Passing the acceleration cavities, the particles will gain a certain amount of energy which is related to the peak voltage of the RF U_0 and to the synchrotron phase ϕ which describes the relative position of the particle in comparison to the sine like RF wave:

$$\Delta E = q\,U_0\ \sin\phi. \tag{2.59}$$

A particle which has a certain phase $\phi = \phi_s$ is called the synchronous particle. This particle will pass the RF wave at each turn at exactly the same position and will gain the same energy every time. In each period of the RF, one can find two positions with the same voltage, one at the flank with positive and the other on the flank with negative slope, which means, that there are two positions where the particles with $\phi = \phi_s$ could be accelerated. More about the decision which slope of the RF has to be chosen – it depends on the behavior of the particles with $\phi \neq \phi_s$ – will be presented below. Assuming that the particles with higher energy than the synchronous particle accomplish one circulation in less time and arrive earlier at the cavity, i.e. they have a phase with $\phi > \phi_s$, then, the position of ϕ_s has to be chosen at the decreasing slope of the RF wave in order to accelerate particles with higher energy less and particles with lower energy more than the synchronous particle. Due to this, particles will carry out longitudinal oscillations around the synchronous phase ϕ_s which are called the synchrotron oscillations. For those oscillations, it is essential that the angular frequency ω is related to the momentum p of the particles:

$$\frac{\Delta\omega}{\omega} = \left(\frac{1}{\gamma_{rel}^2} - \frac{1}{\gamma_{tr}^2}\right)\frac{\Delta p}{p_0}. \tag{2.60}$$

Eq. 2.60 shows that the relative frequency deviation $\Delta\omega$ is related on the particles energy. Particles with an energy below the so called transition energy $E_{tr} = \gamma_{tr}\ E_0$ and with an positive momentum offset will circulate the machine in a shorter time than particles with the same energy and a negative momentum offset. This is the other way around for particles with an Energy above E_{tr}. The velocity of the particles with an energy below transition energy is still far away enough from the speed of light that means the velocity of these particles is increased significantly passing an acceleration cavity. Due to this, the particles with an positive momentum offset need less time for one turn than the particles with smaller or negative momentum offsets. The second effect, which is dominant for particle energies above the transition energy, is that particles with positive momentum offset will be bend on a larger radius than those with negative $\Delta p/p_0$.

This leads to a larger circumference and, as a result, to longer circulation times. The threshold value for the particle energy between the dominance of the two effects is the transition energy. Eq. 2.60 shows also that there will be no synchrotron movement and, due to this, no longitudinal focusing for $\gamma_{rel} = \gamma_{tr}$. For this reason, the particles have to cross the transition energy during acceleration as fast as possible in order to avoid a divergence of the bunch. γ_{tr} is related to the momentum compaction factor:

$$\alpha_P = \frac{1}{\gamma_{tr}^2} = \oint_U \frac{D(s)}{\rho}\, ds \tag{2.61}$$

with the dispersion $D(s)$, the bending radius of the machine ρ and the machine circumference U.

For the calculations of the synchrotron oscillations, the particle movement will be described relative to the synchronous particle, using

$$\Delta\phi = \phi - \phi_s, \qquad \Delta p = p - p_s, \qquad \Delta E = E - E_s, \qquad \Delta\omega = \omega - \omega_s. \tag{2.62}$$

For the variations of $\Delta\phi$ and ΔE, one can calculate [4]:

$$\delta(\Delta\phi) = -\eta_s \frac{\Delta p}{p_s} h\, 2\pi \tag{2.63}$$

$$\delta(\Delta E) = qU_0(\sin\phi - \sin\phi_s). \tag{2.64}$$

Divide this equations by the cycle period $T_s = 2\pi/\omega_s$:

$$\frac{d}{dt}\Delta\phi = -\frac{1}{T_s}\eta_s \frac{\Delta p}{p_s} h\, 2\pi = -\frac{h\eta_s\omega_s}{p_s v_s}\Delta E \tag{2.65}$$

$$\frac{d}{dt}\Delta E = \frac{1}{T_s} qU_0(\sin\phi - \sin\phi_s) = \frac{\omega_s}{2\pi} qU_0(\sin\phi - \sin\phi_s). \tag{2.66}$$

The variables $\eta_s, \omega_s, p_s, U_0$ and ϕ_s vary hardly and will be used as constants in order to simplify the calculation.

An additional differentiation d/dt applied on Eq. 2.65 gives the possibility to insert Eq. 2.66 and to combine both equations to one:

$$\frac{d^2}{dt^2}\Delta\phi = -\frac{h\eta_s\omega_s}{p_s v_s}\frac{d}{dt}\Delta E \tag{2.67}$$

$$= -\frac{h\eta_s\omega_s^2}{2\pi p_s v_s} qU_o(\sin\phi - \sin\phi_s). \tag{2.68}$$

Applying a linear approximation on $\sin\phi - \sin\phi_s$, valid for small ϕ, using $\sin\phi = \phi$ and $\cos\phi = 1$, one gets:

$$\sin\phi - \sin\phi_s \approx \cos(\phi)\Delta\phi. \tag{2.69}$$

Inserting this approximations to Eq. 2.68, one gets a differential equation for a harmonic oscillator:

$$\frac{d^2}{dt^2}\Delta\phi + \Omega^2\,\Delta\phi = 0 \qquad \text{with} \qquad \Omega = \sqrt{\frac{h\eta_s\omega_s^2}{2\pi p_s v_s} qU_o \cos\phi_s}. \tag{2.70}$$

The particles will carry out synchrotron oscillations with the frequency $f_{syn} = \Omega/2\pi$ if Ω is real. The condition for a real Ω is $\eta \cos\phi_s > 0$. Furthermore, one calculates the longitudinal tune with:

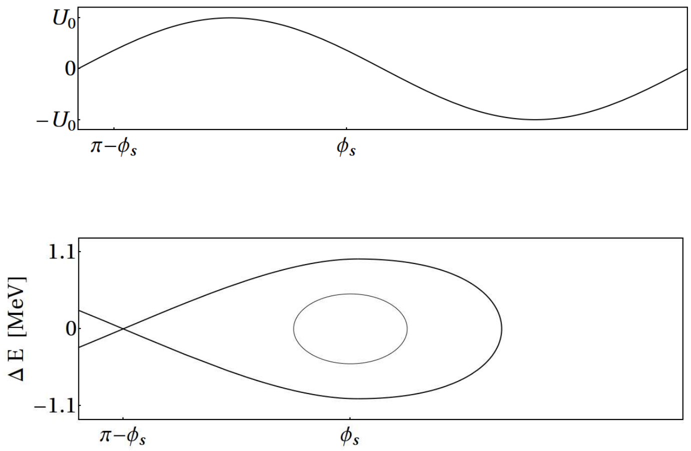

Figure 2.5: The upper plot shows the sine like RF wave and the lower plot the separatrix of the bucket which divides the areas for stable and unstable oscillation in the longitudinal phase space. The phase for the synchronous particle is labelled with ϕ_s.

$$Q_syn = \frac{\Omega}{\omega} = \sqrt{\frac{h\eta_s}{2\pi p_s v_s} qU_o \cos\phi_s}. \tag{2.71}$$

Using $\Delta\phi = \Delta\phi_0 \cos(\Omega t)$ as a solution of an harmonic oscillator and inserting to Eq. 2.65, one gets:

$$\Delta E = \Delta E_0 \sin \Omega t \qquad \text{with} \qquad \Delta E_0 = \frac{\Omega}{\omega_s} \frac{p_s v_s}{h\eta_s} \Delta\phi_0. \tag{2.72}$$

The solution of the harmonic oscillator $\Delta\phi = \Delta\phi_0 \cos(\Omega t)$ and Eq. 2.72 build a parametric equation of an ellipse as presented in Fig. 2.5. The synchrotron oscillation is a coupled oscillation in the $(\Delta\phi, \Delta E)$-plane and the amplitudes are depending on each other in the way as shown in Eq. 2.73 [4].

$$\Delta E_0 = Q_{syn} \frac{p_s v_s}{h\eta_s} \Delta\phi_0. \tag{2.73}$$

2.2.2 The physical emittance during acceleration

A particle with the velocity $\vec{v} = \vec{v}_x + \vec{v}_y + \vec{v}_z$ passing an acceleration structure will get a longitudinal kick, but the transversal velocities will stay unchanged. As a result, the angle x' between the direction of the particle's movement and the longitudinal axis will become smaller. This leads to a shrinking physical emittance during acceleration.

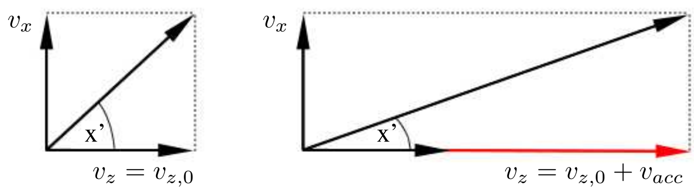

Figure 2.6: Impact of the acceleration on the particles velocity displayed for the horizontal plane.

However, the normalised emittance is a constant during acceleration and gives the possibility to calculate the size of the physical counterpart by:

$$\epsilon = \frac{\epsilon^*}{\beta_{rel}\gamma_{rel}}. \tag{2.74}$$

2.2.3 Longitudinal painting

In order to accelerate the particles as early as possible to mitigate direct space charge effects without being forced to apply a nonadiabatic capturing, the acceleration can be switched on during the injection and the beam will be then send to a "waiting" bucket. Longitudinal painting describes a filling scheme of the "waiting" buckets where the energy of the injected beam will be varied to fill the bucket with an equal density distribution to mitigate direct space charge effects. The beam energy has to be varied during injection e.g. from a positive to a negative energy deviation in order to fill the bucket from the upper to the lower edge. This circle can be applied several times for high intensity beams. For this injection method, a chopper is necessary which can stop the beam during the times the particles would be injected outside the buckets. A schematic drawing for the longitudinal painting scheme as described is shown in Fig. 2.7. The longitudinal painting will be used for the injection from Linac4 to the Booster.

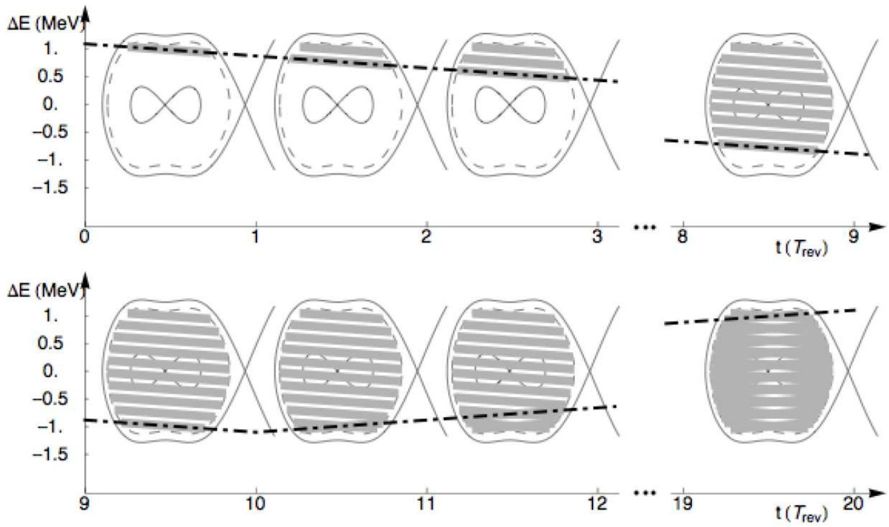

Figure 2.7: The filling scheme for the RF bucket applying longitudinal painting. The first injected beam will fill the bucket at the upper edge and the following particles will fill the areas below. The drawing shows a scheme were the energy deviation became smaller during the first 10 turns and raises then again to the initial value. [7].

2.3 Multiple scattering trough small angles

If a charged particle passes through material, it will be deflected by many small scatters [8]. The main part comes from Coulomb scattering from nuclei, and hence this effect is called multiple Coulomb scattering. The distribution is almost like a Gaussian distribution for small deflection angles but at larger angles it behaves like Rutherford scattering with more populated tails than a Gaussian distributions. For many applications it is sufficient to use a Gaussian distribution with a width given by:

$$\Theta \;=\; \frac{13.6}{\beta cp}\, Z\, \sqrt{x/X_0}\, [1 + 0.038\ \ln{(x/X_0)}] \qquad \text{for} \qquad 160\ \mu\text{m} < \text{x} < 16\ \text{m}. \tag{2.75}$$

Here, βc is the velocity, p the momentum of the particle, Z the charge number of the incident particle in units of proton charge and x/X_0 the thickness of the scattering medium in radiation length which is 16 cm for carbon [9]. Eq. 2.75 consists of two parts, the first part gives $\Theta \propto \sqrt{x}$ which is according to scattering at a thick foil and the second part with the additional $\ln x/X_0$ term takes the coulomb scattering into account. The second term leads to a smaller width and higher peaks. Using the parameters for protons and for a carbon foil with 300 $\frac{\mu g}{cm^2}$, applying Eq. 2.75 one calculates a width of:

$$\Theta_1 = 0.0734. \tag{2.76}$$

If the additional logarithmic term is not considered, which leads to a width proportional to the square root of x, one gets a width of:

$$\Theta_2 = 0.1321. \tag{2.77}$$

The particle distribution after passing the foil can be represented by a Gaussian approximation with mean 0 and width Θ_1 = 0.0734 using the formula as specified or with mean 0 and width Θ_2 = 0.1321, if the second part of Eq. 2.75 is neglected. The reason to neglect the second term for the calculation of Θ_2 was the assumption that one of the scattering models implemented to ORBIT uses this approximation as well. The width Θ_2 was calculated to compare the theoretical value with the width of a distribution after a scattering with the ORBIT model (cf. section 5.3.4).

2.4 Direct space charge effects

For beams with low energy and height particle density like the beams injected from Linac4 to the Booster, it is necessary to include direct space charge effects to the simulations. These effects are caused by the Lorentz forces between the charged particles and, because these forces will decrease for higher particles energies, accelerating the particle will mitigate them. In this chapter, the basic calculations concerning the direct space charge effects will be presented [4,5].
The calculations for the Lorentz forces between the particles will be based on the assumption that the particles are evenly distributed in a cylindrical bunch with infinitive length like shown in Fig. 2.8.

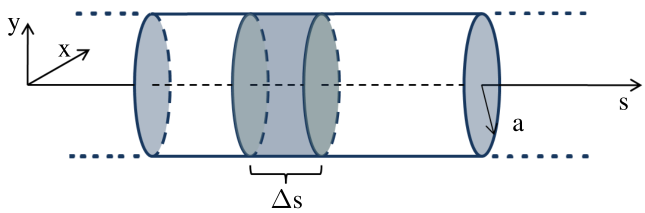

Figure 2.8: Schematic drawing of a cylindrical bunch.

In this model, the beam current I, the particle density ρ and the current flux j can be described as:

$$I = \frac{N\,\beta_{rel}c}{U}, \qquad \rho = \frac{I}{\pi\, a^2\, \beta_{rel}c}, \qquad j = \frac{I}{\pi\, a^2}. \tag{2.78}$$

Where U is the circumference of the machine and a the envelope of the beam. Using this definitions, one can calculate the electric and magnetic field applying Gauss's and Ampere's law. Due to the cylindrical symmetry of the bunch with an infinite length, there are just radial components for the electric and azimuthal components for the magnetic field caused by the particle distribution.

The electric field can be calculated by:

$$\epsilon_0 \int_{\partial S} \vec{E}\, d\vec{S} = \int_{\partial V} dV \tag{2.79}$$

$$\Leftrightarrow \quad 2\pi\, r\, s\, \epsilon_0\, E_r = \rho\, \pi\, r^2\, s$$

$$\Leftrightarrow \quad E_r = \frac{\rho\, r}{2\epsilon_0} \qquad \text{Insert } \rho \text{ from Eq.2.78}$$

$$= \frac{I\, r}{\pi\, a^2\, \beta_{rel} c},, \tag{2.80}$$

and the magnetic field can be calculated by:

$$\int_{\partial r} \vec{B}\, d\vec{r} = \mu_0 \int_{\partial S} \vec{j}\, d\vec{S} \tag{2.81}$$

$$\Leftrightarrow \quad 2\, s\, B\phi = \mu_0\, j\, r\, s$$

$$\Leftrightarrow \quad B_\phi = \frac{\mu_0\, j\, r}{2}. \tag{2.82}$$

Use $B_\phi = \frac{\beta_{rel}}{c}\, E_r$ to calculate the Lorentz forces on the particles which will be needed for the equation of motion:

$$\vec{F} = q(\vec{E} - \vec{v} \times \vec{B}) \tag{2.83}$$

$$= q(E_r - \beta_{rel} \gamma B_\phi)$$

$$= q(1 - \beta_{rel}^2) E_r$$

$$= \frac{qE_r}{\gamma_{rel}^2}. \tag{2.84}$$

Insert $\frac{d^2r}{dt^2} = \beta_{rel}^2 c^2 \frac{d^2r}{ds^2}$ and Eq. 2.80 to the equation of motion which is given by Eq. 2.85:

$$\gamma_{rel} m \frac{d^2r}{dt^2} = \frac{q\, E_r}{\gamma_{rel}^2} \tag{2.85}$$

$$\Leftrightarrow \quad \frac{d^2r}{ds^2} = \frac{q\, I}{2\pi\, m\epsilon_0\, a^2\, \beta_{rel}^3\, \gamma_{rel}^3\, c^3}\, r$$

$$= \frac{\kappa}{a^2}\, r. \tag{2.86}$$

The general perveance

$$\kappa = \frac{q\, I}{2\pi\, m\epsilon_0\, \beta_{rel}^3\, \gamma_{rel}^3\, c^3}, \tag{2.87}$$

is a notion used in the description of charged particle beams. The value of the perveance indicates how significant the space charge effect is on the beam's motion. The term is used primarily for low-energy beams, in which motion is dominated by the space charge [10].

κ can also be defined as:

$$\kappa = \frac{2\ I}{I_0 \beta_{rel}^3 \gamma_{rel}^3}, \tag{2.88}$$

using the Alven-current:

$$I_0 = \frac{4\pi\ \epsilon_0\ mc^3}{q}. \tag{2.89}$$

For the further calculations, the smooth approximation model will be used with the same tune in both planes Q = Q_x = Q_y, also the same emittances $\epsilon = \epsilon_x = \epsilon_y$ and the same focusing strength at all positions of the lattice $k_0 = k_x(s) = k_y(s)$.

The focusing strength is expressed by: $k_0 = \frac{2\pi\ Q_0}{U}$.

Due to the fact that the focusing strength is the same at all positions, also the beta function is constant.

$$\beta(s) = \beta_0 = \frac{1}{k_0} = \frac{U}{2\pi\ Q_0}. \tag{2.90}$$

Then, the envelope equation is given by:

$$K\ a - \frac{\epsilon^2}{a^3} = 0 \qquad \text{with} \tag{2.91}$$

$$K = k_0\ a - \frac{\kappa}{a^2}. \tag{2.92}$$

The combined focusing strength K shows that the space charge effects affect on the beam like a defocusing quadrupole with strength κ.
Using this fact, the calculations of the tune shift caused by the direct space charge effects can be achieved.

The general formula for the tune shift is:

$$\Delta Q \quad = \quad \frac{1}{4\pi} \oint \beta(s)\ \Delta k(s)\ ds \tag{2.93}$$

and for the smooth approximation model:

$$\Delta Q \quad = \quad \frac{1}{4\pi} \oint \beta_0\ \frac{\kappa}{a^2}\ ds \qquad \text{Insert Eq. 2.88} \tag{2.94}$$

$$= \quad -\frac{C}{4\pi} \frac{I\ q\ \beta_0}{a^2\ \beta_{rel}^3 \gamma_{rel}^3 I_0}. \tag{2.95}$$

Using I from Eq. 2.78 and $\epsilon^* = \epsilon\ \beta_{rel}\gamma_{rel}$, one gets the formula for the tune shift:

$$\Delta Q \quad = \quad -\frac{Ne}{2\pi\ I_0\ \epsilon^* \beta_{rel} \gamma^2}. \tag{2.96}$$

The tune shift caused by the direct space charge effects is proportional to the number of particles in the ring N and inverse proportional to the normalised emittance ϵ and to the relativistic factors β_{rel} and γ_{rel}^2.

$$\Delta Q \propto \frac{N}{\epsilon^*\ \beta_{rel} \gamma^2}. \tag{2.97}$$

2.5 Emittance calculations in the Booster measurement line

To get the values of the emittances of the beam in the Booster, one has to send the beam to the measurement line where the particle distribution will be measured with profile monitors at three different positions. The transfer matrices between the measuring points are well known and the betatron phase advance is μ = 60° in each case. The Twiss functions α and β are theoretically known at the monitor positions, but due to perturbations and misalignment in the transfer line, the real values can be slightly different. Using three positions for the measurements enables to calculate the actual values for α, β and the emittance ϵ. To this end, the theoretical values for α, β and the measured data of the first measurement point are taken to describe the phase ellipse of the beam in the normalised phase space using a coordinate system with $\xi = x/\sqrt{\beta_x}$ and $\xi' = d\xi/d\mu_s$. In this description, the phase ellipse is a circle with radius $r = \sigma_x/\sqrt{\beta_x}$ as shown in Fig. 2.9, and the transfer matrices between two positions can be easily described by rotation matrices. For this reason, the theoretical values of the width of the particle distributions at the two other places can be calculated and compared with the measured data in order to calculate the real values for α, β and the value for ϵ. For this calculations, the values for the dispersion and for the momentum offset are also required, because these variables cause an additional particle offset with $x_D = D\ \Delta p/p_0$. For the dispersion, the theoretical value is used and the momentum offset has to be measured before (cf. section 4.1)

To cover all sides of the phase ellipse, a μ = 60° betatron phase advance is the best solution applying 3 measurements. The three different measurement positions are represented by the dashed lines with three different colors in Fig. 2.9.

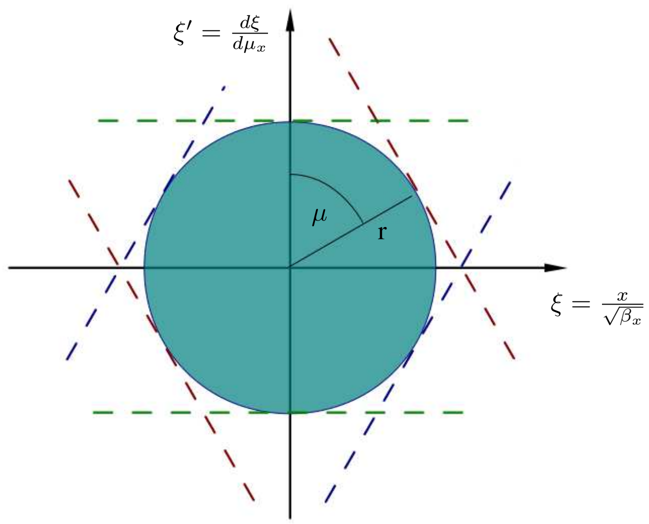

Figure 2.9: Emittance measurement in the normalised phase space. The dashed lines represent the three measurements at positions with $\mu = 60°$ betatron phase advance in between.

Chapter 3

The linear accelerators and the Proton Synchrotron Booster at CERN

3.1 Proton Synchrotron Booster

In this chapter, all accelerators used for the simulations will be described. This includes Linac2 and Linac4 as well as the PS Booster and, for both linacs, the injection to the Booster. Furthermore, the reason to change from Linac2 to Linac4 and with it from a conventional multiturn injection for protons to a H^- charge exchange injection as well as the change from 50 MeV to 160 MeV injection energy will be described.

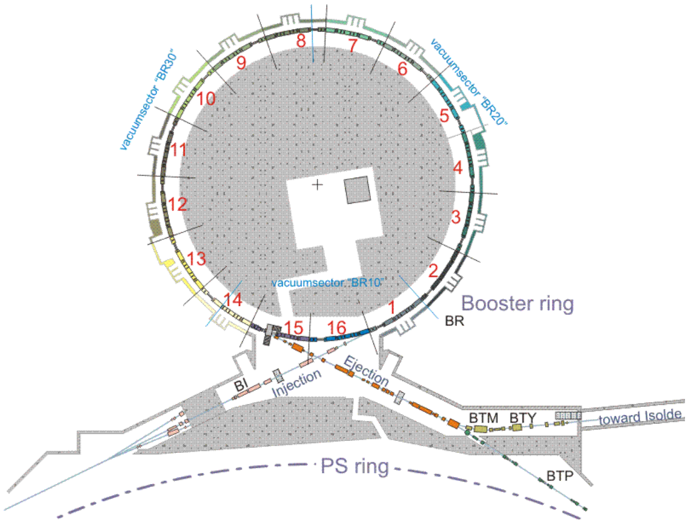

Figure 3.1: Proton Synchrotron Booster layout [11], showing the 16 periods of the Booster as well as the injection and ejection lines and a part of the transfer lines to the PS and the ISOLDE experiment.

The PS Booster is the first synchrotron of the LHC proton injection chain. At present, the Booster injector is Linac2, which will be replaced by Linac4 in 2015. Linac2 provides 50 MeV protons which are injected to the Booster via a conventional multi turn injection with a septum magnet. However, Linac4 will accelerate H^- ions up to 160 MeV and inject them to the PS Booster using a charge exchange injection. Fig. 3.1 shows the Booster layout.

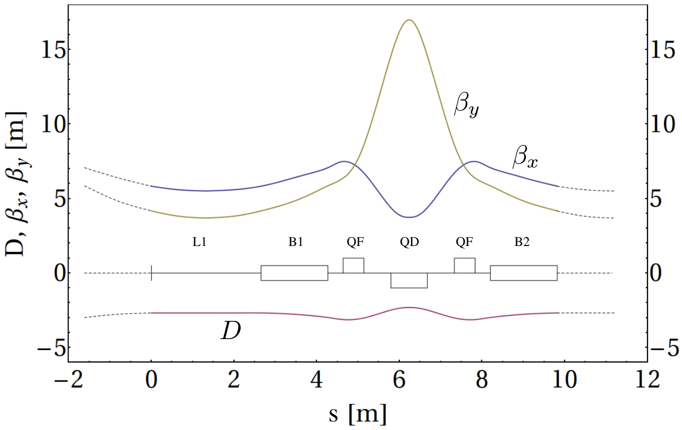

Figure 3.2: Regular period of the PS Booster.

The Booster consists of four rings, one upon the other, with a circumference of 157.08 m and a distance of 36 cm between them. Each Booster ring is subdivided in 16 periods with a length of 9.82 m and all rings are filled by one linac. As a result, fast vertical distributor and septum magnets (cf. section 3.2.1) are required to fill them one after the other. The motivation to stack four accelerator rings on top of each other is that the beam intensity, provided by the Booster, can be four times higher than for one ring using the same repetition rate. Fig. 3.2 shows a regular Booster period.

Due to the small distances between the rings, the magnets of each ring will also affect on the rings next to them. This leads to additional multipole components, especially in ring 1 and 4, caused by the missing vertical symmetry of the magnetic fields. Thus, the performances of the Booster rings 1 and 4 is not as good as the performance of the inner rings, in particular with the "old" working point (vertical tune one unit higher than at present) used up to 2005.

Each period contains two bending magnets as well as two horizontal focusing and one horizontal defocusing quadrupole magnet. The defocusing quadrupole is thereby longer than the focusing magnets. The drift spaces are filled with additional magnets to mitigate non-linear effects, beam diagnostic equipment and with the acceleration cavities. The elements used for injection and ejection are in the periods 1 and 16 respectively.

The injection energy with Linac2 is 50 MeV. In 1972, the Booster was built to accelerate the protons up to 800 MeV, but in the meanwhile, the Booster ejection energy has been increased and the protons get

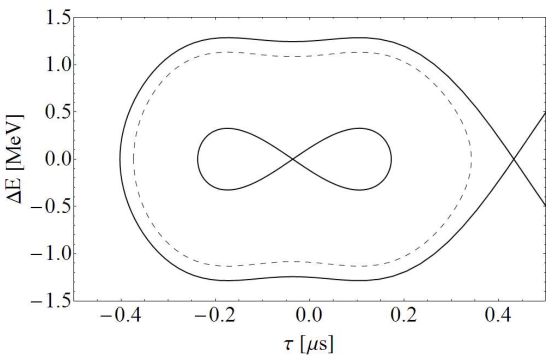

Figure 3.3: Flatted bucket of the applied double harmonic system [7].

accelerated up to 1.4 GeV. There are also discussions about to increase the maximum energy again up to 2 GeV. Either 1.4 GeV or 2 GeV will be the maximum energy with Linac4 protons, obtained by the H^- stripping, although the injection energy is higher than with Linac2. One machine circle, lasts 1.2 seconds and of which the acceleration of the protons will take a bit less than 500 ms. The protons need roughly 1 μs to 0.6 μs for one turn in the Booster, due to this, they circle the Booster 500 000 times during the acceleration. To accelerate the protons, a double harmonic system with two cavities is used. The main cavity with a harmonic number $h = 1$ and a second cavity, positioned in period 13, with $h = 2$. This leads to flatter buckets and to mitigated direct space charge effects. After accelerating the particles in the Booster, they can be directed either to the next synchrotron of the accelerator chain, the Proton Synchrotron (PS), or directly to the experiment ISOLDE. Fig. 3.3 shows a bucket for a double harmonic system calculated and used for the simulations like presented in this thesis.

3.1.1 Booster improvement programme

Transverse direct space charge detuning is the main performance limitation of the PS Booster. This is due to the fact, that the protons, which are injected to the Booster, are not relativistic (cf. section 2.4). A tune footprint for a typical simulation is given in Fig. 3.4. One notes the large tune spreads and that individual particles are close to low order resonances.

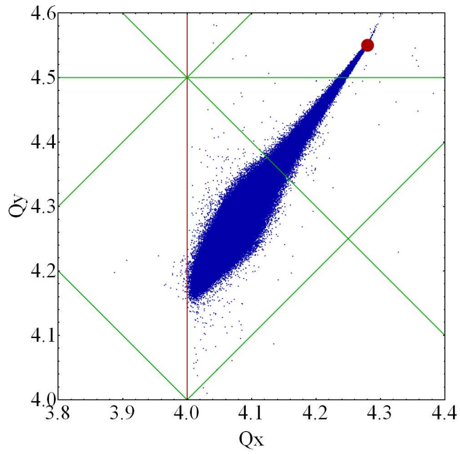

Figure 3.4: Tune footprint for the active compensation scheme (cf. sections 3.3.3 and 5.3.8) after 5000 turns. The red point marks the injection tune of the machine. The tune shift is different for each particle, as a result, the working points of all beam particles cover an area in the resonance diagram. The main reason for the tune shifts are the strong direct space charge forces between the particles.

Several measures to mitigate direct space charge effects have been implemented and are mandatory for highest performance:

- The mentioned double harmonic RF system will flatten the buckets and, in turn, the bunches. This reduces the maximum longitudinal forces between the protons.
- A dynamic working point allows a vertical injection tune above the half-integer resonance at $2Q_y = 9$. During the acceleration, the working point moves below the resonance (cf. section 3.1.2).
- Resonance compensation of the half-integer resonance at $2Q_y = 9$ and of third order resonances are implemented at the Booster.

- The Laslett tune shift, caused by the direct space charge effects (cf. section 2.4), is depending on the relativistic factors β_{rel} and γ_{rel}, the normalised emittance ϵ^* and on the number of particles N in the ring:

$$\Delta Q \; = \; \frac{N}{\epsilon^* \; \beta_{rel} \; \gamma_{rel}^2} \tag{3.1}$$

A higher beam energy leads to a smaller Laslett tune shift. If the same ΔQ can be accepted and the same normalised emittance should be used, a higher injection energy allows higher intensity. It is essential for 50 MeV and 160 MeV protons that:

$$(\beta_{rel} \; \gamma_{rel}^2)_{160MeV} \; = \; 2 \, (\beta_{rel} \; \gamma_{rel}^2)_{50MeV}. \tag{3.2}$$

The factor 2 for the $\beta_{rel} \; \gamma_{rel}^2$ allows to double the beam intensity keeping the same emittances and Laslett tune shifts. As a result, the launch of the Linac4 will allow higher intensity beams accelerated in the Booster.

3.1.2 Variable tune

To avoid a tune footprint crossing of the integer resonances at Q_x = 4 or Q_y = 4, in spite of a tune shift of roughly $\Delta Q = -0.5$ in vertical plane, the injection working point of the PS Booster has to be, at least for hight intensity beam, above the vertical half-integer resonance at $2Q_y$ = 9. Due to this, the tune footprint will cross the half-integer resonance which can lead to particle losses. But the number of lost particles will be smaller than for a crossing of an integer resonance.

The direct space charge effects and the size of the tune footprint are related to the energy of the beam (cf Eq. 3.1.1). During acceleration, the tune footprint will shrink and the machine tune can be moved below the half-integer resonance without pushing the particles over one of the integer resonances Q_y = 4 or Q_x = 4.

3.2 PSB injection with Linac2

Linac2 provides pulsed 0.83 Hz proton beams with a maximum beam current of 175 mA and an energy of 50 Mev. First beam in Linac2 was accelerated to 50 MeV on September 6th in 1978 and the operation with Linac2 started in 1979. Linac2 is a three tank, post coupled stabilised, drift tube linac based on an Alvarez structure and with quadrupole focusing. The first pre-accelerator for Linac2 was a Cockcroft-Walton accelerator which is now replaced by a four vane radio frequency quadrupole with injection energy of 92 KeV and ejection energy of 750 KeV. The source of Linac2 is of duoplasmatron type delivering a maximum current of 300 mA [12]. The RF voltage of the Booster cavities is set to the minimum possible during injection (negligible for beam dynamics). After injection, the capturing of the beam takes about 1 ms which is in the range of the synchrotron oscillation period and not adiabatic. The duration of the capture process is the compromise between two contrarily requirements:

- The magnetic field ramp rate at injection should be large to accelerate the beam and, as a result, reduce direct space charge effects quickly. This leads to short duration of the capture process.

- Capture should be slow to reduce non-adiabatic effects.

3.2.1 Injection and ejection hardware

The Fig. 3.5 and Fig. 3.6 show a part of the injection elements for injecting the Linac2 beam into the PS Booster. The injection line is roughly 80 meters long and contains many diagnostic devises and magnetic elements. Not all parts will be described, but the elements for the vertical distribution of the beam to the four Booster rings. All magnets described are shown in the sketch in Fig. 3.5 and are highlighted by a red circle in Fig. 3.6. The distributor magnet BI.DIS deflects the beam with different small angles depending on the destination Booster ring. A second distributor magnet, BI.DIS Pb, was used for the ion injection from Linac3, which used the same injection line as Linac2. As the ions are now accumulated and accelerated in the LEIR synchrotron, the second distributor magnet is switched off. At the position of the vertical septum magnet BI.SMV, the beams for the different rings are already slightly separated and the septum magnet deflects them to the selected rings. Finally, dipoles, named BI.BVT, deflect the beams into the rings. The horizontal septum magnet BI.SMH, which is a part of the injection section of the Booster and not shown in the sketch in Fig. 3.5, is necessary for the conventional multi turn injection (cf. section 3.2.2).

The ejection line, as presented in Fig. 3.7 and in the sketch in Fig. 3.5, combines the beams out of the four Booster rings onto one trajectory. Therefore, one needs several septum and kicker magnets as shown in the plots. First, the two beams of the upper and the lower rings are deflected by the dipole magnets BT1.BTV 10 and BT4.BTV 10 towards the beams of the inner rings. In the next steps, the upper and the lower beams get almost parallelised by the septum magnets BT1.SMV 10 & BT4.SMV 10 and combined in the kicker magnets BT4.KFA 10 & BT1.KFA 10. Then, the same principle is used to combine the two remaining beams to one beam using the dipole BT.BVT 20 to deflect the lower beam upwards and the vertical septum magnet BT.SMV 20 to send the beams to the kicker BT.KFA 20 where they are merged to one beam.

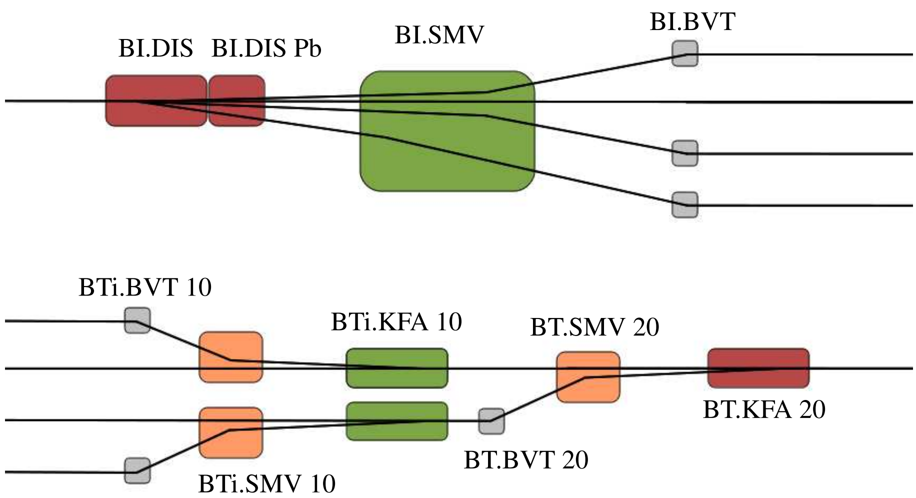

Figure 3.5: Injection and ejection elements. The upper plot shows a sketch of injection elements and the lower plot for the ejection elements.

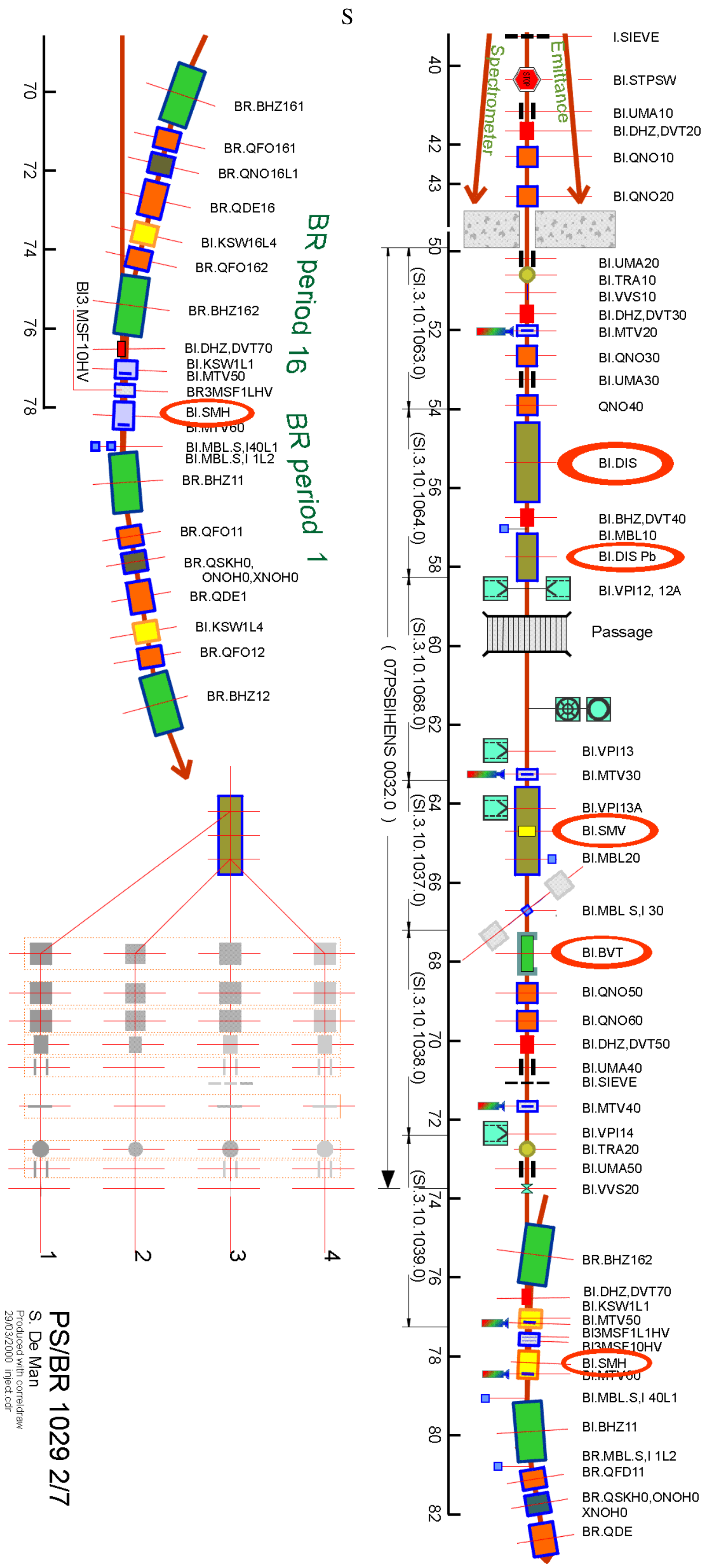

Figure 3.6: Sketch of the injection from Linac2 to PS Booster [11].

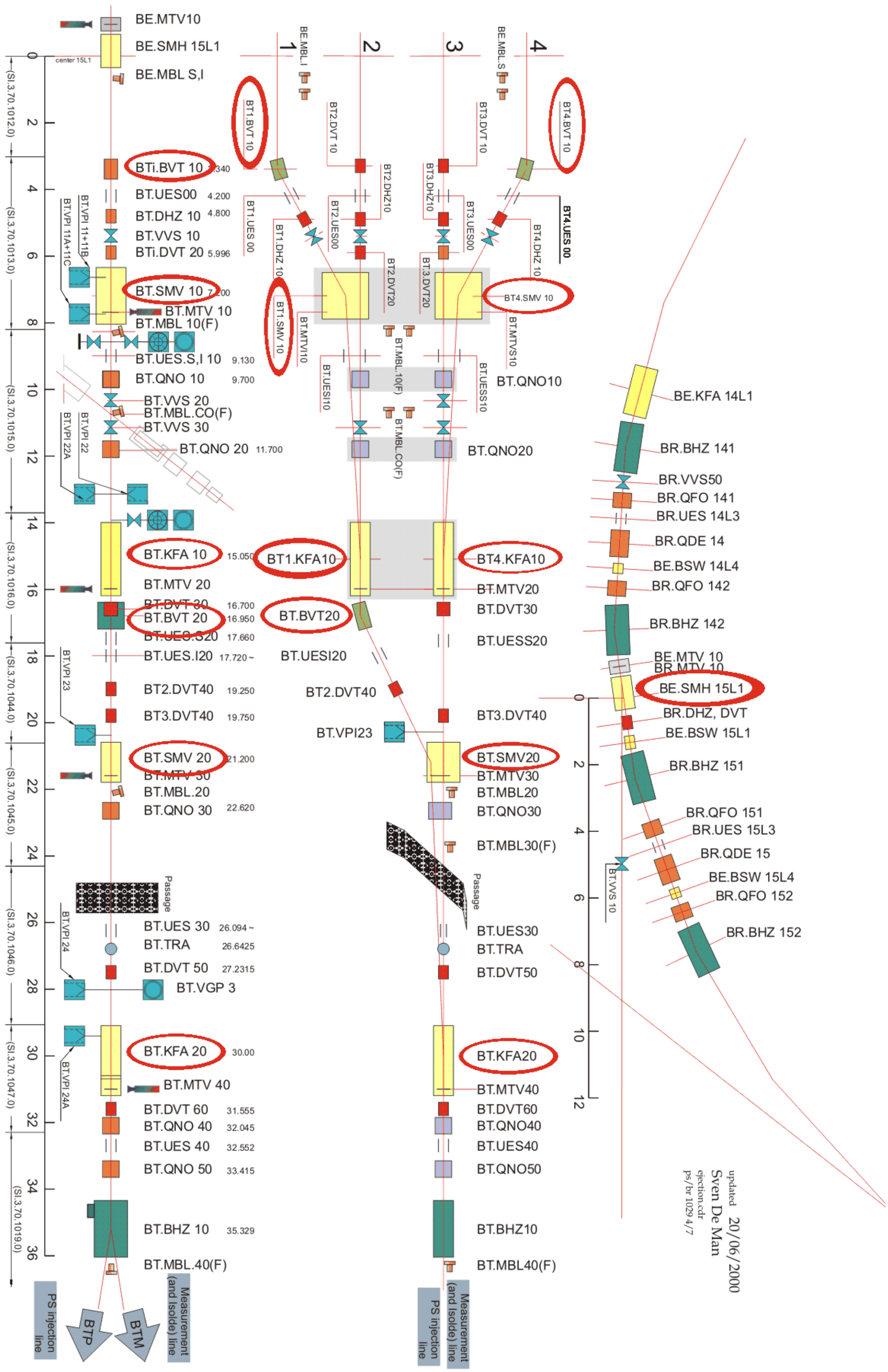

Figure 3.7: Sketch of the Booster ejection as used with Linac2 [11]. The beam can be directed either to the PS or to the ISOLDE experiment.

3.2.2 Conventional multi turn injection

To inject a high intensity beam to the PS Booster, 13 injection turns from Linac2 are necessary to accumulate the required number of protons. The particles are injected to the Booster via a conventional multi turn injection using a closed orbit bump and a septum magnet. Fig. 3.8 shows on the left the bunch positions in horizontal phase space after 5 injection turns using a conventional multi turn injection and on the right hand side the movement of the first bunch during 5 turns. The horizontal tune used for the drawings is the one used in operation for injection of the Booster with a non-linear part of 0.28. At the beginning of the first injection, the closed orbit bump is at it's maximum and the bunch passes the septum magnet at the outer side. Due to the offset between the design orbit and the injected beam, the particles will execute betatron oscillations and one has to take care that the bunch will not hit the septum magnet. During the first turns this is achieved by betatron oscillations. After a few turns, when the bunch arrives at the septum with a betatron phase similar to the initial one, the decrease of the bump leads to increase of the distance between injected and circulating beam. Thus, the particles injected later oscillate with larger amplitudes. This procedure, using a septum magnet splitting the injecting from the circulating beam, prohibits to inject twice to the same phase space volume. This requires a high intensity beam already from the Lina2 to accumulate the protons within a certain emittance.

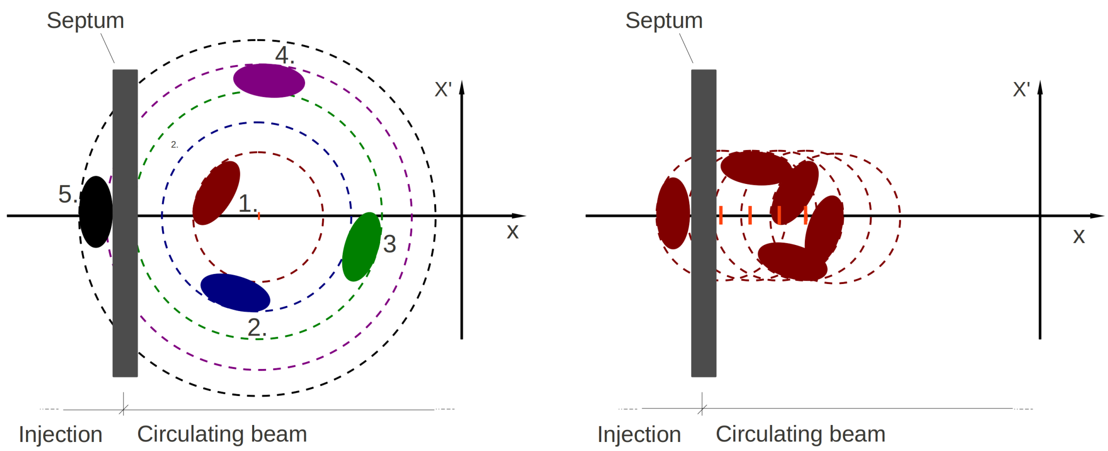

Figure 3.8: Principle of a conventional multi turn injection in horizontal phase space. The plot on the left hand side shows the distribution of 5 bunches at the 5$^{\text{th}}$ injection turn. The plot on the right shows the movement of one bunch from the injection to the position after 5 turns. The red marks at the x-axis show the positions of the design orbit during the decay of the bump.

3.3 PSB injection with Linac4

Linac4 is a normal conducting linear accelerator which will replace Linac2 in 2015. In a first stage, Linac4 will serve as Booster injector, but later may become the pre-accelerator for the future Superconducting Proton Linac (SPL) which is under study to replace the Booster and accelerate the H^- ions up to 3.5 GeV.

The main motivation for Linac4 is to double the intensity of the beam provided by the Booster. Furthermore, the H^- injection from Linac4 to the Booster, including horizontal and longitudinal painting, enables more options to adjust the beam properties and to improve the performance of the Booster.

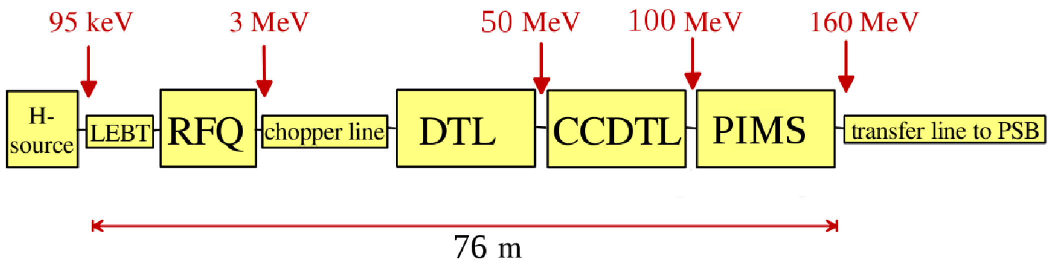

Figure 3.9: Structure of Linac4 [14].

Linac 4 consists of several parts: a drift tube linac (DTL) up to an energy of 50 MeV, a cell-coupled drift tube linac (CCDTL) from 50 to 100 MeV and a Pi-mode structure (PIMS) from 100 to 160 MeV (CERN PS Booster injection) respectively 180 MeV (SPL front-end). The frequency of the Linac4 cavities is 352.2 MHz [13]. As Booster injector, the maximum repetition rate is limited to 2 Hz and the beam pulse length to 400 μs. The average (after chopping) beam current, provided by Linac4, will be 40 mA [14]. Fig. 3.9 shows the structure of Linac4.

The higher injection energy of Linac4, compared with the 50 MeV injection energy of Linac2, will mitigate space charge effects in the Booster, hence the intensity of the beam can be doubled keeping the same normalised emittance and the same Laslett tune shift. The equal dimensions of the tune footprint requires, also for the injection with Linac4, an injection tune above the half integer resonance at 2 Q_y = 9 which will move to a lower working point when the tune footprint becomes smaller due to acceleration (cf. section 3.1.2).

The Booster injection section as currently used is adapted to the Linac2 proton multiturn injection and has to be replaced by a new injection section for the H^- charge exchange injection as required for Linac4 (cf. section 3.3.2).
The H^- injection will allow implementing the transversal and the longitudinal painting schemes (cf. section 2.1.8 and 2.2.3) and, in contrary to the Linac2 injection, the RF will be switched on during injection for the generation of most operational beams and, in particular, for high intensity and high brightness LHC beams. This allows, increasing the acceleration at injection, to reduce direct space charge effects quickly and avoids the perturbations caused by a nonadiabatic RF capturing of the beam like with the Linac2. A chopper, installed after the RFQ and before the first DTL section of Linac4, allows to inject particles just to the "waiting" buckets to assure that all particles in the Booster get accelerated as foreseen.

3.3.1 Injection to the 4 Booster rings

The distribution of the particles from the Linac4 transfer line to the four Booster rings is realised, like for Linac2, with vertical kickers and septum magnets [14]. Fig. 3.10 shows the distribution scheme in two plots. The beam will be vertically deflected by the five BI.DIS distributor magnets, which are pulsed ferrite core kickers, with different angles in order to guide the particles to the appropriate gaps of the septum magnet system BI.SMV which deflects the them to the Booster rings. New investigations have shown, no head dump, nor a tail dump (like shown in Fig. 3.10) will be required any more with Linac4, since the 3 MeV chopper will stop ions before and after filling Booster rings.

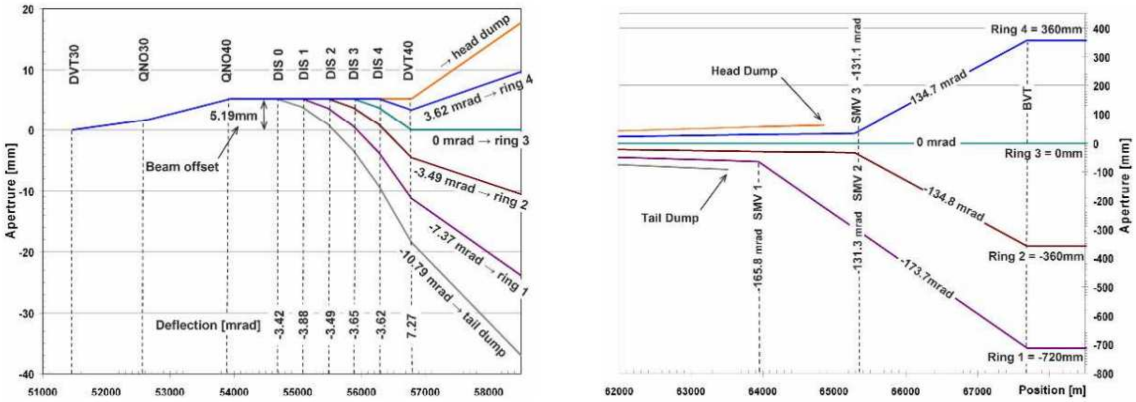

Figure 3.10: Scheme of the distributor and septum magnets to lead the Linac4 beam to the four Booster rings [14].

3.3.2 H$^-$ charge exchange injection

An H$^-$ injection, as sketched in Fig. 3.11, uses the fact that the injected H$^-$ ions and the protons circulating in the machine, have opposite charges. Hence, it is possible to merge the circulating and the incoming beam using a dipole magnet where the two beams will be deflected in opposite directions. To accomplish this, one needs a horizontal closed orbit bump and a stripping foil to convert the H$^-$ ions to protons by removing the electrons after the beams are merged. This closed orbit bump, named the "chicane", consists in the case of the Booster with Linac4 of four dipole magnets with 66 mrad deflection which are positioned in the Booster sections 1 and are symmetrically arranged around the stripping foil. The first dipole, BS1, deflects the circulating beam outwards, the second magnet, BS2, merges the two beams and, after stripping the electrons of the H$^-$ ions, the "new" proton beam will be deflected backward to the normal design orbit of the Booster by the dipole magnets BS3 and BS4. The stripping foil is a thin carbon foil with a thickness of around 300 $\mu g/cm^2$ which will strip more than 99 percent of all H$^-$ ions [9]. To avoid overheating of the foil and a reduction of the Booster performance due to proton scattering, the beam has to be moved away from the foil as quickly as possible, thus, the chicane has to decrease after injection.

One advantage of a H$^-$ injection is that there is no septum magnet necessary like for conventional multi turn injection of protons like the one used with Linac2. The septum separates the horizontal space in a region for the circulating and another one for the injected beam (cf. section 3.2.2). As a result, it is not possible to inject twice into the same phase space volume. However, H$^-$ charge exchange injection like for Linac4 allows to inject several times to the same phase space volume. Hence, the lower beam current available with linac4 is sufficient with the H$^-$ charge exchange injection. Horizontal phase space occupied by the beam during an H$^-$ injection is sketched in Fig.3.12.

The space available for the new Linac4 injection section of the Booster is the same as for the multi turn injection used with Linac2 and not flexible. All new elements have to be built compactly to install all hardware needed within the available space of 2.56 m. As a result, also the chicane bending magnets have to be as short as possible and they will have a length of 0.37 m. To achieve a beam deflection of 66 mrad using this short dipole magnets, a magnetic field of 0.29 T is required.

The chicane will be at it's maximum range of 45.9 mm during injection and she will decrease linearly after the injection. Assuming rectangular BS bending magnets, the beam will leave the magnets BS1 and BS3 and will enter the magnets BS2 and BS4 non perpendicular to the pole faces as long as the chicane is not fully decreased. As a result, edge focusing effects will occur at these pole faces and perturb the vertical be-

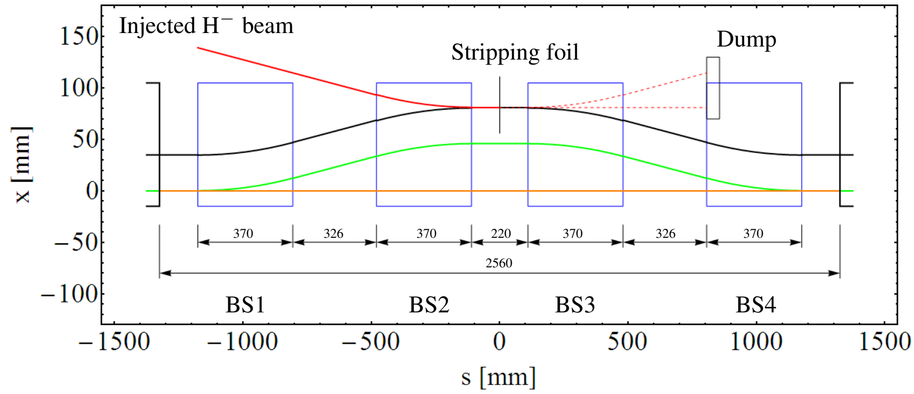

Figure 3.11: Scheme of a H^- injection chicane. The black solid line represents the trajectory of the circulating beam at the beginning of the injection including the chicane as well as the painting bump. The green dashed line shows the trajectory after injection when the painting bump is already decreased but the chicane is still at its maximum. After the chicane fall, the particles are not deflected any more and will follow the orange dashed line. The injected H^- beam is displayed by the red solid line top left and the dashed red lines show the trajectory of the not or partially stripped H^- ions from the foil to the dump.

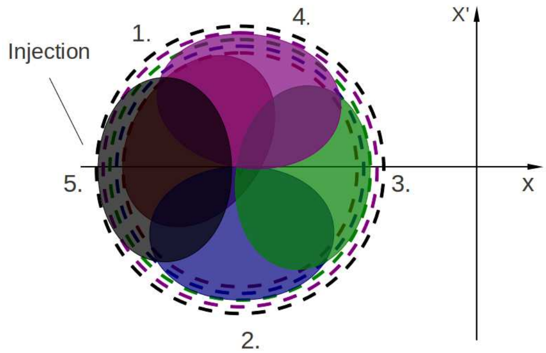

Figure 3.12: Movement of the bunches in horizontal phase space for the H^- injection. Using a H^- charge exchange injection it is possible to injected several times to the same phase space volume.

tatron function. If the perturbations caused by the edge focusing effects will not be compensated, the beam will be lost within the acceleration time completely. In order not to lower the performance of the Booster, the perturbations have to be compensated. To achieve the compensation, there are two possibilities, namely the active and the passive compensation scheme (cf. sections 3.3.3 and 3.3.4). The chicane fall time, after the injection is completed, is related to the chosen compensation scheme. The active compensation scheme needs additional quadrupole magnets and power supplies belonging to them. Depending on the angle between the beam and the pole faces during the fall of the chicane, the compensation magnet currents have to be adjusted in order to provide an effective compensation. To enable the power supplies to follow the required function for the current, the chicane can not be as fast as for the passive compensation scheme. For the active compensation scheme, the chicane will decay within 5 ms which is about 5000 turns. For the passive compensation scheme, the chicane will be roughly 10 times faster and decay within 500 turns after injection.

In addition to the injection chicane, the painting bump is required to implement the horizontal painting. The painting bump is, such as the chicane, a closed orbit bump around the injection area. The height of the painting bump at the beginning of the injection is, depending on the beam and other injection parameters, 35 mm and he is realised with 4 bumper magnets in the sections 1,2 and 16. Due to the larger distance of the magnets from the injection point, the deflections of the magnets can be smaller than for the BS magnets, thus, there are no significant perturbations due to edge focusing effects caused by the painting bump. Contrary to the chicane, the painting bump starts to decay already during the injection to control the filling of the horizontal phase ellipse. For a hight intensity beam with 1.6×10^{13} protons per ring, injected within 100 turns and with a maximum painting bump height of 25 mm, the painting bump decreases within 280 μs.

3.3.3 Active compensation

The active compensation is realised with additional quadrupole components at existing quadrupole magnets in the Booster lattice. Focusing errors, like the edge focusing effects at the BS magnets of the chicane, can be compensated efficiently at $\pm$ 90° ($n \in \mathbb{N}$) betatron phase advance from the perturbation. It is necessary to choose quadrupole magnets which fulfill these requirements for the vertical phase space, where lattice perturbations are strong, since the tune is close to a half-integer resonance. Appropriate locations for additional quadrupole components are the defocusing quadrupole magnets in the sections 3 and 14. Tab. 3.1 shows the beta function and the betatron phase advances at the chosen positions.

Table 3.1: Beta functions and betatron phase advance at the position of the active compensation. μ_x and μ_y show the betatron phase advance between the edge focusing at the BS magnets and the magnets where the compensation takes place.

Period	β_x [m]	β_y [m]	μ_x [2π]	μ_y [2π]
3	3.709	16.574	0.668	0.720
14	3.708	16.584	-0.668	-0.720

The beta function in the periods 3 and 14 are slightly different, in spite of the same positions in the respective periods, this is due to the fact that the painting bump is not completely symmetric around the injection point. As the compensation will be placed on defocusing magnets, the vertical beta functions are larger than the horizontal ones. This leads to effective compensation of the perturbations in vertical plane and to small perturbations in horizontal plane. The betatron phase advances at the compensation positions are:

$$0.720 \quad 2\pi \quad = \quad 1.44\,\pi \;\approx\; 1.5\,\pi \tag{3.3}$$

$$0.668 \quad 2\pi \quad = \quad 1.34\,\pi \;\approx\; 1.5\,\pi, \tag{3.4}$$

so that, the betatron phase advances at the compensation positions are almost at the required values of $\pm\, n \times 90°$ with $n \in \mathbb{N}$.

3.3.4 Passive compensation

For the passive compensation scheme, there are no additional focusing elements necessary. The perturbations will be mitigated by pole face rotations at the BS magnets of the chicane in order to have an, at least almost, perpendicular angle between the beam and the pole faces. Fig. 3.13 sketches the injection chicane with the passive compensation scheme.

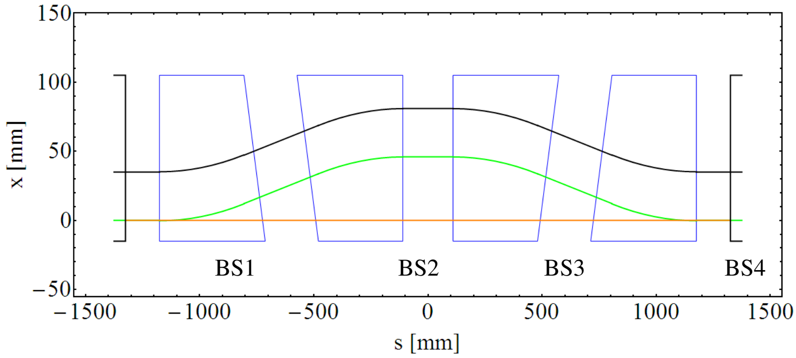

Figure 3.13: Passive compensation scheme with pole face rotations. The rotated pole faces avoid almost the edge focusing due to the fact, that the beam is nearly perpendicular to the magnets pole faces.

Due to the tight space available, there is not enough space left to realise the pole face rotations. Hence, the decision was made to implement the passive compensation by adding gradients to the magnetic field of the BS magnet, which is equivalent to pole face rotations.

Due to the fact that the chicane decreases after injection and the pole face rotations are fixed, it is not possible to mitigate the perturbations during injection and during the chicane fall. As a result, one has to find a compensation setting which gives the best results (cf. section 5.3.7 and 5.3.8).

3.4 PS Booster measurement line

The Booster measurement line, as used for the emittance measurements (cf. chapter 4 and section 2.5), is presented in Fig. 3.14.

The profile monitors to measure the transverse beam distributions are highlighted by red circles.

The dispersion and the Twiss functions at the positions of the profile monitors are known, which is necessary for the emittance measurements. The betatron phase advance between the monitors is $\mu = 60°$.

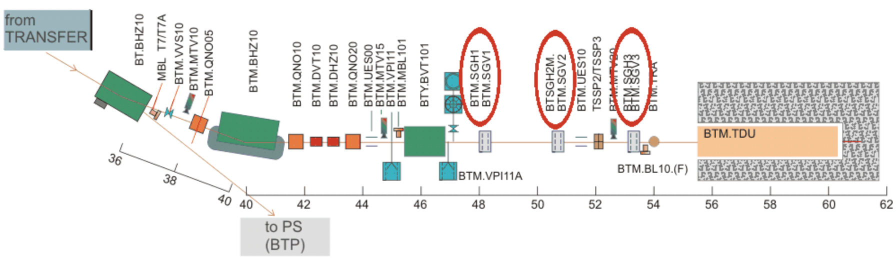

Figure 3.14: Elements of the Booster measurement line [14].

Chapter 4

Measurements

4.1 Beam properties

To run simulations of the injection and acceleration of a beam in the Booster for the results which are presented in this thesis, it was necessary to know the desired beam properties and, in particular, the emittances to adapt the simulation settings to this values. As the PS Booster has been running for many years using Linac2 as injector and as the beam parameters are the same for Linac2 and linac4 injection, it is possible to measure the standard emittances of different operational beams and apply them to simulations for Linac4. These measurements were carried out for a high intensity beam required for the CNGS (CERN Neutrinos to Gran Sasso) experiment and for the LHC25A (LHC nominal) beam. The emittances for the high intensity beam are required for the simulations presented in this thesis and the LHC nominal beam emittances for simulations which will be carried out in further studies.

To study the emittances, the beam investigated has to be sent to the measurement line of the Booster. Note, that just one out of the four Booster rings was used for the measurements to avoid effects by overlapping beams of the different rings. To have, at least, two sets of data, the measurements were carried out with beams from the Booster rings 3 and 4.

Before the emittance measurement can be started, the relative momentum spread of the beam, necessary for the calculation of the particles offset due to dispersion (cf. section 2.5), has to be evaluated. To this end, a tool called the Tomoscope has to be used to define the bucket. Fig. 4.1 shows several bunch shape measurements done at regular intervals (every 50^{th} revolution) during about one and a half synchrotron oscillation periods. These data serve to reconstruct the longitudinal phase space distribution depicted in Fig. 4.2 by tomographic reconstruction.

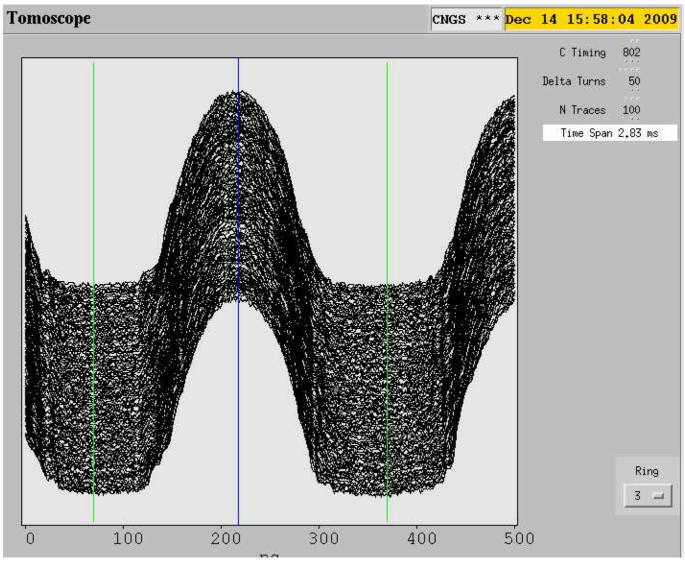

Figure 4.1: Tomoscope acquisition for a CNGS beam in Booster ring 3 a few milliseconds before ejection. The blue line marks the maximum and the two green lines the borders of the bunch.

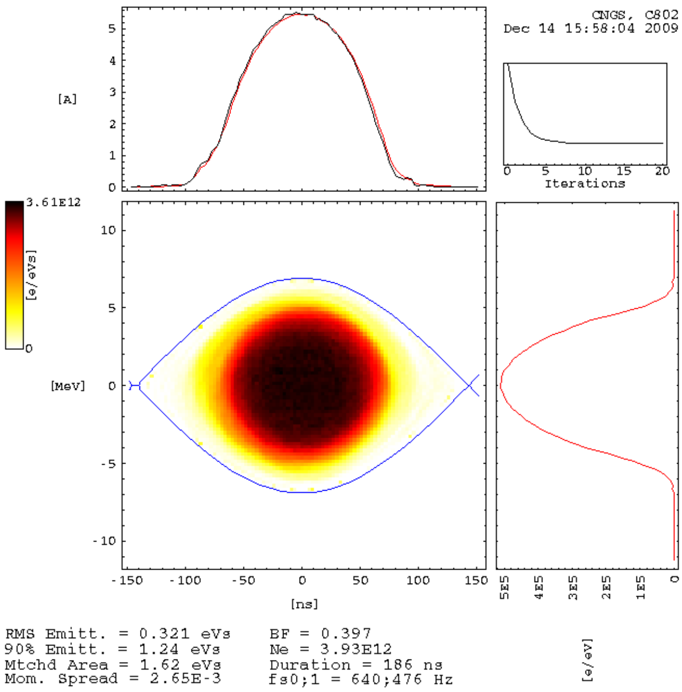

Figure 4.2: Tomoscope reconstruction of the longitudinal phase for a CNGS beam and of two bunches in ring 3. The particle distribution and the iteration function of the calculation are displayed by the plots at the top and right edge. As listed bottom left, the (two times 1 ns) calculated relative momentum spread is 2.65×10^{-3}.

After the momentum spread calculation is done, the measurements of the emittances can take place. But before the measurement, the horizontal or the vertical plane as well as the fitting model has to be chosen. Two different fitting models are available, Gaussian and Spline fit.
To avoid measurement errors due to corrupted wires of the profile monitors, it is strongly recommended to deactivate the concerned parts. Furthermore, the momentum spread achieved by the tomoscope reconstruction, has to be entered. Fig. 4.3 presents a screenshot of a typical emittance measurement at the Booster. The plots show the beam distributions at three positions in the measurement line (cf. section 2.5).

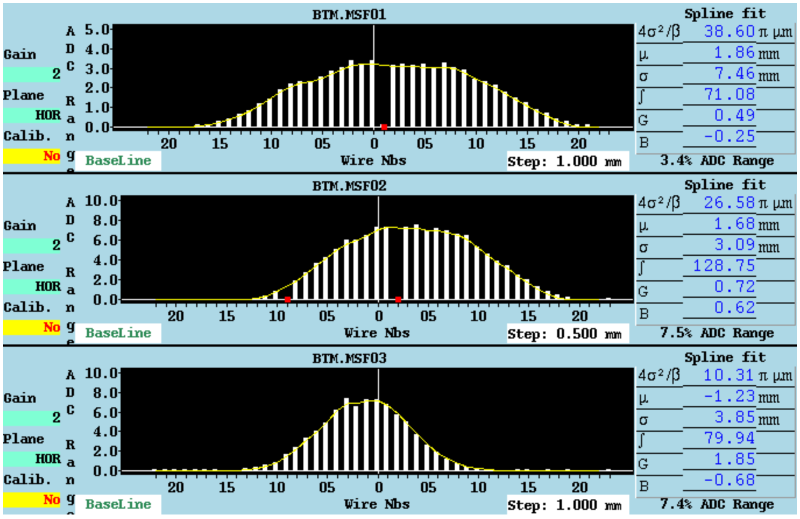

Figure 4.3: Horizontal emittance measurement for a high intensity CNGS beam accelerated in Booster ring 3. The spline fit was used for the calculations and the momentum spread, calculated before, was set to 2.65 10^{-3}. The calculated emittance is $\epsilon_x^{2\sigma}$ = 19.06 $\mu m\ rad$.

The emittances measured in the Booster are physical 2σ emittances for a 1.4 GeV proton beam. As the normalised 1σ emittances are required for the simulations, they have to be calculated using the following formula:

$$\epsilon^* \quad = \quad \frac{1}{4} \quad (\beta_{rel}\ \gamma_{rel})_{1.4\ GeV} \quad \epsilon^{2\sigma} \quad = \quad 0.571 \quad \epsilon^{2\sigma} \tag{4.1}$$

Measurements, like those presented in Fig. 4.1 – Fig. 4.3, were carried out for the CNGS and the LHC beam in horizontal and vertical plane. Furthermore, all emittances were calculated using the two different fitting methods and, as mentioned above, for the Booster rings 3 as well as for ring 4. All measured physical 2σ and all calculated normalised 1σ emittances for both beams and both fitting models are listed in Tab. 4.1.

The emittances in the simulations for a high intensity beam were set to ϵ_x^* = 12 μm rad and ϵ_y^* = 7 μm rad, according to the values achieved in the measurements and to theoretical values for the different beams.

4.2 PSB sensitivity to variations of compensation

An important question which had to be solved was to find out how sensitive the Booster reacts on imperfect compensations of the 2 Q_y = 9 resonance (cf. section 5.3.9). The data of these measurements will be compared with the simulations for the imperfect compensation of the edge focusing effects with the active compensation scheme in order to see, if the simulations deliver believable results.

Table 4.1: Measured emittances for a CNGS and an LHC beam.

	Gaussian fit		**Spline fit**	
CNGS beam, ring 3	$\epsilon^{2\sigma}$ [μm rad]	ϵ^{*} [μm rad]	$\epsilon^{2\sigma}$ [μm rad]	ϵ^{*} [μm rad]
horizontal plane	21.58	12.32	19.06	10.88
vertical plane	16.17	9.23	14.26	8.14
CNGS beam, ring 4	$\epsilon^{2\sigma}$ [μm rad]	ϵ^{*} [μm rad]	$\epsilon^{2\sigma}$ [μm rad]	ϵ^{*} [μm rad]
horizontal plane	24.66	14.07	20.29	11.58
vertical plane	16.92	9.66	14.09	8.04
LHC beam, ring 3	$\epsilon^{2\sigma}$ [μm rad]	ϵ^{*} [μm rad]	$\epsilon^{2\sigma}$ [μm rad]	ϵ^{*} [μm rad]
horizontal plane	5.55	3.17	6.20	3.54
vertical plane	5.01	2.86	4.80	2.74
LHC beam, ring 4	$\epsilon^{2\sigma}$ [μm rad]	ϵ^{*} [μm rad]	$\epsilon^{2\sigma}$ [μm rad]	ϵ^{*} [μm rad]
horizontal plane	5.19	2.96	6.13	3.50
vertical plane	5.10	2.91	5.42	3.09

The resonance compensation of the 2 Q_y = 9 resonance is realised with 2 quadrupole magnets at dedicated positions in the Booster like it will be the case for the active compensation of the edge focusing with Linac4.

To vary the compensation strength, the quadrupole currents were changed from an operation console in the CERN Control Centre. To see all effects caused by the modifications of the compensation, the beam intensity, the vertical emittances and the currents in the compensation magnets were measured and displayed.

The parameters which had to be modified for the measurements are labelled with BR2.QN0412L3 and BR2.QN0816L3. For the further description, these parameters will be called parameter 1 and parameter 2. Both power supplies are connected to two magnets in series with opposite polarities.

The two compensation currents were scanned to determine the limits of an efficient compensation. In the first measurements, only the strength of the parameter 2 was changed, at first to lower and then to higher currents in comparison to the initial values. The current was changed in steps of roughly 0.3 A until the beam was lost completely. For the second test, the current of parameter 1 was reduced by 1 A from -3 A to -4 A and the value of the parameter 2 was again changed to lower values in steps of 0.3 A until the beam was lost completely. This measurements were repeated for currents of -5 A, -6 A and -2 A for parameter 1. Fig. 4.4 shows an overview of the measurements mentioned above.

The injection intensity, represented by the blue line in the upper plot in Fig. 4.4, shows an almost constant value during the measurement. However, the values for the intensity at capturing, acceleration and ejection, shown in the same plot, are not constant during the measurement caused by modifications at the resonance compensation. The lower plot in Fig. 4.4 shows the desired and measured currents of the two compensation magnets and all steps of the measurement described above are visible. One can see, that the beam gets lost when the magnet currents cross the respective threshold values. In Tab. 4.2, all threshold values of the beam

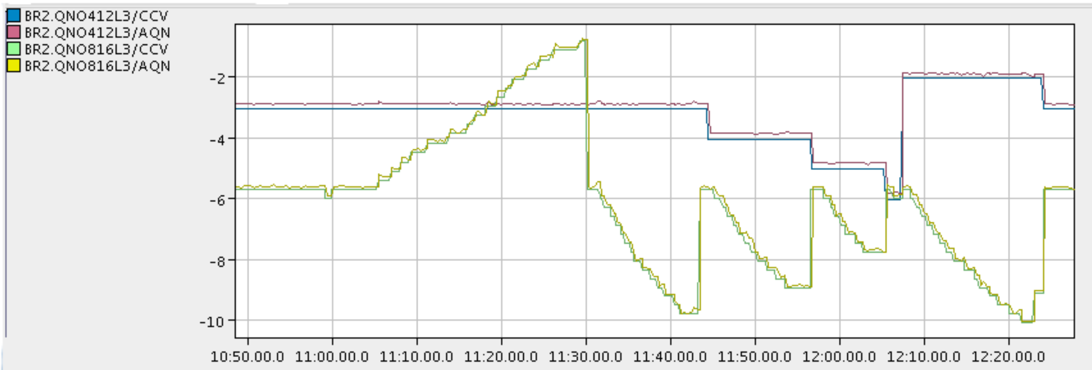

Figure 4.4: Overview of all measurements of the compensation sensitivity of the Booster. The upper graph shows the beam intensity and the lower one the modified currents in the compensation magnets. Both plots show all measurements mentioned. The blue line in the upper plot, labelled with suffix dcINJ, describes the beam intensity at injection, dcCAP (purple) after "capturing", dcACC (green) at acceleration and dcEJ (yellow) at ejection. The CCV (blue and green) values in the lower plot show the programmed magnet currents and the AQN (purple and yellow) values the measured ones.

losses are listed.
The Booster sensitivity on modifications of the resonance compensation is, by far, not as strong as initially expected. The measurements demonstrate that there is the possibility to vary the current of one magnet for more than -60 % and +80 %, respectively, without full beam losses. If the currents are modified in both magnets, there are still modifications in ranges of Amps feasible before the beam is lost completely. This shows the robustness of the Booster against compensation errors. But, there is a smaller impact on the Booster performance even before the beam is lost. As visible in the upper plot in Fig. 4.4, the beam intensity is already decreasing at the beginning of the modifications and the plot in Fig. 4.5 shows that the emittances are not at constant levels during the modifications.

Beside the threshold values for the beam losses, the emittances of the beam were also measured for many cases. It was expected to see a bigger emittance for imperfect compensations than for the perfect compensation case. The measured emittances were physical 2σ emittances in vertical plane calculated using the spline fitting and a relative momentum spread of 3×10^{-3}. As the normalised rms emittances were used for the simulations, they had to be calculated using Eq. 4.1.

Table 4.2: Threshold values for currents in the compensation magnets for beam loss.

$I_{Parameter1}$ [A]	Deviations	$I_{Parameter2}$ [A]	Deviations	Comments
-3.04	± 0 %	-5.69	± 0.0 %	Initial values
-2.04	+ 32.9 %	-8.60	- 51.1 %	Lower limit
-3.04	± 0 %	-1.10	+ 80.7 %	Upper limit
-3.04	± 0 %	-9.20	- 61.7 %	Lower limit
-4.03	- 32.6 %	-8.00	- 40.6 %	Lower limit
-5.03	- 65.5 %	-7.20	- 26.5 %	Lower limit
-6.02	- 98.0 %	/	- /	No stable beam

All measured values for different combinations of the magnet currents as well as the threshold values for the beam losses are listed in Tab. B.1. The emittance evolution of different settings are also plotted in Fig. 4.5.

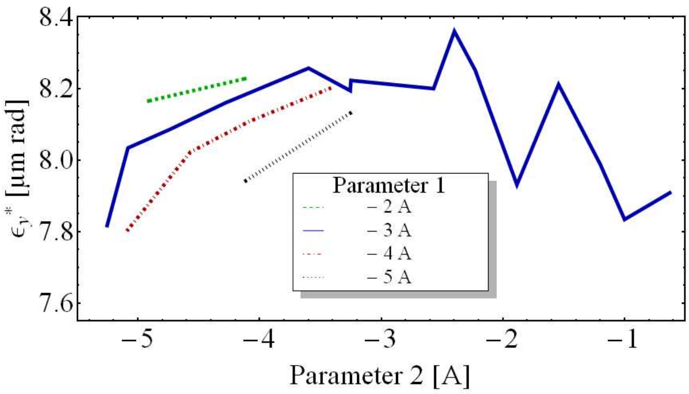

Figure 4.5: Measured emittances for different compensation adjustments. As shown in Fig. 4.4, the current of magnet Parameter 1 was set to fixed values, represented by the different plots, and the current for magnet Parameter 2 was varied to find the stable range. The initial value for Parameter 1 is -3.04 A and -5.69 A for magnet Parameter 2.

The emittances vary in a range of just ± 5 % of the initial value during the modifications of the quadrupole currents and it is visible that the emittances decrease for currents next to the threshold values. The most likely reason for the almost constant emittances is that the expected growth is prevented by particle losses. As shown in Fig. 4.4, this assumption is confirmed by the fact that the beam intensity becomes smaller during the modifications of the magnet currents before the beam gets lost completely.

4.3 Dynamic working point of the PS Booster

For the high intensity beams, the vertical injection tune of the Booster is $Q_y = 4.55$ above the half-integer resonance of $2Q_y = 9$. The reason for the high injection tune is the Laslett tune shift of roughly $\Delta Q = -0.5$. As the tune shift becomes smaller during acceleration, the vertical tune of the Booster can be moved to a position below $Q_y = 4.5$. This is also implemented to the Booster as existing at the moment which provides the possibility to measure the time evolution of the working point. Fig. 4.6 shows the time depending working point of an LHC nominal beam in the PS Booster. Also for this beam, the injection working point is higher than the working point at ejection but, the vertical injection tun is, unlike for the high intensity beam, below the half-integer resonance at 2 $Q_y = 9$.

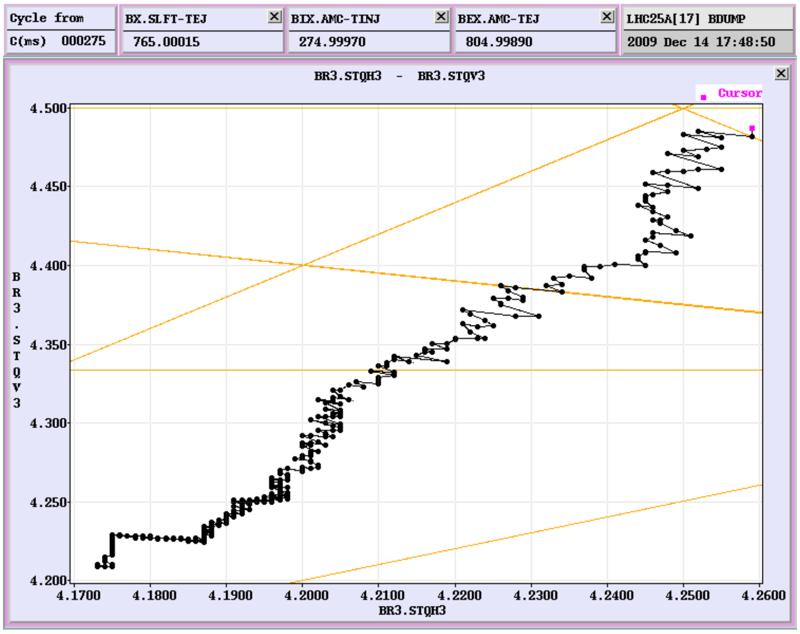

Figure 4.6: Time dependent working point in the Booster. The plot shows an injection working point at roughly (4.26/4.49) and a movement to the position (4.17/4.21) at ejection. This procedure is necessary to achive highest Booster performance.

Chapter 5

ORBIT Simulations

5.1 About ORBIT simulations

All simulations presented in this thesis were executed using the particle tracking code ORBIT [2] (Objective Ring Beam Injection and Tracking). Written for studying the Spallation Neutron Source SNS which is an accelerator- based neutron source in Oak Ridge, Tennessee, USA [15]. ORBIT was programmed to simulate H^- charge exchange injection via stripping foil from a linac to a storage ring and to simulate dynamics of beams with strong direct space charge forces. ORBIT is capable to use multiple processing to speed up the simulations and it is also possible to calculate the direct space charge effects between the protons.

For ORBIT runs with ”non-linear tracking”, a non documented feature, the lattice of the accelerator has to be described in teapot [16] format. Those are generated by first using MAD8 allowing matching to tune lattice parameters and, then, processing MAD8 generated output files with the help of python [17] scripts to generate the teapot style input files for ORBIT.

To launch an ORBIT simulation, a main file has to be called up inside the shell together with the information how many cores should be used. In the main file, all information about the simulation are given or they are implemented via other files called up by the main file. One of those files is the lattice file which contains all information about elements in the ring.

Two different bumps are needed for the injection from Linac4 to the Booster (cf. section 3.3.2). The painting bump is implemented to the simulation using the bump routing of ORBIT and the simulated magnets are defined as thin lenses. Unfortunately, this is not possible for the chicane, because it is necessary to simulate the edge focusing at the pole faces of the chicane magnets. It is therefore important to use bending magnets to simulate the chicane. The injection chicane and, as a result, focusing properties introduced as well as, in case of ”active compensation”, additional compensation quadrupole components, vary with time. Such time variations of the lattice properties were not foreseen by the ORBIT authors, but a procedure for simulations with magnet properties varying with time has been identified [18] and applied.
For this procedure, several scripts and programmes have to be used in the following order:

- Injection
  - Before the injection, the particle distribution has to be generated with a Mathematica [19] file which creates a list of particle coordinates in 6-dim phase space including the longitudinal painting. There is also the possibility to match the injected beam to desired Twiss parameters and the dispersion. The coordinates for each injection turn are saved to a separate file.

  - The main file which controls all further operational sequences defines all given parameters and loads a lattice file, using the initial parameters, where all lattice elements are defined. The main file implements also the files necessary for the acceleration of the particles.
  - The next step is the start of the injection by calling each single file with the initial particle distributions in the desired order, tracking the particles between two injections for one turn and dumping the coordinates of all particles in the ring after each turn.
  - The painting bump is implemented to the code as a time depending closed orbit bump which starts to decrease already during the injection takes place.

- Chicane fall
  - After the injection is finished, the chicane will start to decrease in order to move the beam off the foil as early as possible. To this end, all lattice elements will be deleted at each turn and reinstalled with modified values for the required magnets. All variations concerning the chicane are depending on the deflection in the chicane magnets and this value is defined in the main file as a variable depending on the number of turns accomplished. After the lattice is reinstalled, the acceleration files have to be installed again as well.
  - The particle coordinates, the coordinates of aperture hits and the information about the particles energy can be dumped to files at chosen numbers of turns and all files can be saved in specified folders.

- After chicane fall
  - When the chicane is completely decreased, it is not necessary anymore to reload the lattice including all elements at each turn. Due to this, the lattice will be installed one more time with values adjusted to a zero deflection in the chicane magnets and again the acceleration has to be installed separately.
  - The particle distribution as well as the other simulation parameters can still be dumped as before.

- End of simulation
  - The simulation can be ended using a quit command in the main file. Before quitting, all beam parameters can be dumped again.
  - To calculate the Twiss parameters, the emittances and the dispersion, which are used for all plots and further calculations in this thesis, out of the particle distribution, a Python [17] script is used.
  - Mathematica files are used for the evaluation of the data and to produce all plots.

Limited by computer power, it is not possible to track, for example, a high intensity beam with 1.6×10^{13} protons around the machine. To avoid this problems, a smaller number of macro particles representing the protons are injected and tracked around the machine. A reasonable number of macro particles with an appropriate simulation duration is 500 000 (cf. section 5.3.3). Attention has been paid to make sure that emittance blow-up and particle losses are not dominated by numerical artefacts due to a too small number of macro particles.

The typical number of cores used for simulations with half a million macro particles and all elements included is 24. A benchmarking comparing runs using different numbers of cores led to the conclusion that there is no big benefit with more cores due to the fact that then the communication between the cores will become the main limitation.

As there will be different beams send through the PSB, it is important to allude that all kind of beams can be injected and accelerated with the combination of Linac4 and the PS Booster. The simulations which are presented in this thesis are for a high intensity beam with 1.6×10^{13} protons per ring and normalised emittances of ϵ_x^* = 12 $\mu m\ rad$ and ϵ_y^* = 7 $\mu m\ rad$. With the high intensity beam, there are the highest direct space charge effects expected and the beam size is bigger than for other beams. Together with high brightness LHC beam, these beams are considered the most critical ones, where an injection working point above the vertical half-integer resonance is attractive.

5.2 Particle distribution for injection

The initial particle distributions are generated using a Wolfram Mathematica notebook to model the injection with transversal and longitudinal painting. For each injected turn, one file containing the initial coordinates for all macro particles is generated. It is possible to choose the number of macro particles, the energy spread and shift as well as it is possible to match or mismatch the injected beam to the Twiss parameters and to the dispersion of the machine at injection point. The possibility to modify the energy shift of the particles is used to implement the longitudinal painting to the simulations. The notebook stores automatically all necessary files for the injection to the ORBIT simulations.

5.3 Simulations

The main aim of the simulations is to investigate, if it is feasible to use the higher vertical injection tune above the half-integer resonance at 2 Q_y = 9 with Linac4 applying either the active or the passive compensation scheme. Furthermore, the aim is to assess and compare the effects of the two compensation schemes proposed to deal with lattice perturbations. Results will be used do decide on the compensation scheme implemented. Many simulations were carried out, first, to assure that the programme is running properly and second, to get the data which allow to make the decision between the two schemes. The most important simulations will be presented in this section.

5.3.1 Implementation of the acceleration

The first simulation with ORBIT was related to the implementation of the acceleration to the code. The intension was to verify that the acceleration is correctly implemented. To this end, a simulation was carried out using a fixed lattice i.e. with a chicane which is fully established during the entire simulation. The fixed lattice was chosen to avoid additional effects caused by the decreasing chicane. The computation of the direct space charge effects were also switched off to prevent blow up due to collective effects. Also the stripping foil was not implemented, because the scattering would give an increase of the emittance. All settings of the simulation are listed in Tab. C.1.

The physical emittances for both planes are shown in Fig. 5.1. The dots denote physical rms emittances estimated from macro particle distributions dumped on files during simulation.

The two dots dropping out the line at 100 and 1400 turns in both plots are in all probably due to corrupted files containing macro particle distributions.

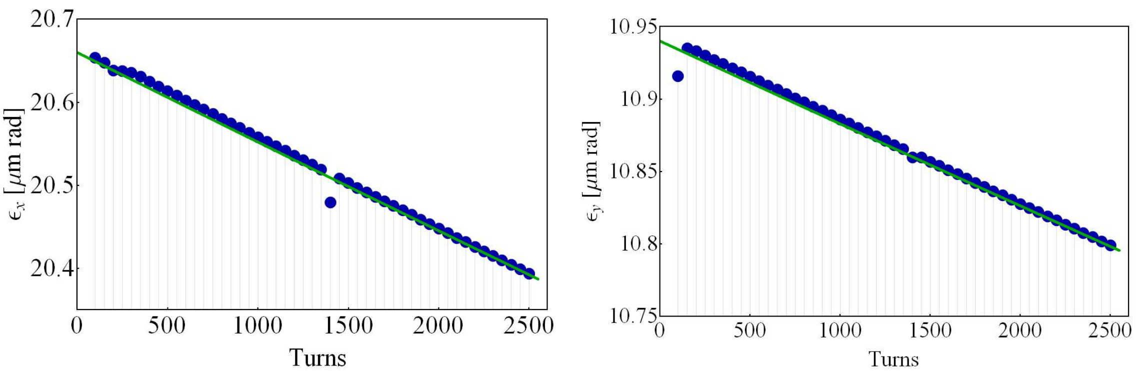

Figure 5.1: Physical emittance during acceleration. The horizontal plane is shown on the left and the vertical plane on the right hand side.

The injection during the first 100 turns is not shown, because the physical emittance is growing during the injection due to the transverse painting. The injection turns would not provide more information about the implementation of the acceleration. It is clearly visible that the physical emittance[1] shrinks due to the acceleration process after completion of the injection process. The green line, which fits well the physical emittance estimated from macro particle distributions, indicates the expected slope of the emittance evolution.

The effect of the acceleration simulation on the particles is as expected and, as a result, the acceleration is implemented to the code correctly.

5.3.2 Implementation of the apertures

Direct space charge effects between the particles are calculated in cells and the size of the cells is given by the distance between the particles which are the farthest apart divided by the number of bins chosen in the main file. If there are particles too far away from the design orbit, the cells are too big to get reasonable results from the space charge calculations. For this reason and to estimate particle losses, it is essential for the simulations to remove particles with too large amplitudes. To this end, apertures are defined. In this section, the implementation and a test of the implemented apertures will be presented.

The design of the apertures is based on the aperture design in the PS Booster as existing at the moment. Only the size of the so called beam scope window is different considering the higher energy of the beam injected with Linac4. All apertures are implemented to the simulations using the ORBIT aperture routine. If a particle hits an aperture, all coordinates from the 6-dim phase space will be dumped to a file and the particle will be taken out of the simulation. In the aperture files, which contains the coordinates of the lost particles, there is also the position and the node of the aperture hit, as well as the turn number. Figure 5.2 shows the positions of the apertures in a regular Booster period.

The standard apertures have a race track shape and they are located in each Booster period at the positions after the first and before the second bending magnet. The beam scope window is just at one dedicated place in period 8, drift L2. It is smaller than the usual apertures to catch most of the particles at this place in order to avoid activated material all around the machine.

[1]Note that the physical emittance is plotted to illustrate the shrinking physical emittance during acceleration. However, in all other emittance plots, normalised emittances will be shown instead.

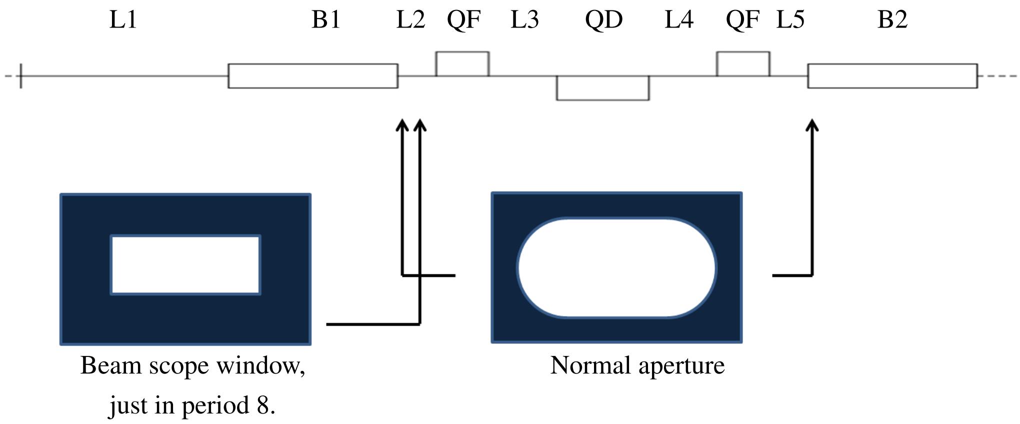

Figure 5.2: Positions of the apertures in a regular period of the PS Booster with drift sections (L), bending (B) and quadrupole (Q) magnets.

The apertures in the Booster periods 3, 14 and 15 are slightly different from the standard apertures. All apertures used in the simulations are defined in Fig. 5.3 and Tab. 5.1.

The apertures with Δx = 61.0 mm and Δy = 29.5 mm are the standard ones. The apertures of the injection area in period 1 and the ejection section in periods 14 and 15 are enlarged to create space for the injected and ejected beams.

An additional Aperture was implemented at the position of the injection septum which is not represented in Fig. 5.2. Due to the position of this aperture between the chicane magnets BS1 and BS2, in the range of the chicane, this aperture has to be implemented differently. The positions of the apertures are given in a coordinate system attached to the design orbit and the chicane magnets are programmed as bending magnets of the lattice. As a result, the design orbit will be change during the chicane fall. If the septum aperture would be implemented at fixed coordinates, the aperture would perform the same movement as the beam during the chicane fall and there would not be any relative movement between them. For this reason, the septum aperture is implemented to the simulation with a time depending x-coordinate which is correlated to the deflection in the BS magnets.

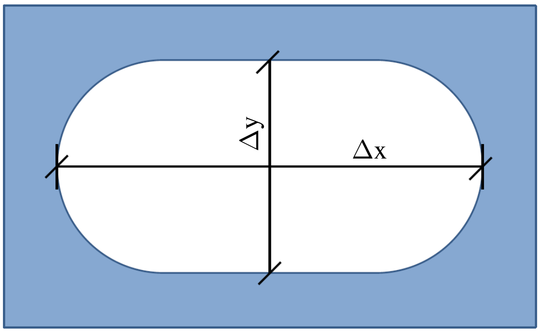

Figure 5.3: Size of the apertures

Table 5.1: Sizes of apertures implemented at different locations of the lattice.

Aperture dimensions in period 1

Position B1	Δx = 64.0 mm	Δy = 29.5 mm
Position B2	Δx = 61.0 mm	Δy = 29.5 mm

Aperture dimensions in period 2-13 and 16

Position B1	Δx = 61.0 mm	Δy = 29.5 mm
Position B2	Δx = 61.0 mm	Δy = 29.5 mm

Aperture dimensions in period 14

Position B1	Δx = 61.0 mm	Δy = 29.5 mm
Position B2	Δx = 68.5 mm	Δy = 29.5 mm

Aperture dimensions in period 15

Position B1	Δx = 64.0 mm	Δy = 29.5 mm
Position B2	Δx = 61.0 mm	Δy = 29.5 mm

The size of the beam scope window in the simulations is smaller than in the existing PS Booster, because the beam size will change due to the higher injection energy. With Linac4, the Booster is expected to generate beams with the same (normalised) emittances than now. To remove particles with large betatron amplitudes already at low energy with Linac4, the Beam scope window should be reduced accordingly. The size for the 50 MeV injection energy is Δx = 50 mm and Δy = 28.6 mm. To calculate the new dimensions, consider:

$$\epsilon_{160\text{ MeV}} = \frac{(\beta_{rel}\gamma_{rel})_{50\text{ MeV}}}{(\beta_{rel}\gamma_{rel})_{160\text{ MeV}}}\,\epsilon_{50\text{ MeV}} \approx 0.544\,\epsilon_{50\text{ MeV}} \tag{5.1}$$

$$\text{with} \qquad x^{max} \propto \sqrt{\epsilon} \qquad x^{max}_{160\text{ MeV}} = \sqrt{0.544}\;\; x^{max}_{50\text{ MeV}} \tag{5.2}$$

To take orbit variations into account, 5 mm have to be subtracted from the width and height before the calculation of the new dimensions takes place.

$$x^{max}_{160\text{ MeV}} = (50.0\,mm - 5\,mm)\,\sqrt{0.544}\, + 5\,mm \approx 38.18\,mm \tag{5.3}$$

$$x^{max}_{160\text{ MeV}} = (28.6\,mm - 5\,mm)\,\sqrt{0.544}\, + 5\,mm \approx 22.40\,mm \tag{5.4}$$

Due to this, the size of the beam scope window in the simulations for 160 MeV protons is Δx = 38.18 mm and Δy = 22.40 mm.

To control the implementation of the apertures, a test simulation with one standard aperture and a rectangular shaped particle distribution was carried out. The test beam was created with an equal distribution of 200 000 macro particles over a 200 mm times 120 mm rectangle with zero deflection in x and y plane. A scatter plot with coordinates of macro particles which hit the aperture, is shown in Fig. 5.4.

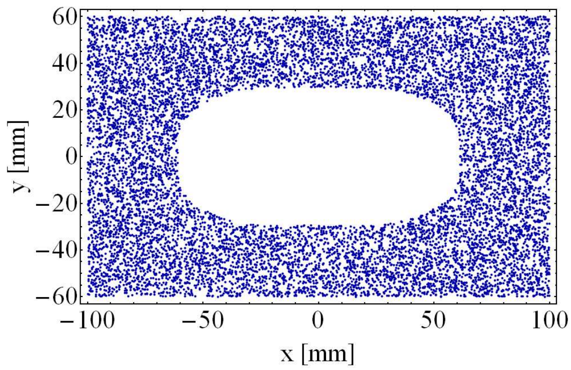

Figure 5.4: Aperture hits with a rectangular particle distribution and a standard Booster aperture.

The distribution of the particle hits on the aperture looks like expected. Hence, the assumption was made that the routine to simulate apertures and the routine to dump the aperture hit coordinates work properly.

5.3.3 Benchmarking on the number of macro particles

The number of macro particles required for simulations and more general appropriate simulation parameters are a delicate topic. To get an idea about the effects of the number of macro particles, similar simulations were run varying the number of macro particles and keeping all other parameters fixed. The used numbers of macro particles were 250 000, 500 000 and 750 000. All settings are listed in Tab. C.2.

In Fig 5.5, the emittances calculated with the distribution of the different numbers of macro particle are plotted as function of time.

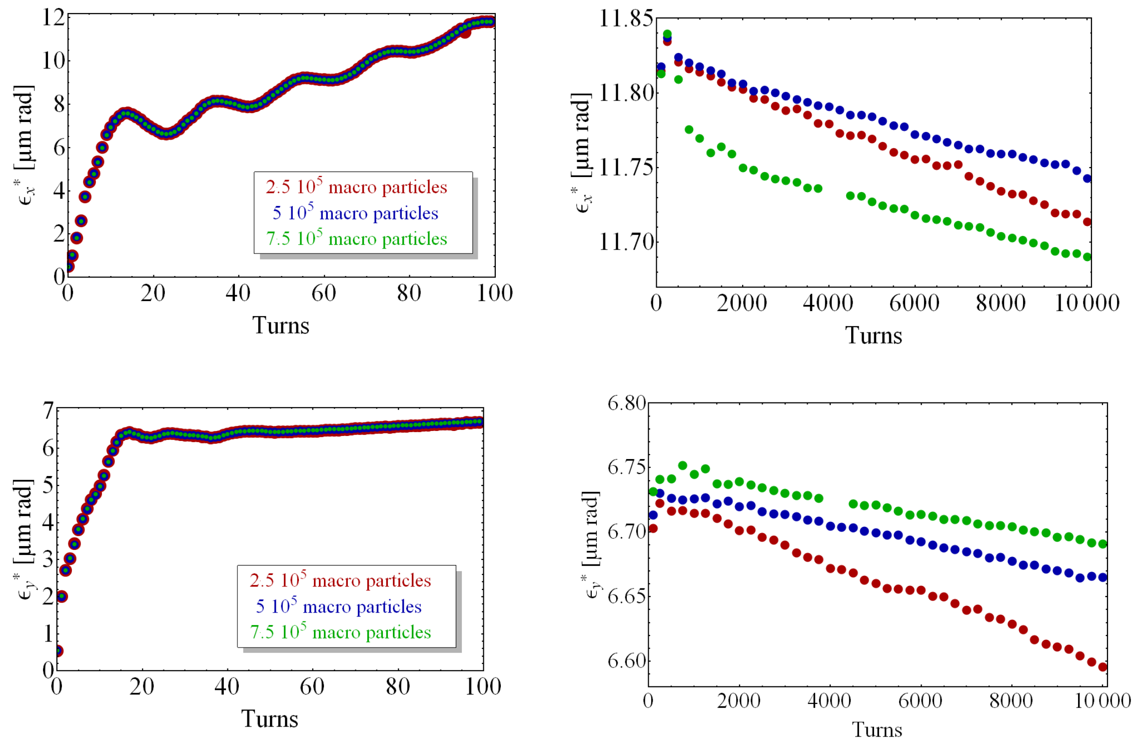

Figure 5.5: Normalised emittances for different numbers of macro particles. The first line represents the emittances in horizontal plane, the second line the emittances in vertical plane. Emittance evolutions during the injection turns are shown on the left and the ones for the rest of the simulation on the right hand side.

The emittance evolution is very similar for all three cases during injection, but after injection, small differences are visible in both planes. The oscillation of the emittance evolution in the horizontal plane is caused by dispersion of the injected beam and by the longitudinal painting.

More information to compare the simulations provide the numbers of lost particles. The plots in Fig. 5.6 show loss rates as function of time. The accumulated losses for all three cases are shown in Fig. 5.7.

The more macro particles in the simulation, the smaller are the relative losses. The difference between 250 000 and 500 000 macro particles is bigger than the difference between 500 000 and 750 000 macro particles. Particularly the behaviour of the simulation for 250 000 macro particles towards 10 000 turns is different from the behaviour of the two other simulations. Both, emittance evolutions and loss rates during the first part of the simulation, where lattice perturbations are expected to cause emittance blow up, are similar at least for 500 000 and 750 000 macro particles. Thus, one concludes that the results for 500 000 macro particle are not dominated by numerical artefacts caused by a too small number of macro particles.

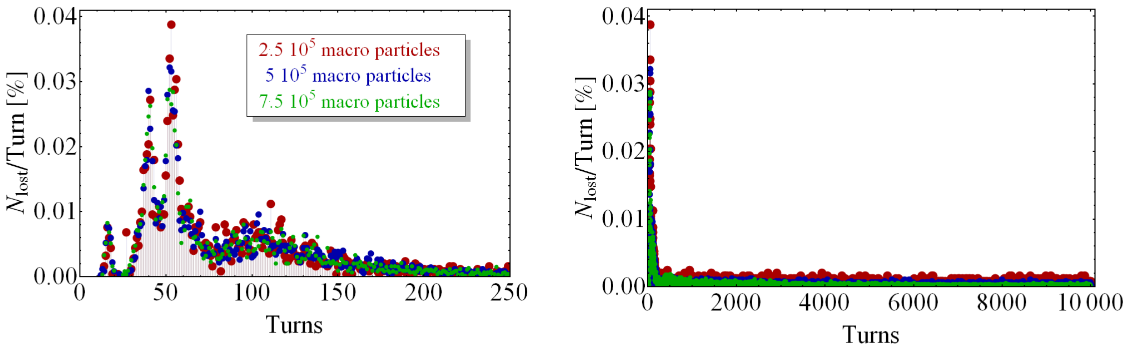

Figure 5.6: Relative losses per turn for different numbers of macro particles. The plot on the left shows the data for the injection and up to 250 turns and the plot on the right shows the data up to 10 000 turns.

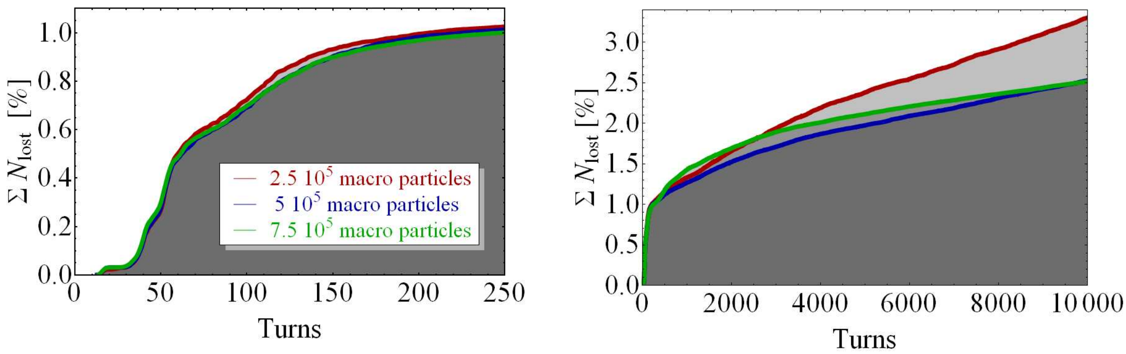

Figure 5.7: Accumulated losses for different numbers of macro particles. The plot on the left hand side shows the injection and the first turns up to 250 and the plot on the right hand side shows the data up to 10 000 turns

After this benchmarking the decision was made to use 500 000 macro particles for all further simulations.

5.3.4 Different scattering models for the injection foil

The injection foil is a necessary element for the H^- injection to strip the electrons from the H^- ions. Unfortunately, the foil will also cause scattering which leads to emittance growth and therefore to beam quality degradation. As a result, it is important to get the beam off the foil as fast as possible. However, there will be scattering at least during the demotion of injection and it is unavoidable to implement the scattering to the simulations to take these effects into account.

ORBIT provides two different scattering models for the foil named "model 1" and "model 2". To decide which model will be used, two simulations were carried out to see how the different scattering models effect on the beam.

For these investigations, a particle distribution with 10 000 macro particles was created, all at position $x = 0$, $y = 0$ and with zero deflection in both planes. This distribution was "injected", send through the foil and directly behind the foil, the particle coordinates in 6-dim phase space were dumped and the data evaluated. Scattering due to a thin carbon foil generates multiple Coulomb scattering distributions (cf. section 2.3) with strongly populated tails and a narrow central peak. To see the scattering effects of ORBIT "model 1", "model 2" and of the expected distribution for multiple Coulomb scattering, the distributions for x' and y' coordinates are shown in Fig. 5.8.

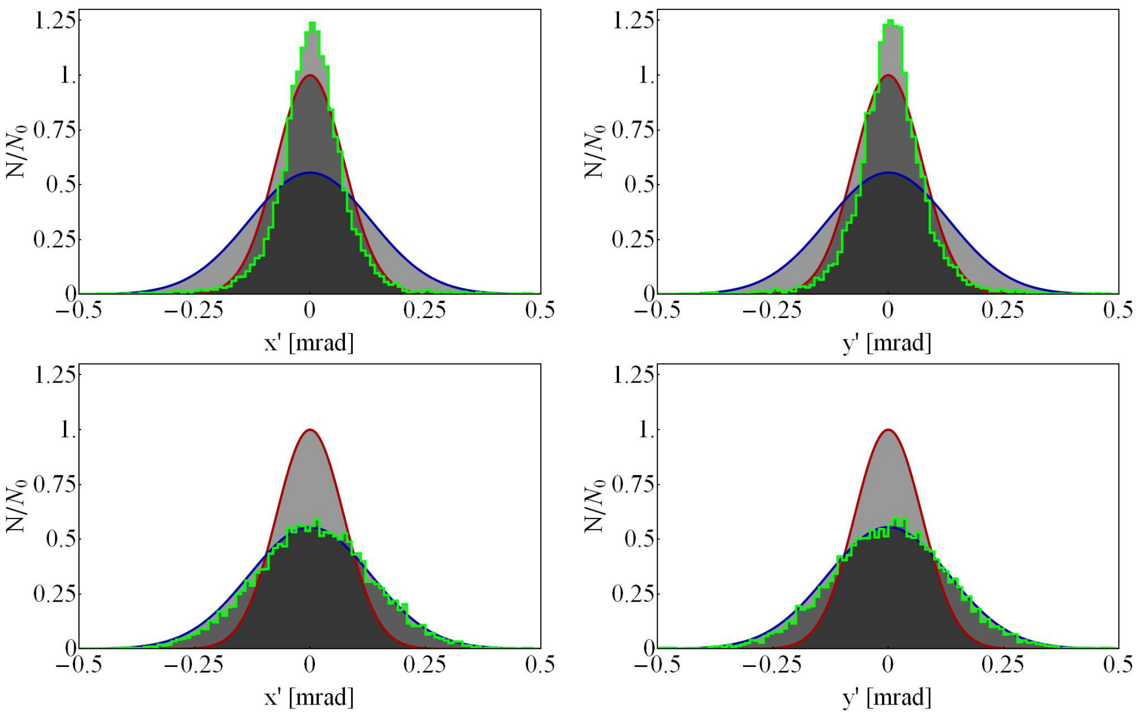

Figure 5.8: Comparison of the particle distributions after scattering simulations with different scattering models. The plots in the first line are for the ORBIT scattering "model 1" and the plots in the second line for ORBIT "model 2". The green lines represent the distributions after scattering simulations using the models in ORBIT. The red and the blue lines represent the expected distributions for multiple Coulomb scattering as described in section 2.3. The red line shows a distribution with width Θ_1 and the blue line with width Θ_2.

The scattering distribution expected for a thin foil, as described in section 2.3 using the width Θ_1 calculated with a formula for multiple Coulomb scattering, is represented by the red line in Fig. 5.8. The blue line represents a Gaussian scattering distribution with width Θ_2, calculated without the logarithmic term of the formula mentioned before. The used formula is valid for foil thicknesses of 160 μm < d < 16 m. The foil thickness used for the simulations is:

$$d \;=\; 300\frac{\mu g}{cm^2} \;=\; 1.33\,\mu m \tag{5.5}$$

and below the minimum level of the formula's domain of definition. Compared to a foil with thickness of 160 μm, one expects for a thinner foil a scattering distribution with a higher, thinner peak. This is exactly shown by the ORBIT scattering "model 1". The distribution of ORBIT "model 2" shows a smaller and wider peak and fits well to the distribution calculated with Θ_2.

Tab. 5.2 shows the theoretical values Θ_1 and Θ_2 as well as the values calculated using the macro particle distribution after scattering simulated with the ORBIT "model 1" respectively "model 2".

Table 5.2: Theoretical and simulated widths of the particle distributions after scattering at the foil.

$\Theta_1 = 0.0734$	$\Theta_{model1,x'} = 0.0953$	$\Theta_{model1,y'} = 0.0876$
$\Theta_2 = 0.1321$	$\Theta_{model2,x'} = 0.1587$	$\Theta_{model2,y'} = 0.1387$

Interesting is also that the energy losses caused by the scattering at the foil is modelled in two different ways. In ORBIT's scattering "model 1", there is no energy loss at all and in the second model, all particles loose the same amount of energy. The lost energy in "model 2" per 160 MeV proton and per foil pass is -1.4×10^{-3} MeV.

Taking into account the facts from this simulations, the decision was made to use the scattering ”model 1”. Crucial was that the scattering effect on the distribution of scattering ”model 1” is more like the reference model using Θ_1 than scattering ”model 2”. The fact, that there is no energy loss implemented to the first model is expected to be negligible, because the typical energy loss is very small compared to the bucket hight and the transverse blow-up due to energy loss, as well as the fact that the foil is in a dispersive section, is small compared to the emittance to be provided by the Booster.

5.3.5 Impact of the foil implementation method

To describe the dynamic chicane and painting bump in ORBIT, the lattice has to be erased and re-implemented with modified parameters for the magnets concerned at each turn during the chicane fall. To assure that this treatment is feasible also for the injection foil, two simulations were carried out using the same setting but in the first simulation, the foil was implemented just once at the beginning and for the second simulation, the foil was erased and re-implemented at each turn. In order to get a stronger influence of the foil on the beam, the simulation was carried out in such way that the particles passed the foil 5000 times instead of roughly 100-200 turns as usual for the injection of a high intensity beam. In contrary to the expectations, comparing the simulations one could see that there are differences shown for the emittance evolutions between the two implementation methods (cf. chapter A). The reasons for these deviations are not resolved yet. Due to the fact that the deviations are small, especially during the first 100 turns which are of interest in the simulations, one concludes that the implementation method can be applied anyway.

5.3.6 Quadrupole resonances

To investigate if there are quadrupole resonances, the beam envelopes in both planes have to be studied. It is well known that the envelope of the beam can be calculated by:

$$\sigma = \sqrt{\epsilon\beta} \tag{5.6}$$

The parameters ϵ and β used for this investigations are calculated from the macro particle distribution dumped to external files during the simulation. Two different simulations were carried out using the passive compensation scheme, the first after the injection (100-220 turns) and the second after the chicane fall (600-720 turns). The plots in Fig. 5.9 show the evolution of σ^2 for both transversal planes and for both cases.
The frequencies of the quadrupole oscillations simulated were calculated using the FFT method and the results are presented in Tab. 5.3 and Tab. 5.4.

Table 5.3: Frequencies after injection

Plane	horizontal	vertical
Frequency	0.373 1/Turn	0.707 1/Turn

The upper plots in Fig.5.9, showing the data for the simulation after injection, one can see a coupling between the horizontal and vertical plane described by an increasing σ_x^2 and a decreasing σ_y^2 during the simulation. As this behaviour is not shown in the simulation after the chicane fall, one concludes that the

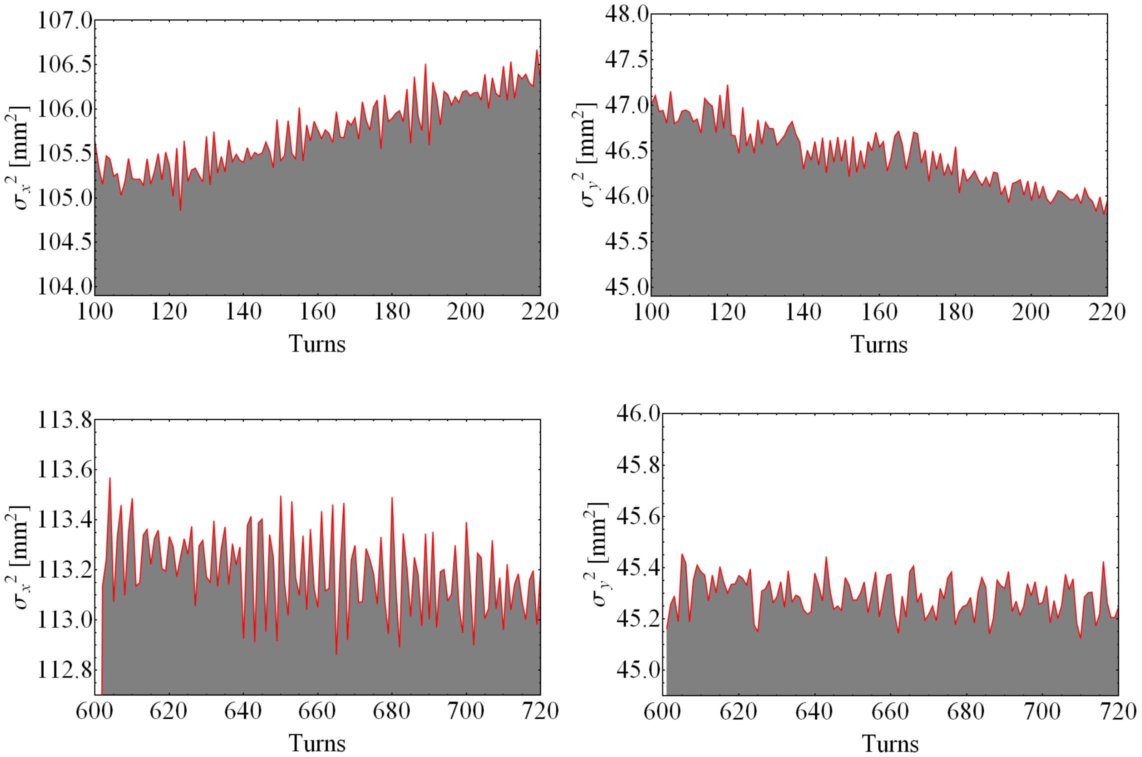

Figure 5.9: σ oscillations. The first line shows the oscillations after the injection and the second line after the chicane fall.

Table 5.4: Frequencies after chicane fall

Plane	horizontal	vertical
Frequency	0.361 1/Turn	0.601 1/Turn

coupling is probably caused by the decreasing chicane, the painting bump or the injection.

Quadrupole resonances in both planes are related to the incoherent space charge tune shift and can be calculated with the following formulas [20]:

$$Q_{2,x} = 2Q_{0,x} - \left(1.5 - 0.5\frac{a_x}{a_x + a_y}\right)|\Delta Q_{inc,x}| \tag{5.7}$$

$$Q_{2,y} = 2Q_{0,y} - \left(1.5 - 0.5\frac{a_y}{a_x + a_y}\right)|\Delta Q_{inc,y}| \tag{5.8}$$

With the frequency of the quadrupole oscillations $Q_{2,x}$ and $Q_{2,y}$, the frequency of the betatron oscillations $Q_{0,x}$ and $Q_{0,y}$, the incoherent tune shifts in both planes $\Delta Q_{inc,x}$ and $\Delta Q_{inc,y}$ and the horizontal and vertical beam dimensions a_x and a_y. This formulas were used to calculate the expected tune shift for the given quadrupole resonances to compare them with the tune shifts given in the simulations. The expected values are (cf. Fig. 5.18):

$$\Delta Q_{inc,x} \approx -0.35 \qquad \text{and} \qquad \Delta Q_{inc,y} \approx -0.5. \tag{5.9}$$

The absolute values for the tune shift calculated by the simulated quadrupole resonances are listed in Tab. 5.5.

Table 5.5: Calculated absolute values for the incoherent tune shift.

	Horizontal plane	Vertical plane
After injection	0.31	0.62
After chicane fall	0.30	0.47

The values for the incoherent tune shift calculated by the simulated data fits well with the expected tune shifts for the Booster which explains the frequencies of the quadrupole resonances.

5.3.7 Passive compensation with different pole face rotations

To investigate the impact of the pole face rotations used for the passive compensation on the performance and to find the best setting, several simulations were carried out using different angles of 0, 20, 40, 50, 60, 64, 66 and 70 mrad. The maximum deflection of the beam in the chicane magnets was 66 mrad.

All simulations were run with the same set of macro particles and with the same offset between injected and circulating beam in both planes. Due to varying focusing effects caused by different pole face rotations, the fall time of the painting bump had to be modified to adjust the horizontal emittance to the required values. Unfortunately, there is no possibility to do such a compensation for the vertical emittance which leads to different values. Smaller emittances will lead to less losses during injection and therefore it is necessary to take this effect into account interpreting the data. Table 5.6 shows the normalised emittances after injection for all cases. The desired normalised emittances are ϵ_x^* = 12 $\mu m\ rad$ and ϵ_y^* = 7 $\mu m\ rad$.

Table 5.6: Normalised emittances after injection for all simulations with different pole face rotations.

	0 mrad	20 mrad	40 mrad	50 mrad	60 mrad	64 mrad	66 mrad	70 mrad
ϵ_x^* μm rad	12.04	12.09	12.18	12.20	11.76	12.15	11.93	11.94
ϵ_y^* μm rad	6.25	6.54	6.86	6.98	6.97	7.05	7.00	6.39

The vertical emittances for 0, 20 and 70 mrad are much smaller than required. As mentioned above, this will lead to smaller vertical beam sizes (the vertical beta functions are almost the same at the end of injection) and, due to this, to smaller losses during injection. However, these simulations will be compared with the other simulations as well to see what are the effects caused by those angles.

As the fast chicane used for the passive compensation decays between turn 100 and 600, it was sufficient to run this simulations up to 750 turns, because all effects caused by the chicane can be investigated within this range. Fig. 5.10 shows the horizontal emittances for all pole face rotations.
In the horizontal plane, all emittances are similar at the end of injection due to accordingly modified painting schemes. The different evolutions of these values are caused by different beta functions depending on the pole face rotations. The smaller the angle of the pole faces, the bigger is the horizontal beta function and the smaller is the emittance.

In Fig. 5.11, the emittances in the vertical plane are presented. It was not possible to obtain the same values for the vertical emittances at the end of injection for all cases, because there is no vertical painting bump to keep the emittances at the same values in spite of the different perturbations. The evolution of the vertical emittance during injection is again, like in the horizontal plane, due to the evolution of the beta functions. In vertical plane, the smallest angle of the pole face rotations leads to the smallest beta function and to the biggest emittance. The data for the horizontal and the vertical beta functions between injection and up to

750 turns are presented on the right hand side in Fig. 5.12.

The emittance evolution in the vertical plane after injection is almost the same for the angles between 60-70 mrad. For the smaller angles below 60 mrad, the emittances are shrinking due to more particle losses caused by the not compensated part of the perturbations.

Fig. 5.13 shows the loss rates per turn for all different pole face rotations. There are losses during injection caused by the used linear decreasing painting bump. The losses for the simulations with angels between 60 and 70 mrad are much smaller than the loss rates for pole face rotations below 60 mrad. Due to this, the best setting has to be found within this range. More information about the losses are provided in the plots for the accumulated losses shown in Fig. 5.14. The one on the left shows clearly that out of the set of angles up to 50 mrad, the 50 mrad pole face rotation leads to the smallest number of losses. In the plots on the right hand side, the number of lost particles for a pole face rotation of 70 mrad is the smallest. This is a surprisingly result, because a 70 mrad angle is already over compensation for a maximum deflection of 66 mrad. Probably this result is caused by another effect which was not taken into account. One possibility is that the normalised emittance for the 70 mrad pole face rotation was smaller than for other angles. This leads to a smaller beam size and possibly to less losses. Also the the emittances for the 66 mrad case, which shows also a relative low loss rate, was smaller then the nominal value. However, the emittance for the 64 mrad case was bigger than the desired values in both planes and the accumulated losses are in the same range as for the 66 mrad pole face rotation. This fact leaded to the decision to use the 64 mrad pole face rotation for further simulations.

Tab. 5.7 shows the particle losses in percentage of the beam for simulations with different pole face rotations. The first line presents the numbers of losses for all turns up to 750, the second line the losses during injection and the third line all losses between the end of injection and 750 turns.

Table 5.7: The loss rate for different pole face rotations in percentage of the beam for the injection, for the time after the injection and for the whole time of the simulation.

	0 mrad	20 mrad	40 mrad	50 mrad	60 mrad	64 mrad	66 mrad	70 mrad
All	25.02 %	16.30 %	9.26 %	6.59 %	4.16 %	4.20 %	4.00 %	3.43 %
Injection	17.64 %	12.15 %	6.92 %	4.44 %	2.04 %	1.57 %	1.25 %	0.76 %
After Injection	7.39 %	4.16 %	2.34 %	2.15 %	2.12 %	2.63 %	2.75 %	2.67 %

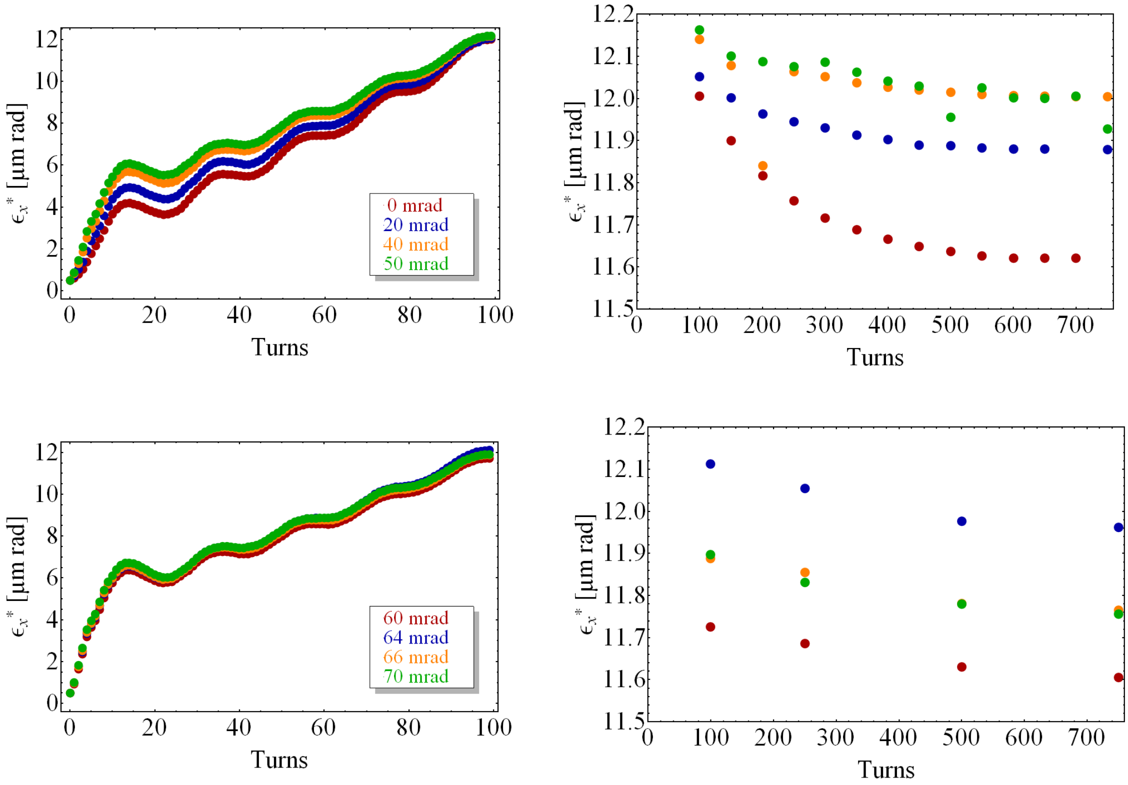

Figure 5.10: Horizontal emittances for different pole face rotations. All injection turns are presented on the left hand side and the turns after injection on the right.

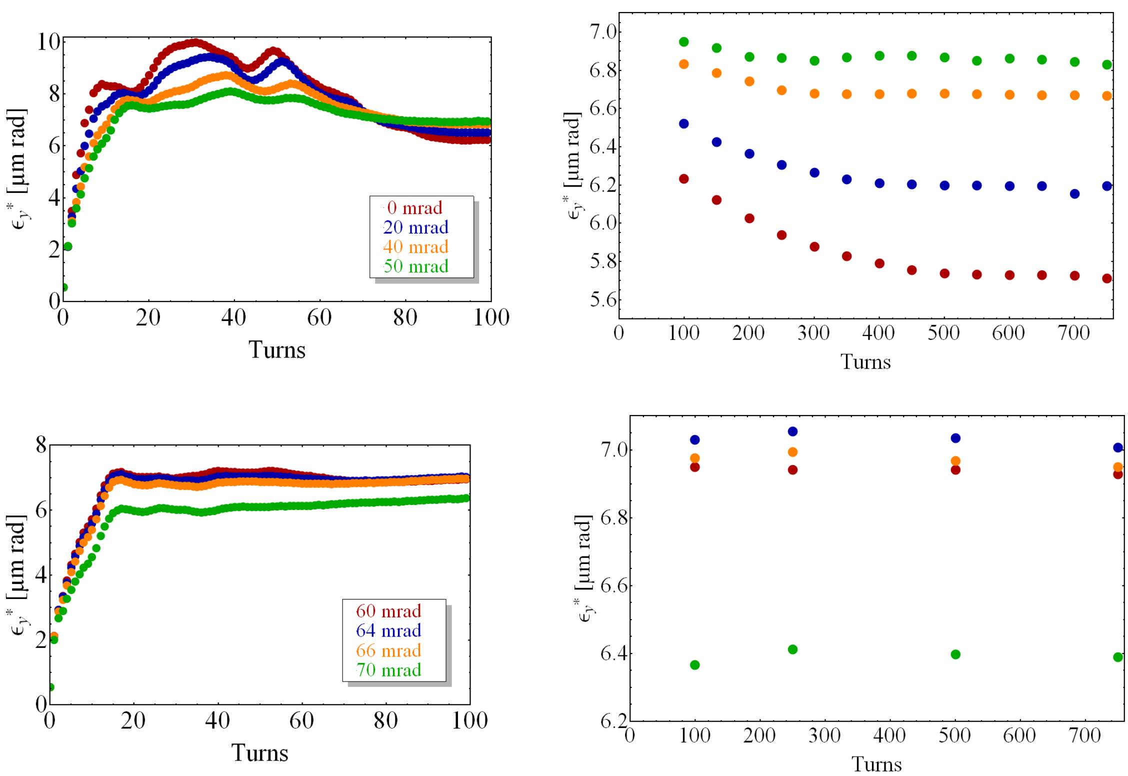

Figure 5.11: Vertical emittances for different pole face rotations. The injection turns are presented on the left hand side and the following turns on the right.

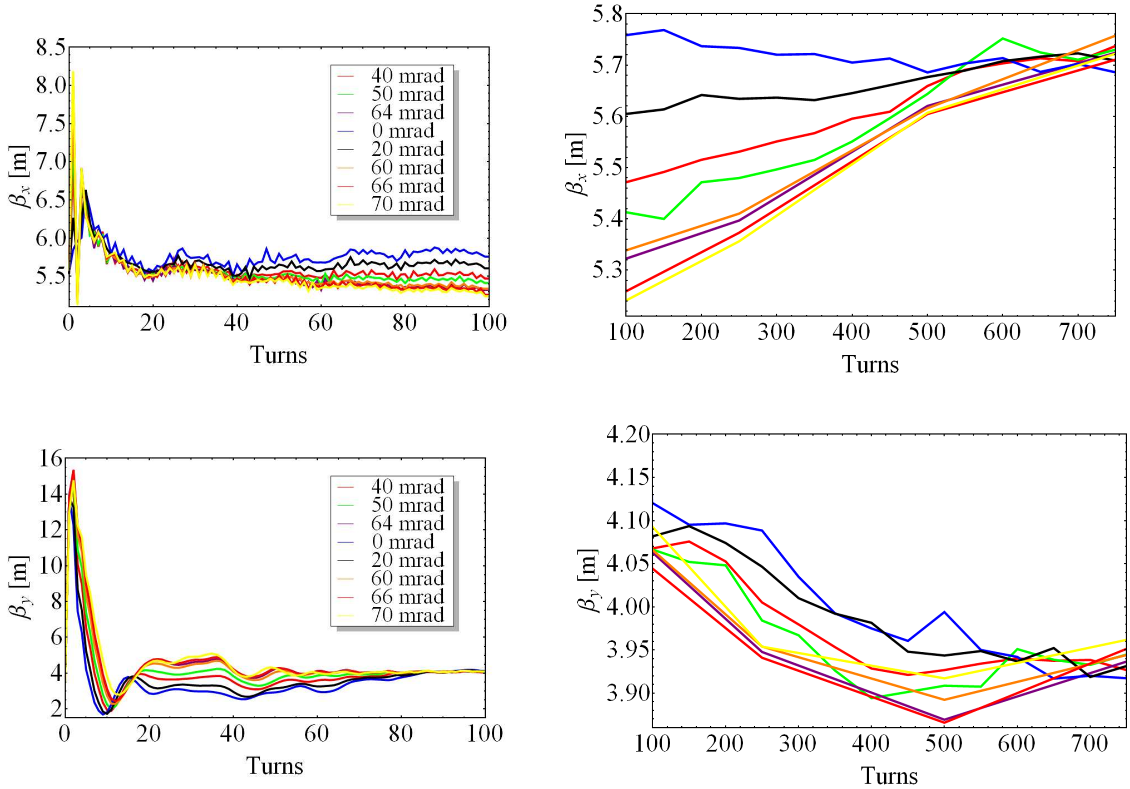

Figure 5.12: The four plots show the beta functions for the simulations with different pole face rotations. All horizontal functions are shown in the first, and the vertical functions in the second line.

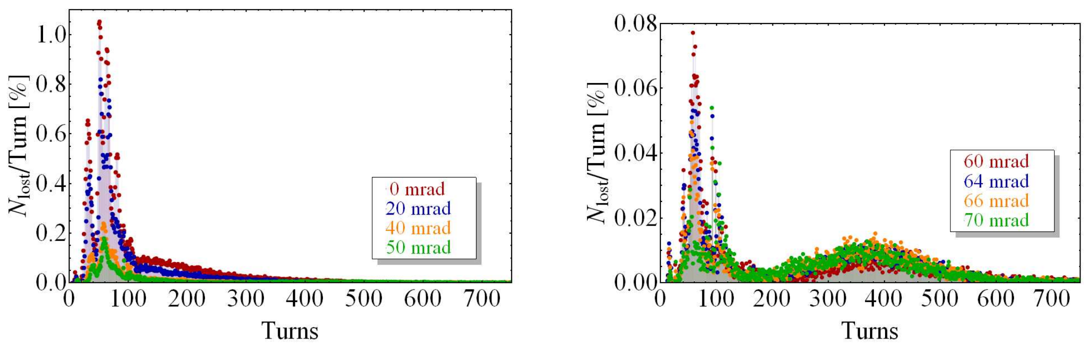

Figure 5.13: Relative losses per turn for different pole face rotations.

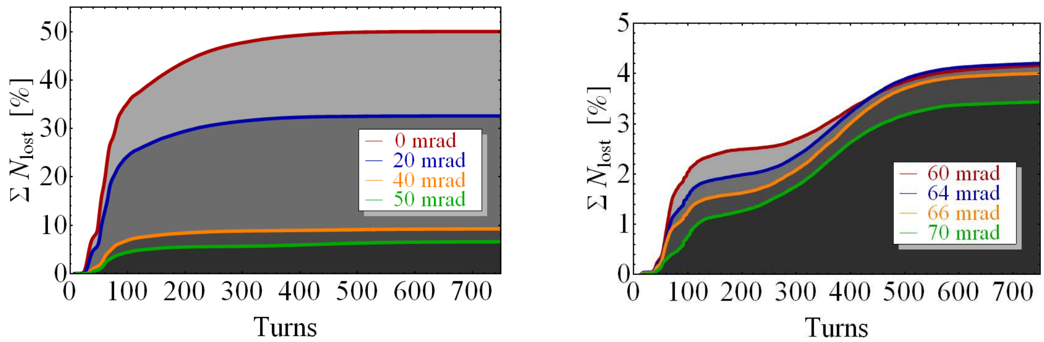

Figure 5.14: Accumulated losses for different pole face rotations.

5.3.8 Comparison of active and passive compensation

The impact of the active and the passive compensation scheme on Booster performance will be assessed in this section. For both schemes, many simulations were carried out to find the best setting within the scheme. These settings were used for two long simulations up to 20 000 turns and compared with each other.

For the active compensation scheme the values for the trim magnets were like calculated using MAD8 which means a perfect compensation. The passive compensation scheme was carried out with a 64 mrad pole face rotation at the BS magnets of the chicane. This setting provided the best results in the simulations run before.

Both simulations were carried out with 500 000 macro particles representing 1.6×10^{13} protons per bunch. To reduce the space charge density in the centre of the horizontal phase ellipse and to reduce the maximum betatron oscillation amplitudes, the particles were injected with an initial offset to the closed orbit of the machine in addition to the offset given by the painting bump. The desired horizontal emittances were obtained with these offsets and with the painting bump fall time adapted to it. All settings are listed in the Tab. C.6.

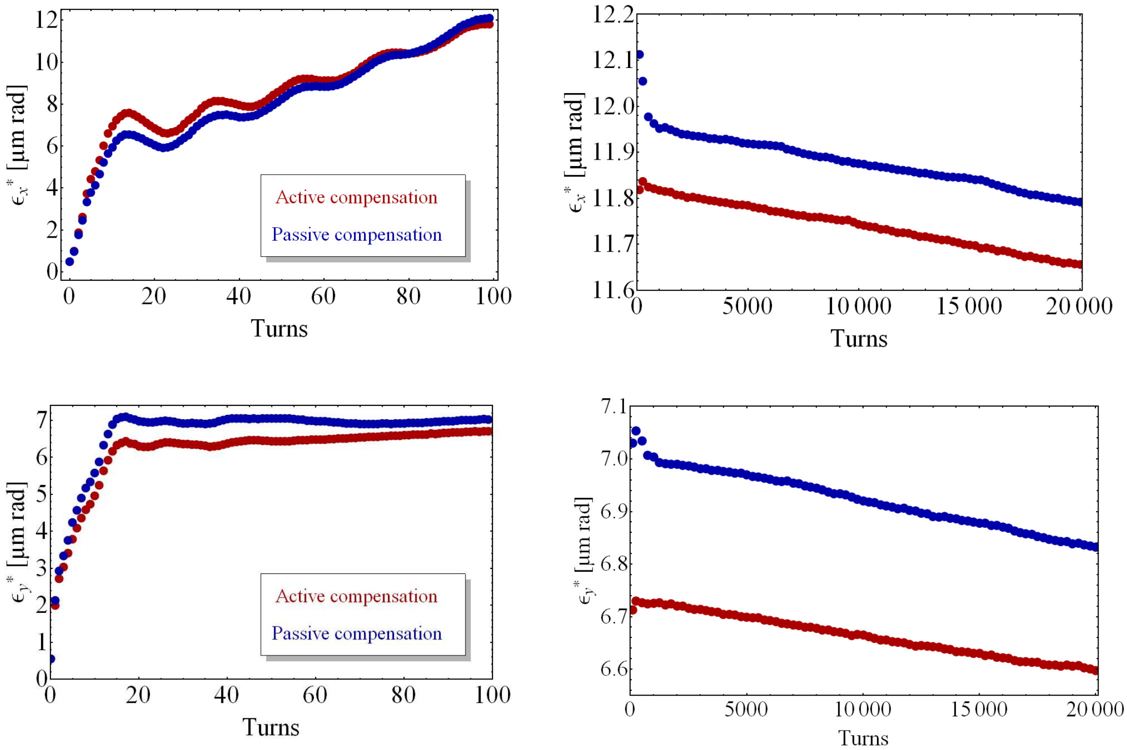

Figure 5.15: Normalised emittances for active and passive compensation scheme. The first line represents the emittances in the horizontal plane, the second line the emittances in the vertical plane. For each case, the injection turns are shown on the left and the turns after injection on the right hand side.

The small deviations for the emittances between the active and passive compensation scheme during injection is given by the different injection offsets as described above. The absolute value of the emittances after injection can be adjusted by the settings of the injection offset and the painting bump decrease time. That makes it non-relevant that there is a small deviation between the emittances for the active and passive compensation at the end of injection. More important is the emittance evolution during the simulation which is shown in the plots on the right hand side. The chicane decreases within 5000 turns for the active compensation and within 500 turns for the passive compensation scheme, starting to decay after injection. The chicane will be disappeared after 600 turns for the case of the passive compensation scheme and after 5100 turns for the active compensation. In the emittance plots in Fig. 5.15, it is visible that the emittances for the passive compensation decreases clearly in both planes during the first turns after injection. This is due to the losses caused by imperfect compensation of the lattice perturbations during the chicane fall After the chicane is vanished in both compensation schemes, the evolution of the emittances are almost the same.

The reasons for the shrinking normalised emittances after injection are the losses of particles at the simulated apertures as shown in Fig. 5.16.

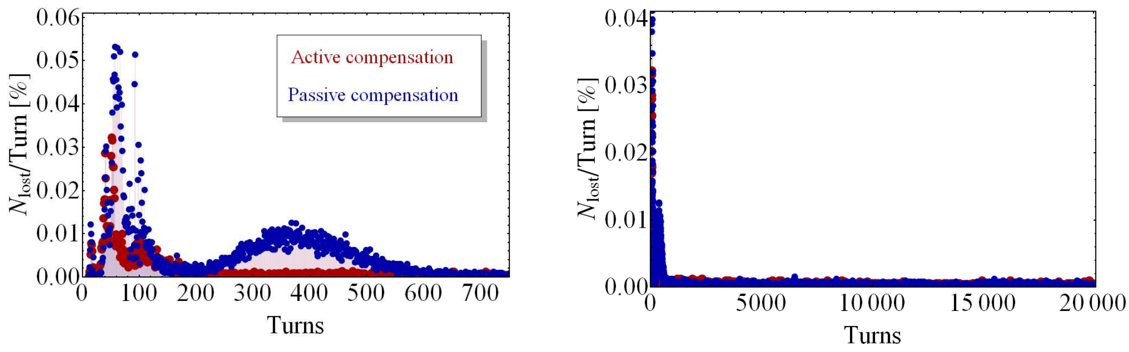

Figure 5.16: Relative losses per turn for the active and passive compensation scheme. The plot on the left shows the data for the injection and up to 250 turns and the plot on the right shows the data up to 20 000 turns.

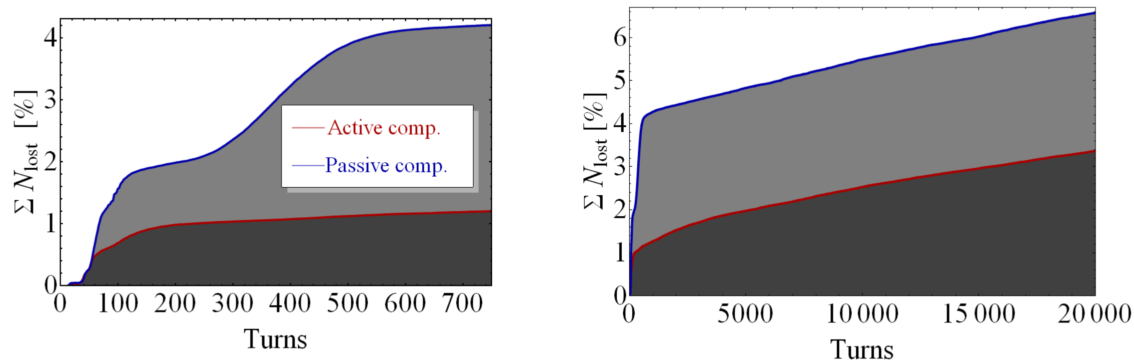

Figure 5.17: Accumulated losses for the active and passive compensation scheme. The plot on the left hand side shows the injection and the first turns up to 750 and the plot on the right hand side shows the data up to 20 000 turns

Figure 5.16 shows the loss rates per turn. As clearly visible, for both simulation schemes many particles are already lost during injection. This is due to the injection process with the chosen initial offset between injected beam and design orbit at the beginning of injection as well as to the linear painting bump decrease. Using the given setting, it is not possible to avoid all losses during injection if the desired normalised emittances of $\epsilon_x^* = 12$ μm rad and $\epsilon_y^* = 7$ μm rad should be archived for the high intensity beam. These losses could be possibly avoided using other values for the initial offset and for the painting bump fall time as well as using another function for the painting bump decrease.

For the active compensation scheme, the loss rates after injection are smaller compared to the ones with passive compensation. With active compensation, no significant increase of the loss rate is visible after 200 turns. This is not the case for the passive compensation scheme. Due to the implemented compensation of the edge focusing with fixed pole face rotations, the vertical half-integer resonance is strongly exited during a part of the chicane fall duration. For the passive compensation scheme, the chicane starts to decrease after 100 turns and decreases linearly within 500 turns. The maximum deflection of the beam during injection is 66 mrad and the pole face rotations at the BS magnets of the chicane, to mitigate the edge focusing, are 64 mrad in this case. The beam is therefore perpendicular at around 115 turns during chicane fall. Between 200 and 400 turns, the edge focusing effects are quite visible by strongly increased loss rates. The fact, that the losses per turn decrease after 400 turns again, although the angle between beam and pole faces increases, is due to the fact that the magnetic field becomes weaker. After the fall of the chicane in the passive compensation scheme (at 600 turns), both simulations show roughly the same loss rates per turn.

Fig. 5.17 shows the accumulated losses during the simulations for both compensation schemes. The information one can get from this plots are the same as from the plots in Fig. 5.16. The higher loss rates, using the passive compensation scheme translates into the larger slope. In the second plot for the accumulated losses, both simulations show the same slope from 600 turns on which means that in both simulations the same number of particles got lost per turn. Apart from the higher number of losses between 100 and 600 turns for the passive compensation scheme, there are no significant differences between the two compensation methods.

The tune footprints of the beams after 20 000 turns are shown in Fig. 5.18 for both, active and passive compensation. Since the ORBIT routine for the tune footprint calculations does not allow to run the calculations using several cores, this simulation had to be be carried out using just one core applying a special procedure.

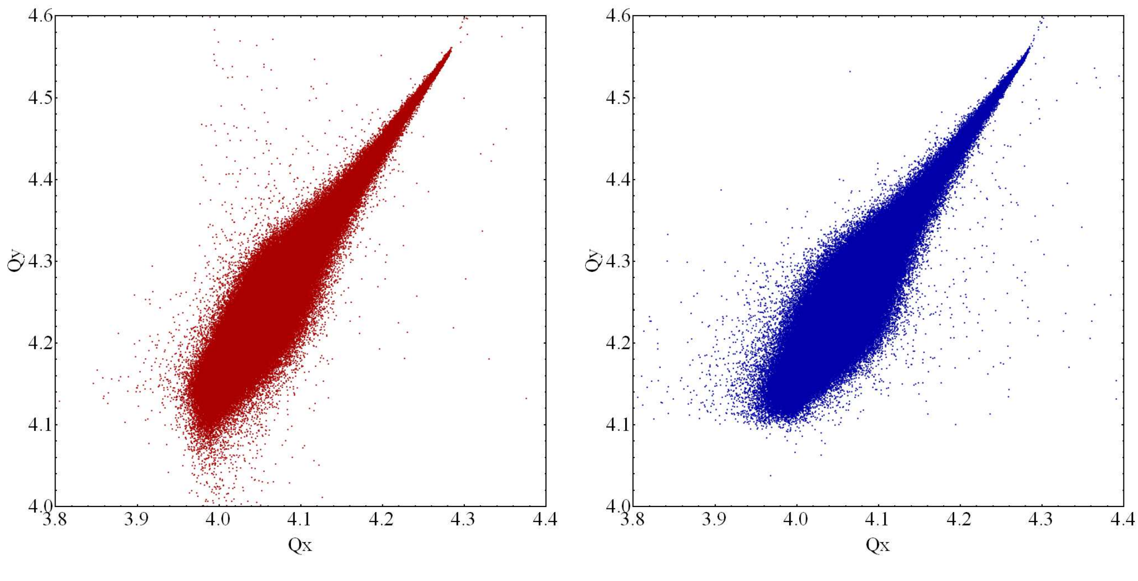

Figure 5.18: Tune footprints for active compensation scheme on the left hand side and for the passive scheme on the right hand side. Both footprints show almost the same size and shape.

From Fig. 5.18, one notes that there are no big differences between the tune foot prints for the two different compensation schemes. Due to the vertical injection tune at Q_y = 4.55, the tune footprint crosses the half integer resonance 2 Q_y = 9. For the active compensation scheme, there are more particles close to the vertical integer resonance Q_y = 4. The differences are assumedly due to the different particle distributions for the schemes and due to the different forces acting on the particles in the bunch.

The time dependence of the working point in order to move the tune below the half-integer resonance during acceleration was not implemented into the simulation, because the tune drift would be small during the simulation time.

After this comparison of the two different compensation schemes was made, it is clear that both schemes are feasible for the higher injection tune above the half-integer resonance at $2Q_y = 9$. The active compensation scheme features less particle losses than the passive compensation, but there is also no big beam blow up for the passive scheme.

5.3.9 Imperfect active compensation

In the previous chapter, passive compensation was compared with a perfect active compensation. However, in practice it may be difficult or even impossible to set up a perfect active compensation of lattice perturbations caused by the chicane. This motivates simulations with an imperfect active compensation scheme where the compensation was set to 90 % and 110 % of the theoretical value. The plots in Fig. 5.19 - Fig. 5.22 present the emittance evolution, the beta functions and the particle losses for the two imperfect compensations as well as for the perfect compensation to compare with.

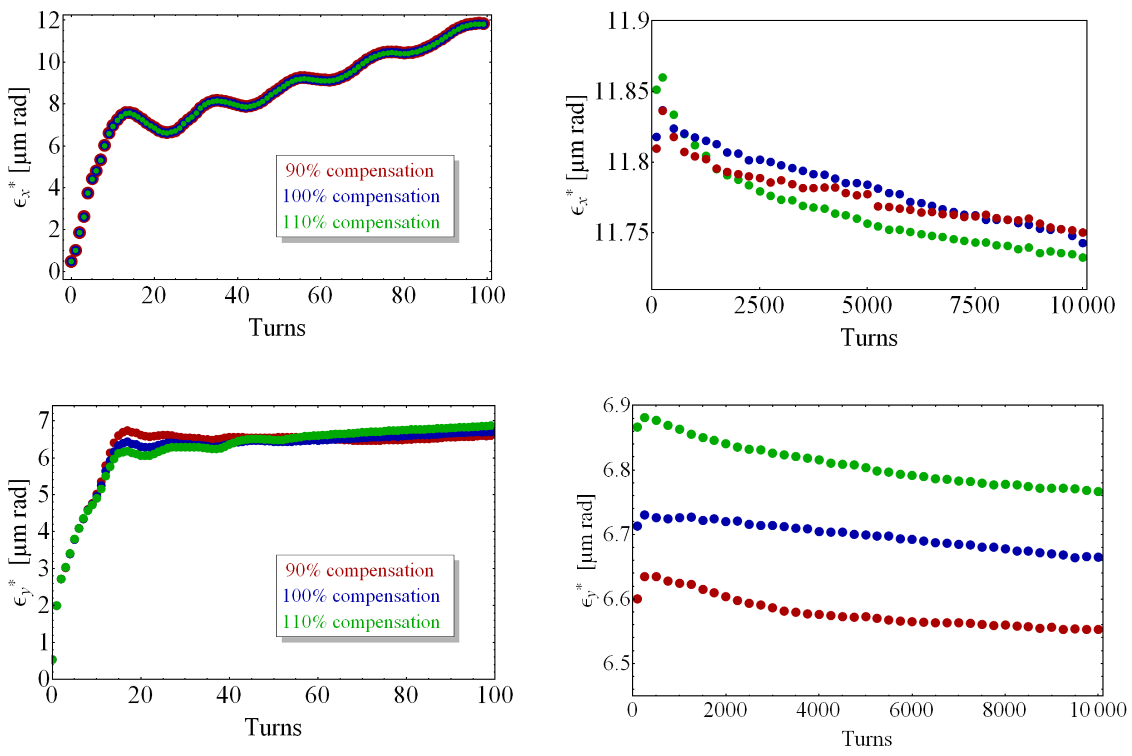

Figure 5.19: Normalised emittances for imperfect active compensation schemes. The first line represents the emittances in horizontal plane, the second line the emittances in vertical plane. For each case the injection turns are shown on the left and the turns after injection on the right hand side.

During injection, there are almost no differences of the emittance evolutions between the perfect and the imperfect compensations in the horizontal plane, but there are small deviations in the vertical plane which are explained by different beta functions for the two imperfect compensations. The beta functions for the imperfect active compensations are shown in Fig. 5.20.

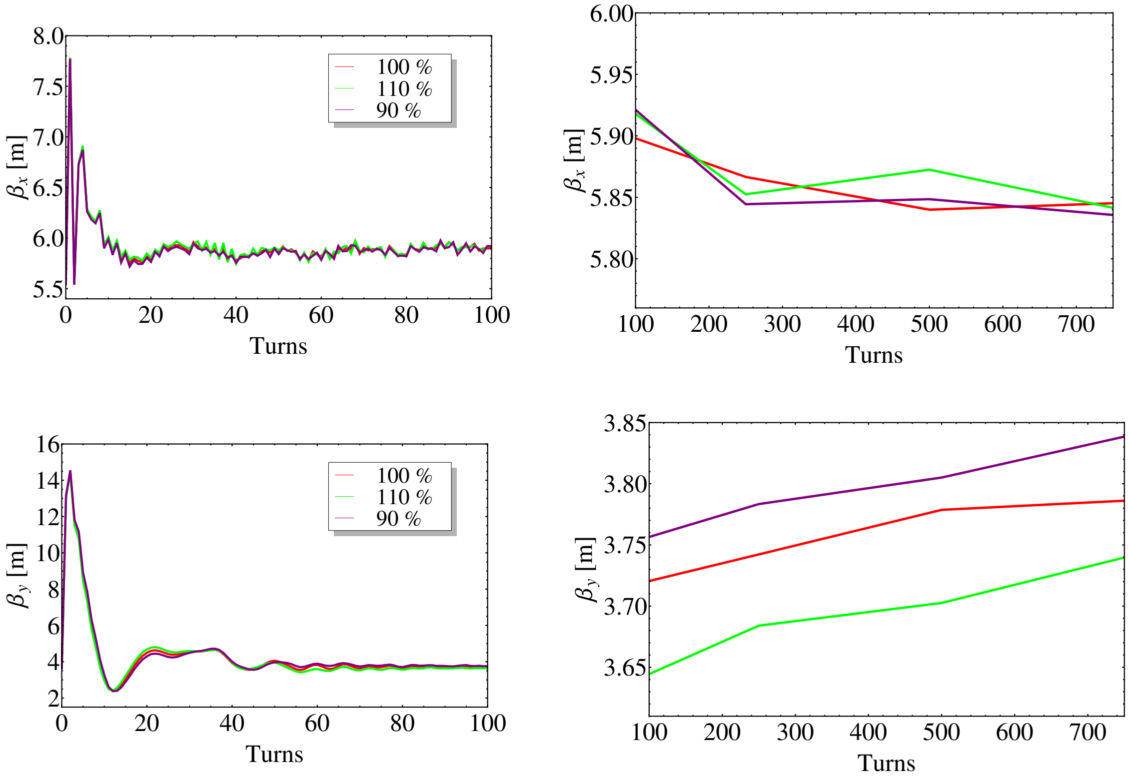

Figure 5.20: Beta functions for the imperfect active compensation. The injection turns are shown on the left hand side and the following turns on the right. In the first line, the horizontal functions are presented and in the second line the vertical ones.

The emittance evolutions for the turns after injection which are shown on the right hand side in Fig. 5.19, are slightly different for the different settings. One observes different slopes for the three simulations, especially until the end of the chicane fall at 5000 turns. The slope of the emittances is, in both planes, slightly higher for the imperfect compensations indicating higher loss rates per turn.

The plots in Fig. 5.21 present the relative number of lost particles per turn for the imperfect active compensation and for a reference simulation with perfect active compensation. Fig. 5.22 shows the plots for the accumulated losses.

There are again losses during injection, but, as discussed before, these losses cannot be avoided using the present linear painting bump, if the desired emittances should be achieved. The largest loss rates are obtained with the 90% compensation. The losses for 110% compensation are almost the same as for the perfect case during injection and slightly higher after the first 100 turns.

The number of accumulated losses during the simulation is as expected. The smallest number of lost particles is achieved with the perfect compensation and the losses for the 90% compensation are higher than those for the two others. As shown in the plot up to 10 000 turns in Fig. 5.22, after the chicane fall one can

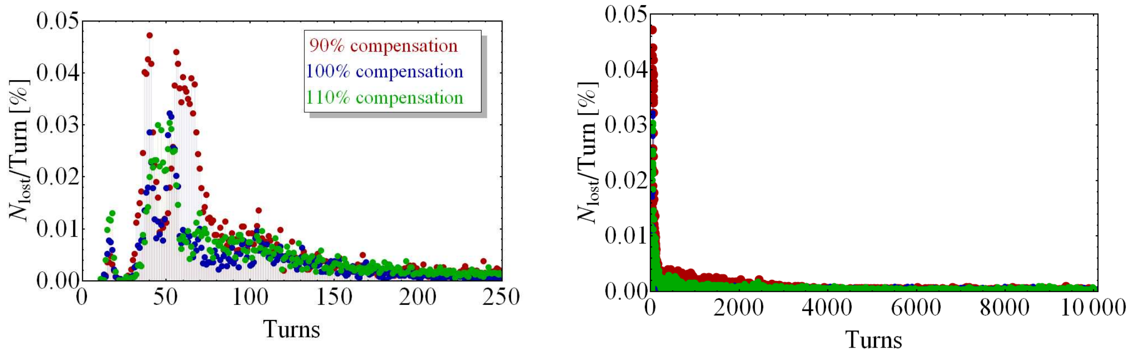

Figure 5.21: Relative losses per turn for imperfect active compensation scheme. The plot on the left shows the data for the injection and up to 250 turns and the plot on the right shows the data up to 10 000 turns.

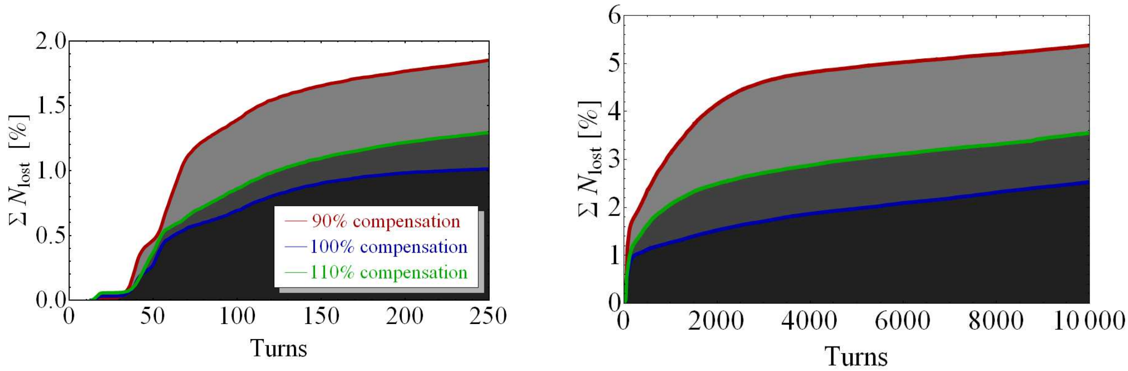

Figure 5.22: Accumulated losses for imperfect active compensation schemes. The plot on the left hand side shows the injection and the first turns up to 250 and the plot on the right hand side shows the data up to 10 000 turns

find the same slope for all three cases. As there is no perturbation left after the chicane is decreased, the compensation is not in use any more and this leads to the same results for all three simulations.

One concludes that simulations with both imperfect compensations with $\pm$ 10% yield acceptable loss rates for Booster operation. In both imperfect compensation cases, losses observed are smaller than for passive compensation.

Comparing these results with the measurements at the Booster (cf. section 4.2), one can observe that the active compensation of the half-integer resonance as implemented to the Booster shows a comparable evolution of the emittances and the loss rates for a $\pm$10% variation of the compensation. This approves the results of the simulations.

Chapter 6

Conclusions and prospects

The most important conclusion of the simulations presented in this thesis is that the injection of a high intensity beam from Linac4 to the PS Booster and the acceleration of the particles is feasible with both compensation schemes for the higher vertical tune above the half integer resonance at $2Q_y = 9$.

Furthermore, the single simulations and the comparison of the data led to the following conclusions:

- The first test were concerning to basic implementations to the ORBIT code like the acceleration function. Testing the impact of this tool, one could see that the acceleration is well implemented to the code.
- The apertures are implemented with dimensions corresponding to the PS Booster as existing at the moment and the size of the beam scope window is adapted to the higher injection energy with Linac4. An additional aperture was implemented to the injection area to simulate the injection septum at the second chicane magnet. A test simulation showed that the apertures are implemented properly.
- The benchmarking on the number of macro particles showed that 500 000 macro particles are enough to avoid statistical effects and the size of the dumped files are still in a rage one can handle.
- The comparison of the different foil scattering models implemented to ORBIT led to the decision to use scattering "model 1" which represents the expected scattering distribution much better than "model 2". It was decided that the disregard of the energy loss for scattered particles in "model 1" can be neglected due to the fact that the expected effects are small.
- To simulate the dynamic chicane in the injection area running ORBIT simulations, the lattice elements have to be erased and reinstalled each turn during the chicane fall. The simulation to investigate impacts caused by the continuously re-installation of the foil showed unexpected deviations between the simulations with a lattice which was installed just once and a lattice which was reinstalled during each turn. The reasons for the deviations were not completely understood and it may be interesting to continue with further investigation on this topic.
- The quadrupole resonances documented for one simulation applying the passive compensation scheme show the frequencies which were expected due to the fact that those frequencies are related to the tune spread.
- Simulating the passive compensation scheme for the perturbations at the chicane magnets, one investigated that it is feasible to run the machine applying this compensation method. A benchmarking on the pole face rotations aiming to find the angle which leads to the smallest particle losses led to the

surprisingly large angle of 64 mrad. Further studies could confirm this value and one could run additional simulations to explore the best pole face rotation angle for other beams like the LHC nominal beam.

- Running simulations for both compensation schemes and comparing the results, one could find out that the active compensation scheme leads to less losses than the passive one. Both compensation schemes show losses during the injection which are related to the fact that some particles are already injected outside the machine acceptance. This was not avoidable using a linear painting bump if the required emittances for a high intensity beam should be achieved. One possibility to reduce the number of lost particles during injection is eventually to modify the function of the painting bump. Further losses occurred in case of the passive compensation during the chicane fall caused by the fact that the compensation of the edge focusing effects cannot be realised with a fixed passive compensation during the whole fall of the chicane. The losses during the chicane fall plus the losses during injection lead to higher loss rates for the passive compensation compared with the active counterpart, but still the losses for both schemes are in an acceptable range.

- The simulation treating a perfect active compensation demonstrated the feasibility of the scheme, but it was also of note to see the results for an imperfect active compensation. Two simulations with $\pm$ 10 % variation of the compensation magnet strength showed that the loss rates are higher than for the perfect case, but still acceptable. The simulation for the 110 % focusing strength in the trims led to roughly 30 % more losses and the 90 % focusing strength doubled the number of lost particles compared to the perfect compensation.

Due to different fall times of the chicane for the two compensation schemes, there are also different requirements on the lattice elements. Both schemes have different demands on the power supplies, the active compensation scheme for the additional trim magnets which have to follow a pre-programmed time evolution in order to compensate the varying edge focusing effects during the chicane fall, and the passive compensation needs fast and powerful power supplies to realise the chicane fall within 0.5 ms. The fast chicane applied for the passive compensation scheme requires also special vacuum chambers, otherwise, the fast ramped magnets will induce currents which will then lead to further perturbations. This problems can be solved with ceramic vacuum chambers. Eventually, the ceramic vacuum chambers or corrugated vacuum chambers have to be used also with the active compensation. One should also consider, that the passive compensation scheme will be fixed whereas the active compensation will be flexible which could be once an advantage if something will be changed in the Booster lattice or in the operating schedule.

A further tasks concerning the simulations of the H^- charge exchange injection from Linac4 to the Booster could be the implementation of imperfections caused by additional multipolar components and misalignment of lattice elements in order to investigate the impact of these perturbations on the Booster performance.

Furthermore, it could be interesting to get a modified ORBIT code which gives the possibility to change the strength of quadrupole and dipole magnets in order to realise the dynamic lattice without erasing and reinstalling the lattice at each turn. Another useful implementation would be a function to calculate the emittances and other beam parameters in ORBIT without dumping the particle coordinates which requires a lot of memory space and time for the calculation.

Appendix A

Deviations due to the re-installation of the lattice

During the chicane fall, the lattice has to be erased and re-implemented at each turn with modified values for the magnets related to the chicane and, in case of the active compensation, for the magnets related to the trim quadrupols. No artefacts were expected with this procedure [21]. Nevertheless, to investigate if there are unusual impacts from the fact that the lattice, and especially the foil, is reinstalled at each turn, two simulations were carried out and compared. The two runs started for this comparison were exactly the same but in the first one, the lattice was installed just once at the beginning and in the second run, the installation took place at each turn.

The used lattice was fixed which means without decaying bumps. Thus, there are no disturbing factors by chicane modifications and the beam passed through the foil during the whole simulation and not just for the injection turns. This will enlarge the effect of the foil on the beam and, if there are differences between the two ways to install the lattice, they will be more developed. The desired emittances were archived by an offset in both planes between the injected beam and the design orbit. To speed up the simulations, they were run with 100 000 macro particles instead of half a million like usual. This should be no problem, because the reason to run this simulations is just to find differences between the two simulations if existing. If there is any impact caused by the smaller number of macro particles, it will occur in both simulations. All simulation settings are summarised in Tab. C.3. The plots in Fig. A.1 show the emittance evolution during the simulation.

The emittance evolution is the same for both simulations during injection. After the injection and due to scattering at the injection foil, there is an emittances growth up to approximately 300 turns in both planes and for both simulations. After the beam reaches a certain size, more and more particles get lost at the apertures and the emittance starts to shrink again. Small deviations between the two injection schemes take place for higher turn numbers which was not expected. The reasons for the different result are not clear yet and have to be investigated later.

One notes that the accumulated losses for the two simulations, presented in Fig. A.2, are almost identical. From this observation and the almost similar emittance evolutions during the injection, one concludes that the procedure with regular re-installation of the lattice has negligible impact on the results of the simulation.

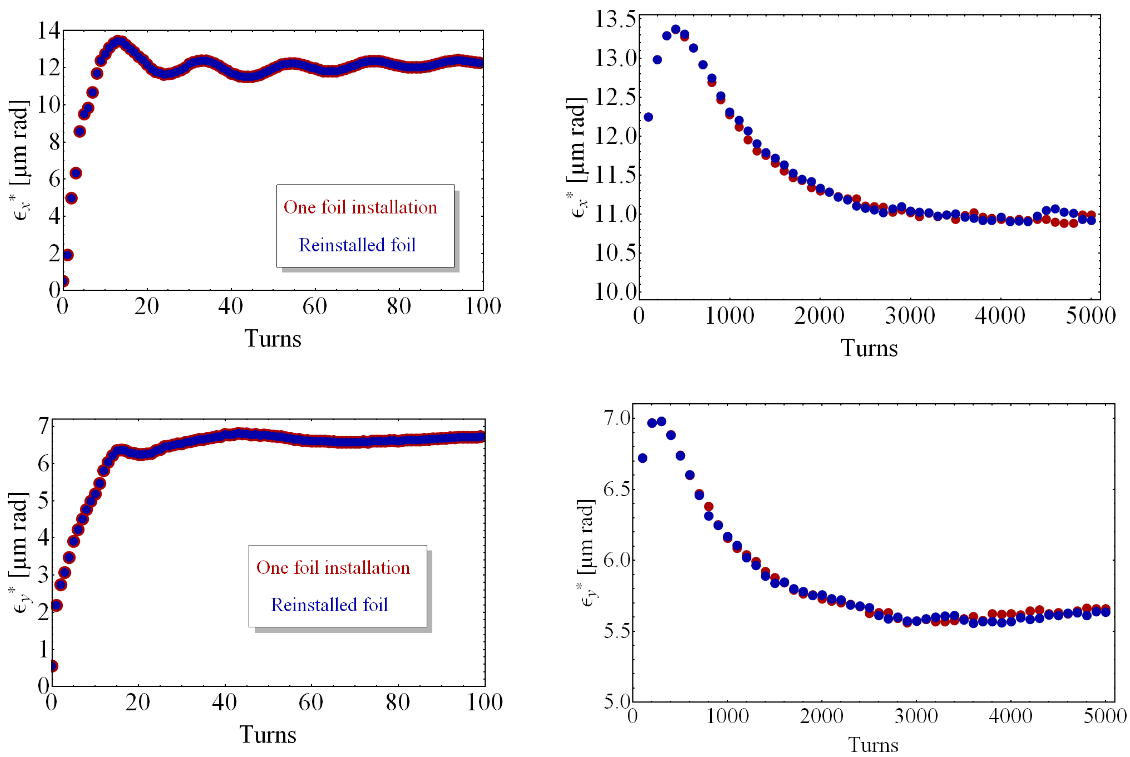

Figure A.1: Normalised emittances for the different installation schemes for the lattice. The first line shows the horizontal and the second line the vertical plane. The injection turns are presented on the left hand side and the turns up 5000 turns on the right hand side.

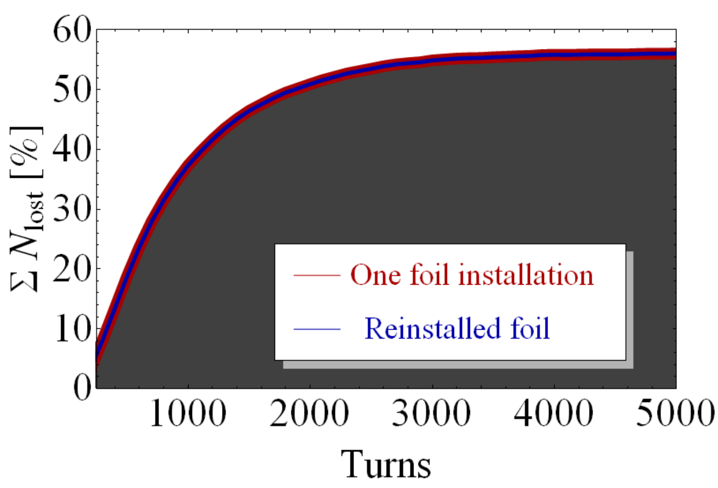

Figure A.2: Accumulated losses for different installation schemes for the lattice.

Appendix B

Measurements at the PS Booster

All data of the emittance measurements at the PS Booster (cf. chapter 4), are listed in the following Tab. B.1.

Table B.1: Measured emittances for different compensation adjustments.

$I_{Parameter1}$ [A]	$I_{Parameter2}$ [A]	$\epsilon_y^{2\sigma}$ [μm rad]	ϵ_y^* [μm rad]	Comments
-3.04	-5.69	14.4	8.22	
-3.04	-4.5	14.36	8.20	
-3.04	-4.2	14.64	8.36	
-3.04	-3.9	14.45	8.25	
-3.04	-3.3	13.89	7.93	
-3.04	-2.7	14.38	8.21	
-3.04	-2.1	13.99	7.99	
-3.04	-1.75	13.72	7.83	
-3.04	-1.1	13.85	7.91	
-3.04	-0.8	0	0.00	$\rightarrowtail$ Beam got lost
-3.04	-5.7	14.35	8.19	
-3.04	-6.3	14.46	8.26	
-3.04	-7.5	14.29	8.16	
-3.04	-8.3	14.16	8.09	
-3.04	-8.9	14.07	8.03	
-3.04	-9.2	13.69	7.82	
-3.04	-9.5		0.00	$\rightarrowtail$ Beam got lost
-3.04	-9.8		0.00	
-4.03	-6	14.36	8.20	
-4.03	-7.15	14.2	8.11	
-4.03	-8	14.05	8.02	
-4.03	-8.9	0	0.00	$\rightarrowtail$ Beam got lost
-5.03	-5.7	14.24	8.13	
-5.03	-7.2	13.91	7.94	
-5.03	-7.7	0	0.00	$\rightarrowtail$ Beam got lost
-6.02	-6	0	0.00	$\rightarrowtail$ Beam got lost
-2.05	-7.2	14.41	8.23	
-2.05	-8.6	14.3	8.17	
-2.05	-9.5	0	0.00	$\rightarrowtail$ Beam got lost

Appendix C

Simulation settings

In the following tables, one can find all settings used for the simulations presented in chapter 5.

Table C.1: Implementation of the acceleration

General settings	
Simulation date: 24.02.2010	Active compensation scheme
Simulation up to 2500 turns	Injection position: -35 mm / 8.45 mm
No of macro particles: 500 000	No of protons per bunch: 1.6×10^{13}
Q_y = 4.55	Q_x = 4.28
Space charge: not implemented	Apertures: not implemented
Injection foil: not implemented	Acceleration: implemented
Painting bump	
Maximum height: 25 mm	Fall time: 280 μs
About the active compensation	
KQDE and KQFO: 100%	dKQDE: 100%
Emittances after injection	
ϵ_x = 20.65 μm rad	ϵ_y = 10.92 μm rad

Table C.2: Benchmarking about the number of macro particles

General settings	
Simulation date: 14.12.2009	Active compensation scheme
Simulation up to 10 000 turns	Injection position: -35 mm / 8.45 mm
No of macro particles: 250 000, 500 000, 750 000	No of protons per bunch: 1.6×10^{13}
Q_y = 4.55	Q_x = 4.28
Space charge: implemented	Apertures: implemented
Injection foil: implemented	Acceleration: implemented
Painting bump	
Maximum height: 25 mm	Fall time: 280 μs
About the active compensation	
KQDE and KQFO: 100%	dKQDE: 100%
Emittances after injection	
$\epsilon_{x,2.5E5mp}$ = 19.41 μm rad	$\epsilon_{y,2.5E5mp}$ = 11.01 μm rad
$\epsilon_{x,5E5mp}$ = 19.41 μm rad	$\epsilon_{y,5E5mp}$ = 11.03 μm rad
$\epsilon_{x,7.5E5mp}$ = 19.41 μm rad	$\epsilon_{y,7.5E5mp}$ = 11.06 μm rad

Table C.3: Simulations to investigate deviations caused by the re-installation of the stripping foil.

General settings

Simulation date: 10.05.2010	Active compensation scheme
Simulation up to 10 000 turns	Injection position: -14.95 mm / 8.45 mm
No of macro particles: 100 000	No of protons per bunch: 1.6×10^{13}
Q_y = 4.55	Q_x = 4.28
Space charge: implemented	Apertures: implemented
Injection foil: implemented	Acceleration: implemented

Painting bump

A fixed lattice without painting bump was used

About the active compensation

KQDE and KQFO: 100%	dKQDE: 100%

Emittances after injection

$\epsilon_{x,one\ implementation}$ = 20.12 μm rad	$\epsilon_{y,one\ implementation}$ = 11.04 μm rad
$\epsilon_{x,reimplementation}$ = 20.12 μm rad	$\epsilon_{y,reimplementation}$ = 11.04 μm rad

Table C.4: Investigation of quadrupole resonances after injection and after chicane fall.

General settings

Simulation date: 19.02.2010	Passive compensation scheme
Simulation up to 220 respectively to 720 turns	Injection position: -14.95 mm / 8.45 mm
No of macro particles: 100 000	No of protons per bunch: 1.6×10^{13}
Q_y = 4.55	Q_x = 4.28
Space charge: implemented	Apertures: implemented
Injection foil: implemented	Acceleration: implemented

Painting bump

A fixed lattice without painting bump was used

About the passive compensation

Pole face rotation: 64 mrad

Emittances after injection

ϵ_x = 19.90 μm rad	ϵ_y = 11.55 μm rad

Table C.5: Imperfect passive compensation.

General settings	
Simulation date: 12.03.2010	Passive compensation scheme
Simulation up to 10 000 turns	Injection position: -35 mm / 9.06 mm
No of macro particles: 500 000	No of protons per bunch: 1.6×10^{13}
Q_y = 4.55	Q_x = 4.28
Space charge: implemented	Apertures: implemented
Injection foil: implemented	Acceleration: implemented
Painting bump	
Maximum height active comp: 29 mm	Fall time active comp: 195 μs
About the passive compensation	
Pole face rotations of: 0, 20, 40, 50, 60, 64, 66, and 70 mrad	
Emittances after injection	
cf. Tab. 5.6	

Table C.6: Comparison of active and passive compensation scheme.

General settings	
Simulation date: 03.01.2010	Active and Passive compensation scheme
Simulation up to 20 000 turns	Injection position: -35 mm / 8.45 mm for active, -35 mm / 9.06 mm for passive comp.
No of macro particles: 500 000	No of protons per bunch: 1.6×10^{13}
Q_y = 4.55	Q_x = 4.28
Space charge: implemented	Apertures: implemented
Injection foil: implemented	Acceleration: implemented
Painting bump	
Maximum height active comp: 25 mm	Fall time active comp: 290 μs
Maximum height active comp: 29 mm	Fall time active comp: 255 μs
About the compensation schemes	
passive compensation:	Pole face rotation: 64 mrad
active compensation:	all gradients set to 100%
Emittances after injection	
$\epsilon_{x,\ active\ comp}$ = 19.41 μm rad	$\epsilon_{y,\ active\ comp}$ = 11.03 μm rad
$\epsilon_{x,\ passive\ comp}$ = 19.90 μm rad	$\epsilon_{y,\ passive\ comp}$ = 11.45 μm rad

Table C.7: Imperfect active compensation.

General settings	
Simulation date: 12.03.2010	Active compensation scheme
Simulation up to 10 000 turns	Injection position: -35 mm / 8.45 mm
No of macro particles: 500 000	No of protons per bunch: 1.6×10^{13}
Q_y = 4.55	Q_x = 4.28
Space charge: implemented	Apertures: implemented
Injection foil: implemented	Acceleration: implemented
Painting bump	
Maximum height active comp: 25 mm	Fall time active comp: 290 μs
About the active compensation	
KQDE and KQFO: 100%	dKQDE: 90%, 100% and 110%
Emittances after injection	
$\epsilon_{x,\ 90\%}$ = 19.47 μm rad	$\epsilon_{y,\ 90\%}$ = 10.84 μm rad
$\epsilon_{x,\ 100\%}$ = 19.41 μm rad	$\epsilon_{y,\ 100\%}$ = 11.03 μm rad
$\epsilon_{x,\ 110\%}$ = 19.40 μm rad	$\epsilon_{y,\ 110\%}$ = 11.28 μm rad

List of Figures

Bibliography

[1] Web site: http://en.wikipedia.org/wiki/CERN, May 2010.

[2] ORBIT user manual version 1.10, J.D. Galambos, J.A. Holmes, D.K. Olsen, SNS Building MS-8218, Oak Ridge National Laboratory, A. Luccio, J. Beebee-Wang, Brookhaven National Laboratory, Upton, NY, Juli 16, 1999.

[3] Web site: http://www.electronicsweekly.com/blogs/electronics-weekly-blog/CERN-Accelerators.gif, April 2010.

[4] Physik der Teilchenbeschleuniger und Ionenoptik, 2. Auflage von Frank Hinterberger, Springer Verlag.

[5] Particle Accelerator Physics, Third Edition, Helmut Wiedemann, Springer Verlag.

[6] Basic course on Accelerator physics, J. Rossbach, P. Schmüser.

[7] Active longitudinal painting for the H^- charge exchange injection of the Linac4 beam into the PS Booster, AB-Note-2008-011 ABP, C. Carli, R. Garoby.

[8] Particle Physics Booklet, July 2008, Elsevier, Available from LBNL and CERN.

[9] Stripping foils for the PSB H^- injection system, CERN sLHC Project Node 005, M.Aiba, C.Carli, B.Goddard, W.Weterings.

[10] Web site: http://en.wikipedia.org/wiki/Perveance, April 2010.

[11] PS Booster Web site: http://psb-machine.web.cern.ch/psb-machine/default.asp, March 2010.

[12] Linac2 Web site: http://linac2.home.cern.ch/linac2/default.htm, April 2010.

[13] Superconducting Proton Linac development at CERN, K. Hanke, R. Garoby, F. Gerigk, A.M. Lombardi, C. Rossi, M. Vretenar (CERN, Geneva, Switzerland) S. Chel, R. Duperrier, D. Uriot (CEA Saclay Gif-sur-Yvette, France), P. Pierini (INFN Milano, Italy).

[14] Technical design report for Linac4, 2006.

[15] SNS Web site: http://neutrons.ornl.gov/aboutsns/aboutsns.shtml, Feb. 2010.

[16] L. Schachinger and R. Talman, TEAPOT: A thin element accelerator program for optics and tracking, Particle Accelerators 22, 35 (1987).

[17] Pythen Programming Language, official website: http://www.python.org/, April 2010

[18] Masamitsu Aiba, privat communication.

[19] Web site: http://www.wolfram.com/products/mathematica/index.html, May 2010.

[20] Measures avec pick-up quadripolare a Lear, PS/AR/Note 95-15, M. Chanel.

[21] SNS, privat communication.

Erklärung:

Hiermit bestätige ich, dass die vorliegende Arbeit von mir selbstständig verfasst wurde und ich keine anderen als die angegebenen Hilfsmittel – insbesondere keine im Quellenverzeichnis nicht benannte Internet-Quellen – benutzt habe und die Arbeit von mir vorher nicht einem anderen Prüfungsverfahren eingereicht wurde. Ich bin damit einverstanden, dass die Diplomarbeit veröffentlicht wird.

Genf, 13.Mai 2010

Matthias Scholz

Acknowledgments

Zunächst möchte ich mich herzlich bei Christian Carli, meinem Betreuer am CERN, für die große Mühe, die Er sich gegeben hat, und für die guten Tipps sowie Hilfen, die ich während meiner Arbeit erhalten habe, bedanken. Ohne die gute Betreuung währe es mir nicht möglich gewesen, diese Arbeit so zu schreiben, wie sie jetzt vorliegt. Während unzähliger Kaffee- und Teegespräche hat Er mir alle Fragen beantwortet und es spielte dabei keine Rolle, ob ich diese zum ersten oder zum wiederholten Mal gestellt habe.

Herzlichen Dank auch an Eckhard Elsen, meinen Betreuer der Uni Hamburg, der mir stets mit guten Ratschlägen beigestanden hat und sich bei jedem Besuch am CERN viel Zeit nahm, meine Arbeit zu besprechen und mir wertvolle Tipps gab. Auch die vielen Emails, die in dieser Zeit geschrieben wurden, beantworteten viele meiner Fragen.

Beiden Betreuern möchte ich außerdem noch dafür danken, dass Sie es mir ermöglicht haben zu den Beschleunigerphysik-Schulen der CAS und TAS sowie zur Tagung der DPG zu fahren. Alle drei Veranstaltungen haben mir viel Freude bereitet und ich konnte Erfahrungen sammeln, die ich nicht mehr missen möchte.

Un grande grazie alle mie dolcissime compagne di ufficio Barbara e Simona. E‘ stato un piacere condividere l’ufficio e le pause pranzo con voi. Sono stato accolto benissimo fin dal primo giorno e sono molto contento di aver trovato due amiche cosi‘. Grazie a voi, ho vissuto il tempo trascorso in ufficio quasi come se fossi stato in vacanza in Italia invece che al lavoro. Inoltre, vorrei ringraziare Marco per essere stato sempre cosi‘ gentile e rilassato tutte le volte che veniva in ufficio. Ho apprezzato molto la tua capacita‘ di fare sentire a proprio agio le persone attorno a te! Thank you Elena for the translation!

A big THANK YOU goes to the "lunch group" I was allowed to join every day in restaurant 1. I still can’t believe that it was possible to find so many good friends in such a short time. Well, very often I was the only non Italian during lunch, but you were so nice that each lunch was like one day of holiday in Italy. Thank you all for the nice time we spend together.

Einen „urgroßen” Dank auch an die Östereicher bei der Arbeit und deren Freundinnen. Ihr habt mich als „Piefke” jederzeit herzlich aufgenommen und immer dafür gesorgt, dass ich mich wohlgefühlt habe. Vielen Dank für die schöne Zeit und Eure herzliche Gastfreundschaft, es war immer „urgut”.

A big thanks goes to my colleagues Michel Chanel, Michel Martini, Masamitsu Aiba and Frank Stulle for all the helpful discussions about my work. I felt always welcome in your offices and you helped me with all the questions I asked.

The first time in a new country and in a new office is always exciting, but thanks to Anneline who helped me to find my apartment and who was a good neighbour and friend during the time we stayed at the same place, I felt myself comfortable from the first moment on.

Ohne Jörg Rossbach und seine interessante Vorlesung zur Beschleunigerphysik wäre ich nie zu diesem wunderbaren Thema gekommen. Auch die Übungsgruppe von Bernhard Schmidt und seine kniffligen Aufgaben haben unbedingt dazu geführt, dass ich von diesem Thema nicht mehr lassen kann, wofür ich mich ausdrücklich bedanken möchte.

Die Verbindung zum CERN und zur Gruppe ABP kam über meinen Mentor Peter Schleper zustande, der mir auch schon zuvor während des Studiums stets mit gutem Rat zur Seite stand. Vielen Dank für die Betreuung und für den entscheidenden Anruf bei Eckhard Elsen.

Einen herzlichen Dank möchte ich noch Alexander Gewering Peine aussprechen, der mich in vielen Emails und Telefonaten unterstützt sowie über alles Neue in Hamburg auf dem Laufenden gehalten hat. Ich freue mich schon darauf in Kürze mit Dir zusammen am DESY anzufangen!

Liebe Ursula, lieber Bernhard, ohne Euch währe es absolut überhaupt nicht gegangen... Danke, für Eure liebe Unterstützung in den letzten drei Jahrzehnten. Ich bin froh Euch als meine Eltern zu haben. Außerdem besten Dank an meine lieben Schwestern Merit, Astrid und Manuela, die immer fest an Ihren großen Bruder geglaubt haben.

Ich möchte außerdem Jutta und Heiz Jürgen Schmidt für Ihre herzliche Art und für all die Unterstützung während der letzten Jahre danken. Es währe mir vieles schwerer gefallen ohne Eure Hilfe.

Liebe Sonja, ohne Dich währe trotzt guter Betreuung und guter Freunde alles nicht machbar gewesen! Ich Danke Dir von ganzem Herzen für all Deine Unterstützung und den Rückhalt, den Du mir immer gegeben hast. Deine Offenheit und Deine Selbstverständlichkeit, mit der Du mir begegnest, sind wunderbar und haben mir in unserer gemeinsamen Zeit viele neue Einblicke und Erfahrungen ermöglicht. All das möchte ich nicht mehr missen. Ich freue mich ganz besonders, bald wieder bei Dir in Buxtehuder zu sein!